Summer 8-15-2017

Novel PET Systems and Image Reconstruction with Actively Controlled Geometry

Ke Li
Washington University in St. Louis

Washington University in St. Louis

School of Engineering and Applied Science

Department of Electrical and Systems Engineering

Dissertation Examination Committee:
Joseph A. O'Sullivan, Chair
Mark A. Anastasio
R. Martin Arthur
Joseph P. Culver
Yuan-Chuan Tai

Novel PET Systems and Image Reconstruction with Actively Controlled Geometry

by

Ke Li

A dissertation presented to
The Graduate School
of Washington University in
partial fulfillment of the
requirements for the degree
of Doctor of Philosophy

Aug 2017
Saint Louis, Missouri

Contents

List of Tables . . . . . **v**

List of Figures . . . . . **vi**

Acknowledgments . . . . . **x**

Abstract . . . . . **xiii**

1 Introduction **1**
1.1 Fundamental Physics of Positron Emission Tomography 1
1.2 Detection and Data Acquisition 2
1.3 Monte Carlo Simulation 3
1.4 Image reconstruction for PET 4
1.5 Evolution of PET Design 5
1.6 Motivations for Novel PET Systems for Human Imaging 7

2 Contributions **9**
2.1 Innovative PET Systems 9
2.2 Collaboration with Other Colleagues 12

3 List Mode GPU-based Image Reconstruction Framework for PET with Flexible Geometry **14**
3.1 Introduction, Background and Motivation 14
3.2 Penalized EM using Trust Region Newton's Method 15
3.3 Multi-GPU Implementation 19
3.3.1 The GPU computing architecture overview 19
3.3.2 On-The-Fly Projection Kernel 21
3.3.3 Multi-GPU Scalability 23
3.4 Extensions 27
3.4.1 Dynamic Geometry 27
3.4.2 OSEM and Parallelization 28
3.5 Application to Different Systems 29
3.5.1 Plant PET System 30
3.5.2 Micro Insert - Micro PET System 31
3.5.3 Siemens Biograph 40 Clinical Scanner 32

3.6 Performance Comparison with Previous Work . . . 38
3.7 Conclusion and Summary . . . 40

4 Second Generation Robot Controlled Virtual Pinhole PET . . . 44
4.1 Introduction and Background . . . 45
4.2 Integration of Robotic Controlled Flat Panel Insert with Clinical Scanner . . . 48
4.2.1 High Resolution Flat Panel PET Insert . . . 49
4.2.2 Integration of Insert and Robotic Arm . . . 51
4.2.3 Establishing the Coordinate System of Whole Body Scanner . . . 51
4.2.4 PET Data Based Coordinate System Calibration . . . 52
4.3 Image Reconstruction for Second Generation Robot Controlled VP-PET . . . 54
4.3.1 Geometry Modeling . . . 54
4.3.2 Incorporating Robotic Information into Reconstruction . . . 57
4.3.3 Data Correction . . . 58
4.4 Methods . . . 61
4.4.1 Monte Carlo Simulation using GATE . . . 61
4.4.2 Experimental Phantom Study . . . 63
4.5 Results . . . 65
4.5.1 Simulation Results . . . 65
4.5.2 Experimental Results . . . 72
4.6 Discussion . . . 74
4.7 Conclusion . . . 76
4.8 Future Development of Robotic VP-PET . . . 77
4.8.1 Targeted ROI imaging . . . 77
4.8.2 Safety Concern . . . 78
4.8.3 Adaptive Scan . . . 78

5 A Feasibility Study of a Point-of-Care PET System . . . 80
5.1 Introduction . . . 81
5.2 Methods . . . 84
5.2.1 Prototype System Design . . . 84
5.2.2 Monte-Carlo Simulation . . . 88
5.2.3 Image Reconstruction . . . 91
5.2.4 Scan-Reconstruction-Rescan . . . 95
5.3 Results . . . 96
5.3.1 Non-TOF Prototype Experiment and Simulation . . . 96
5.3.2 POC-PET Simulation Scenario 1 . . . 98
5.3.3 POC-PET Simulation Scenario 2 . . . 101
5.3.4 Scan-Reconstruction-Rescan . . . 104
5.3.5 A Panel - Half Ring Scanner Example . . . 106
5.4 Discussion and Conclusion . . . 110

References **114**

Vita **122**

List of Tables

3.1 Notations 15
3.2 Image reconstruction parameters for 3 different PET systems 29
3.3 Comparison between GPU and CPU image reconstruction for clinical scanner 40

5.1 Image reconstruction parameters for 3 systems 95

List of Figures

3.1 Illustration of CPU and GPU architecture, figure from CUDA programming guide v8.0 http://docs.nvidia.com/cuda/cuda-c-programming-guide 20
3.2 Comparison between the CPU and GPU computation power in terms of single precision FLOPS and memory bandwidth, figure from Karl Rupp's blog available at https://www.karlrupp.net/2013/06/cpu-gpu-and-mic-hardware-characteristics-over-time/ 22
3.3 (a) Illustration of TOR intersection with the volume. For X oriented events, YZ planes are used to calculate their intersections. (b) TOR intersection with a single slice, with number of intersected voxels bonded. Distance of voxel to TOR center is calculated by looping through all the intersected voxels. . . . 24
3.4 Block diagram of (a) the forward and backward projection implemented on a single GPU card and (b) the implementation of image reconstruction on multi-GPU. 25
3.5 Comparison of image reconstruction time per iteration when different numbers of GPUs are used. 26
3.6 One slice of the 3D maximum intensity projected reconstruction images at 15th iteration for a Venus flytrap using data acquire by plant PET system with (a) 14 million counts and (b) 1.6 million counts. 30
3.7 One slice of the 3D maximum intensity projected reconstruction images at 10th iteration for a (a) line source and (b) two ^{68}Ge spherical bead sources imaged by the standalone insert system. 31
3.8 (a) Experiment phantom imaged by Siemens Biograph 40® clinical PET-CT and (b) Illustration of the spherical tumors arrangement in the phantom. . . 32
3.9 Reconstructed images of the phantom via standard clinical software using (a) filtered back projection (b) OSEM method of 2 iterations and 24 subsets (c) OSEM method of 8 iterations and 4 subsets (d) OSEM method of 8 iterations and 4 subsets with PSF TrueX algorithm. 33
3.10 Experiment phantom reconstructed image by (a) Siemens Biograph 40® clinical PET-CT and (b) GPU list mode reconstruction with no penalty and (c) GPU list mode reconstruction with smoothness penalty. Images are reconstructed using roughly the same number of coincidence counts and shown at the same window level. 35
3.11 Plot of profiles for the Siemens Biograph 40® and GPU reconstructed images. 36

3.12 GATE simulated phantom reconstructed image by (a) previously developed CPU based reconstruction without penalty and (b) GPU list mode reconstruction without penalty; (c) GPU list mode reconstruction with penalty; (d) GPU list mode reconstruction with TOF information (TOF FWHM = 528 ps) without penalty; (e) GPU list mode reconstruction with TOF information with penalty. 41
3.13 Plot of profiles of reconstructed images by CPU and GPU with different parameters. 42

4.1 (a) Detector blocks arranged in 8×4 array inside the case, compared with a cell phone with 5.5 inch screen. (b) Internal view of block detectors and crystals. (c) Front view and (d) back view of the panel and tube holder assembly. 50
4.2 Customized alignment tool guided by force-torque sensor automatically searching for best contact with the metal back panel of the scanner (a) during the searching process and (b) firm contact is made and TCP is recorded for coordinate system calculation 53
4.3 FWHM of the tube-of-response from the front facing insert-scanner crystal pair 56
4.4 Cylindrical phantom with spherical tumors of different sizes simulated. . . . 62
4.5 (a) Configuration of VP-PET in GATE simulation. Insert panel at 5 positions are shown. (b) Configuration of scanner only in GATE simulation. 63
4.6 ^{18}F solution filled phantom 64
4.7 Reconstructed images at 30th iteration of 200 seconds equivalent simulation data with no penalty by (a) scanner only and (b) VP-PET using SS data set 1 only and (c) VP-PET using SS data set 2 only. 66
4.8 Plot of line profiles comparing images in Figure 4.7. 67
4.9 Reconstructed images at 30th iteration with no penalty by VP-PET using SS simulation data only of (a) 200 seconds and (b) 400 seconds and (c) 800 seconds data. Reconstructed images at 30th iteration with no penalty by VP-PET including Insert-Scanner data of (d) 200 seconds data. 68
4.10 Plot of line profiles of Monte Carlo simulation VP-PET images reconstructed with no penalty in Figure 4.9. 69
4.11 Reconstructed images at 30th iteration of 200 seconds equivalent simulation data with penalty by (a) scanner only. Reconstructed images at 30th iteration with penalty by VP-PET using SS simulation data only of (b) 200 seconds and (c) 400 seconds and (d) 800 seconds data. Reconstructed images at 30th iteration with penalty by VP-PET including Insert-Scanner data of (e) 200 seconds data. 70
4.12 Plot of line profiles of Monte Carlo simulation VP-PET images reconstructed with penalty in Figure 4.11. 71
4.13 Reconstructed images at 30th iteration of 200 seconds equivalent experimental data with no penalty by (a) scanner only and (b) VP-PET using SS data only and (c) VP-PET using both SS and IS data. 73

4.14 Reconstructed images at 30th iteration of 200 seconds equivalent (a) experimental data and (b) simulation data, with no penalty by VP-PET using only IS data. 74

5.1 (a) LYSO crystals, light guide, MPPC detector and resistor network on a flexboard. (b) Crystal segmentation of the 20 × 20 flood image 85
5.2 MPPC detector mounted on the microscribe in coincidence with a half ring Inveon detectors. 86
5.3 Illustration of the scanning scheme of POC-PET Simulation Scenario 1 (a) showing the scanning trajectory of the front(top) panel (b) showing the system definition in GATE 89
5.4 Illustration of the scanning scheme of POC-PET Simulation Scenario 2 . . . 91
5.5 Illustration of scanning trajectory drawn in Matlab (a) side view, (b) top view 97
5.6 Reconstructed image of (a) experimental data, (b) Monte Carlo simulation . 98
5.7 Reconstructed images for a body phantom with Derenzo-like pattern rods with different contrast ratio and CRT imaged by POC-PET design in 5.2.2.2: (a) contrast ratio 11:1, CRT 282 ps and (b) contrast ratio 21:1, CRT 282 ps and (c) contrast ratio 11:1, CRT 717 ps and (d) contrast ratio 21:1, CRT 717 ps. 100
5.8 Reconstructed images for a body phantom with Derenzo-like pattern rods with different contrast ratio imaged by POC-PET design in 5.2.2.2 with CRT 282 ps: (a) contrast ratio 6:1 and (b) contrast ratio 11:1 and (c) contrast ratio 21:1 and (d) zero background activity. 102
5.9 (a) The position of profiles related to the phantom. Plot of line profiles for images in Figure 5.8: (b) line profile A and (c) line profile B and (d) line profile C. 103
5.10 Reconstructed images for a body phantom with Derenzo-like pattern rods with different contrast ratio imaged by POC-PET design in 5.2.2.3: (a) Contrast ratio 6:1 (b) Contrast ratio 11:1 (c) Contrast ratio 21:1 (d) No background activity. 105
5.11 Image reconstructed at 15th iteration of 21:1 background activity using CRT 282 ps from data set acquired at (a) 1st group of positions, (b) 1st and 3rd group of positions, (c) 1st, 3rd and 5th group of positions, (d) all groups of positions. 107
5.12 Line profile for reconstructed images in Figure 5.11.(a) The position of profiles A, B and C related to the phantom. Line profiles showing the voxel value of (b) line profile A, (c) line profile B, (d) line profile C, in images reconstructed using different groups of data. Line profiles A, B and C in images reconstructed from (a) 1st group of data, (f) 1st and 3rd group of data, (g) 1st, 3rd and 5th group of data. 108

5.13 Experiment setup of using robotic controlled flat panel detector together with Siemens Biograph 40 whole body scanner to demonstrate the idea of Point-Of-Care PET 109
5.14 (a) Sensitivity image showing the relative position between panel positions and the phantom. (b) The 20th iteration of ML reconstructed images using panel-scanner only prompt events 110

Acknowledgments

I would like to express my sincere gratitude to my research advisor, Dr. Joseph A. O'Sullivan and Dr. Yuan-Chuan Tai, for their patient guidance and continuous support of my Ph.D. research at Washington University. I have been so lucky to have two professors who supervise me on the theoretical and experimental side respectively. Without their support, I would not have access to the immense knowledge base and research resources.

A special thanks goes to Dr. Aswin John Mathews, a former Ph.D. graduate from our lab, for his generosity in helping me get started on my research and understanding the image reconstruction techniques. A special thanks goes to Dr. Qiang Wang and Jie Wen for their generous help on making all the hardware electronics ready. I wish to thank former and current members in my lab, including Dr. David Politte, Dr. Sergey Komarov, Dr. Bosky Ravindranath, Dr. Ikenna Odinaka, Dr. Jianyong Jiang, Dr. Yaqi Chen, Dr. Soysal Degirmenci, Dr. Tianpeng Xu, Homayoon Ranjbar, Jingwei Lu, Shouyi Wei, Ayan Mitra, Shuangyue Zhang and Linyun He, for the insightful discussions with them. I'm also thankful to the undergraduate students whom I worked together with, for their contributions to the Virtual Pinhole PET project. I appreciate the help from Malcolm Tobias for his valuable help on running my programs on the CHPC.

The work was supported in part by the National Institute of Health (R01-CA136554), the National Science Foundation (DBI-1040498, IIA-1430428) and the Department of Energy

(DE-SC0005157). Part of the computations were performed using the facilities of the Washington University Center for High Performance Computing, which were partially provided through NIH grant (S10 OD018091).

Ke Li

Washington University in Saint Louis
Aug 2017

Dedicated to my beloved parents.

ABSTRACT OF THE DISSERTATION

Novel PET Systems and Image Reconstruction with Actively Controlled Geometry

by

Ke Li

Doctor of Philosophy in Electrical Engineering

Washington University in St. Louis, Aug 2017

Research Advisor: Joseph A. O'Sullivan, Yuan-Chuan Tai

Positron Emission Tomography (PET) provides in vivo measurement of imaging ligands that are labeled with positron emitting radionuclide. Since its invention, most PET scanners have been designed to have a group of gamma ray detectors arranged in a ring geometry, accommodating the whole patient body. Virtual Pinhole PET incorporates higher resolution detectors being placed close to the Region-of-Interest (ROI) within the imaging Field-of-View (FOV) of the whole-body scanner, providing better image resolution and contrast recover. To further adapt this technology to a wider range of diseases, we proposed a second generation of virtual pinhole PET using actively controlled high resolution detectors integrated on a robotic arm. When the whole system is integrated to a commercial PET scanner, we achieved positioning repeatability within 0.5 mm. Monte Carlo simulation shows that by focusing the high-resolution detectors to a specific organ of interest, we can achieve better resolution, sensitivity and contrast recovery.

In another direction, we proposed a portable, versatile and low cost PET imaging system for Point-of-Care (POC) applications. It consists of one or more movable detectors in coincidence

with a detector array behind a patient. The movable detectors make it possible for the operator to control the scanning trajectory freely to achieve optimal coverage and sensitivity for patient specific imaging tasks. Since this system does not require a conventional full ring geometry, it can be built portable and low cost for bed-side or intraoperative use. We developed a proof-of-principle prototype that consists of a compact high resolution silicon photomultiplier detector mounted on a hand-held probe and a half ring of conventional detectors. The probe is attached to a MicroScribe device, which tracks the location and orientation of the probe as it moves. We also performed Monte Carlo simulations for two POC PET geometries with Time-of-Flight (TOF) capability.

To support the development of such PET systems with unconventional geometries, a fully 3D image reconstruction framework has been developed for PET systems with arbitrary geometry. For POC PET and the second generation robotic Virtual Pinhole PET, new challenges emerge and our targeted applications require more efficiently image reconstruction that provides imaging results in near real time. Inspired by the previous work, we developed a list mode GPU-based image reconstruction framework with the capability to model dynamically changing geometry. Ordered-Subset MAP-EM algorithm is implemented on multi-GPU platform to achieve fast reconstruction in the order of seconds per iteration, under practical data rate. We tested this using both experimental and simulation data, for whole body PET scanner and unconventional PET scanners. Future application of adaptive imaging requires near real time performance for large statistics, which requires additional acceleration of this framework.

Chapter 1

Introduction

This chapter starts from the basic knowledge of Positron Emission Tomography (PET), including the underlying physics, the electronics related technology and image reconstruction algorithm and computational methods. Then it briefly goes through the history of the development of PET and the currently ongoing PET system development. This is important because the evolution of PET motivates my research work and some ongoing development takes on a different approach to solve some similar problems.

1.1 Fundamental Physics of Positron Emission Tomography

PET is an in vivo tomographic imaging technique to measure the radioactive source distribution in the body. A typical PET scan of a patient starts with injection of positron emitting radionuclide into the patient body. The radionuclide undergoes a positron emission decay in which a proton converts to a neutron while releasing a positron, a type of beta particle. After randomly traveling a short distance inside the patient tissue, the positron will collide

with a electron to form a intermediate unstable state called positronium, which quickly turn into a pair of gamma photons in the annihilation. The energy of the two gamma photons are determined by mass energy equivalence of the two beta particles, to be 511 KeV each. Clinically, fludeoxyglucose F 18 (^{18}F-FDG) is widely used for PET scans because it is a marker of tissue uptake of glucose. With increased uptake by cancer cells, ^{18}F-FDG PET image provides a visualization of glucose metabolism of the patient.

Such physical process has some intrinsic limiting factors of resolution for PET. The random path taken by the emitted positron before annihilation depends on the initial kinetic energy and the tissue density. This distance is called positron range. For example, positrons emitted from ^{18}F-FDG has a mean positron range of 0.27 mm in soft tissue [47]. It causes the loss of information of the original radionuclide location and limits the accuracy of the final reconstructed PET image. In addition to positron range, the kinetic energy also causes the non-collinearity effect due to conservation of momentum, meaning that the pair of gamma photons are not exactly back-to-back. Since we always reconstruct the image by assuming the gamma photons are back-to-back, this small random deviation in the angle will finally propagate into the image resolution. The severity of this problem depends on the diameter of the scanner ring and this blurring component is commonly calculated by $0.0022D$ where D is the diameter [57].

1.2 Detection and Data Acquisition

Single photon based nuclear imaging techniques such as Single Photon Emission Computed Tomography (SPECT) uses absorptive collimation to regulate the incoming photon and use the directional information for image reconstruction. In comparison, PET uses electronic

collimation [39], or coincidence detection of emitted gamma photon pairs, to localize the radionuclide source. Without the absorption of photons by the collimator, more photons can be used for image reconstruction thus the sensitivity is usually much higher for PET. Coincidence detection is done by applying a coincidence timing window in the data acquisition system. As streams of photons detection coming to the coincidence processor, time of arrival of any pair of detected photons are compared. They will be recorded as a coincidence pair as long as they fall in a certain time window. If the data rate is too high and more than two photons falls into the same coincidence windows, they are handled by a multiple-coincidence routine. The width of the time window is usually picked according to a series of factors: data count rate, number of data channels, size of FOV and the system timing resolution. If two photons fall into the same time window while not coming from the same annihilation event, they will still be recorded as coincidence events and we call these random coincidence events, which need to be treated in image reconstruction.

1.3 Monte Carlo Simulation

Various Monte Carlo simulation software package have been developed and used for nuclear imaging (PET, SPECT) including Geant4 [1, 2, 3], SimSET [17] and GATE [26, 27]. Geant4 is a general purpose Monte Carlo simulation package that provide most features and is widely used in high energy physics research and detector design. It simulates comprehensive process in particle physics using well validated models, providing precision and accuracy in quantitative study. It also provides the most flexibility that Geant4 can be customized to simulate any geometry. But the gain in flexibility comes at a cost of user friendliness and simulation speed. SimSET partially solved this problem by making itself a dedicated

simulation package for PET and SPECT with limited flexibility in geometry and limited functions that a user can control during simulation.

A good balance between Geant4 and SimSET is GATE, an open source Monte Carlo simulation software package developed by the OpenGATE collaboration. It is now most widely used by the nuclear imaging (PET, SPECT) research community, though it is also capable of simulating Computed Tomography (CT), Optical Imaging (Fluorescence) and Radiotherapy process. In terms of PET, GATE is capable of simulating almost any geometry while only requires simple scripting instead of complex programming.

1.4 Image reconstruction for PET

Like other tomographic imaging techniques such as Computed Tomography (CT), PET image reconstruction can be categorized into analytical reconstruction and statistical/model based reconstruction. In PET, statistical image reconstruction uses Poisson model to explain the underlying radioactive decay process and models the image reconstruction task into a function optimization problem. Usually, iterative methods such a Expectation Maximization (EM) are used to solve the problem. Compared to analytical reconstruction, model based image reconstruction can incorporate more complex prior information and data correction techniques. However, by solving it iteratively, the computation is very intensive when a large number of iterations are needed.

1.5 Evolution of PET Design

Since the invention of PET, most PET scanners are designed in a ring shape to meet more generic demands. The image resolution of PET was very low compared to CT and MRI. Improving the image quality has been always a very important research area for PET. The most direct path to better image quality is to use detectors with better intrinsic resolution and detection efficiency. With so many limitations and constrains in designing a whole body PET, designing PET systems for certain specific applications also provides a viable answer to this problem. In the recent years, driven by the improvement of detector technology and computational techniques, more and more PET systems with interesting geometry designs start to show their benefits in specific applications.

Clinical PET Scanner In clinical application, PET is mostly used to perform whole body scan from skull to thigh for cancer staging. Driven by this demand, commercial whole body clinical PET scanners usually have gantries of large size to accommodate most patient bodies. Constrained by the cost of detectors and the overall sensitivity required, clinical whole body PET systems usually use scintillation crystals of large pitch size (more than 4 mm) and long axial length(20 mm). The pitch size limits the best intrinsic spatial resolution while the larger axial length degrades the spatial resolution off the scanner center. Additionally, larger FOV introduces more significant degradation in resolution due to photon non-collinearity effect, which theoretically limits the highest possible image resolution for a regular clinical PET scanner (with ring diameter larger than 80 cm) to be no better than roughly 2 mm FWHM. Since PET is a count limited imaging technique, image quality heavily depends on the counting statistics. We talk about image quality considering a practical number of counts. Empirically, a common clinical scanner can provide best image resolution at around 4-6 mm

FWHM at the center of FOV. Considering post smooth filtering applied, the resolution is worse. As a result, recent advances in whole body PET research and development has been focused more on areas other than applying detectors with better intrinsic resolution, such as using Time-Of-Flight (TOF) to increase contrast recovery and integration of PET to MRI.

Application Specific PET Systems The need for detecting small lesions greatly motives researchers to overcome the resolution and sensitivity limitation of whole body PET. Application specific PET systems have been proposed and commercialized to address this problem. For example, PET for breast imaging, Positron Emission Mammography (PEM) uses detectors of higher resolution placed around the breast to get resolution of below 3 mm FWHM [34, 64]. It is shown that using this technology can improve the sensitivity of detection of tumors various sizes and the decrease of sensitivity of detection with the decreasing tumor size is not significantly affected in PEM, which is not the case in whole body PET [28]. While these advantages are exciting, we also understand that these application specific PET systems have limited FOV and the quantitative acurracy is saptial variable due to the limite angle sampling and lack of data correction techniques [34]. Besides PEM, there are few application specific systems commercialized for clinical use. The requirement for developing one system for each specific organ or application greatly increases the cost.

Emission Tomographic Systems with Dynamically Changing Geometry Besides building application specific PET to improve the image quality, another attempt has been taken in recent years to extend the application area of PET beyond traditional cancer staging. Novel radioactive tracer development allows PET to be used for many other diseases and purpose. Intraoperative emission tomographic systems have developed to bring nuclear imaging into the operation room. These systems include SPECT, gamma camera and PET,

sharing the similar concept that they are operated directly by the technician in a flexible scanning path. Their detectors are lightweight, movable and tracked accurately, making it possible to get closer to the organ of interest for any patient. Similar idea applies to a system integrated with ultrasound endoscope to achieve best sensitivity for pancreas caner via an invasive approach [40, 4]. All these systems have dynamically changing geometry to provide flexibility and to overcome the limited sampling angle problem. The position information of detectors are taken into account in image reconstruction and data correction so an accurate and robust tracking mechanism is highly desirable.

1.6 Motivations for Novel PET Systems for Human Imaging

Since we have several systems developed under the virtual-pinhole PET (VP-PET)concept, we started to think how to make improvements and push the limitation of PET. For example, the first generation of VP-PET [29] has a half ring geometry, which provides good detection sampling coverage but sacrifices the flexibility while using it. In some of the patient studies, it was found that some patient cannot easily fit their head and neck into this half-ring insert, which made it difficult to position the Region-Of-Interest (ROI) inside the insert enhanced region. The bulky insert itself is mounted on a heavy-duty 3 dimensional translation stage, limiting its application to other parts of a body. To solve this issue, we have been designing a flat panel insert for imaging metastatic lymph nodes of breast cancer patients [44]. To maximizing its flexibility, we decided to control it with a robotic arm, which will virtually allow us to use the insert for arbitrary ROI of the patient.

After we achieved the capability of doing image reconstruction for PET system with arbitrary geometry, we start to think how to use this tool to help us move forward. I noticed that the reconstruction running on clusters are not quite easy to use due to a long queuing time. As computing power is shifting from CPU clusters to GPU, I got the motivation to transfer the existing codes from CPU to GPU architecture, still maintaining the capability to handle arbitrary geometry. Another motivation to develop this tool was our dedicated plant PET system. That system is used for routine experiments of a large amount of plant science studies, which require individual reconstruction for different time frames in order to do dynamic analysis. Near-real time image reconstruction capability will be greatly beneficial to these studies.

With the capability of doing image reconstruction by list-mode and incorporating dynamically changing geometry information, I started to think this could open a new area of PET applications. Our Point-Of-Care PET shares similar concept and approach with the EndoTOFPET-US project [5] but with totally different emphasis and application. The EndoTOFPET-US combines PET imaging with ultrasound endoscope and its aim is to have early phase detection of the deadly pancreatic cancer. However, due to its very small detector design, and the movement range of the endoscope, it can hardly provide enough sampling angles for a tomographic image. It heavily relies on its state-of-art Time-Of-Flight (TOF) detector and the proximity to the tumor guided by the ultrasound endoscope. Instead, our Point-Of-Care PET provides a non-invasive approach that only scans outside of the patient. To solve the limited sampling angle problem, we use precise mechanical tracking device that allows us to move the PET detector around the ROI as much as we can. Without going inside the patient, our detector could be made much bigger and more technologies could be used to achieve the goal.

Chapter 2

Contributions

2.1 Innovative PET Systems

GPU-based Fast Image Reconstruction for Unconventional PET Geometry This project serves as an important tool throughout my research. Before I started this project, Dr. Mathews and I together debugged and set the workflow of the generalized image reconstruction framework developed by Dr. Mathews [37]. In addition to the original code base, I implemented the Gaussian TOR (Tube-Of-Response) forward model and compared that with the original multi-ray Siddon's projector, which turns out to give comparable results at faster computational speed. Then I implemented the list-mode objective function to satisfy the need for reconstruction of Plant PET data segmented by time frames. This feature greatly improved the flexibility to conduct dynamic imaging study for plant science.

Since then, we were facing another issue, the computation and queuing time of the WUSM CHPC computing cluster. Since our implementation requires large memory to hold the system matrix, we need to request one of the eight nodes with large shared memory on CHPC and usually we could not start our reconstruction quickly. So with this motivation

I started to port the code base to Nvidia GPU architecture using CUDA programming standard. It turns out that the original multi-ray Siddon's projector is not suitable for GPU architecture but the Gaussian TOR projector is a very good fit. The GPU version naturally takes list-mode (also histogram-mode) as input and uses on-the-fly projector computation. A major part of the original reconstruction framework, automatic symmetry identification, is removed as it is no longer needed for list-mode on-the-fly projector.

The first system that we applied this reconstruction to is the plant PET, with a fixed geometry. My colleagues benefits a lot from the fast image reconstruction which enables them to see the image reconstructed as the PET data acquisition is going on. They also use this tool to verify the accuracy of the object position and the quality of the radioactive absorption. Based on the success of using this GPU based image reconstruction on a static geometry system, I started to make it work on moving geometry to support my other research projects. It also has the flexibility to reconstruct a insert-scanner system with either static or moving insert position. Through out the following years I optimized the code by using many new features came with the newer generation of GPU such as atomic operation, unified virtual addressing, unified memory and multi-GPU. The latest version of the code is optimized to run on 4 Nvidia GTX Titan X (Maxwell Architecture). It is now used for image reconstruction of our routine plant science experiments and our robot controlled ACTIV PET. As PET is a complex system that involves a lot of physical process, it takes years of effort to develop a relatively complete image reconstruction framework, especially for PET with unconventional geometry. My GPU-based image reconstruction framework has been tested on multiple systems, including both conventional and unconventional PET, both experimental system and commercial clinical system. However it requires further development to improve the quantitative accuracy.

Point-Of-Care PET This project is largely motivated by our experience of using a MicroScribe® (referred as microsribe in this thesis) with a laser scanner device to digitize the contour of an object. I started to think whether we can build a maneuverable PET scanner with detectors that could be moved freely by hand, while using the microscribe to track the detectors. The ideal use case will be that a technician guides this maneuverable PET scanner to cover a scanning contour of a ROI (Region-Of-Interest) of the patient, with a real time image reconstruction engine that reconstructs the refreshed PET images as the scanning trajectory is being adjusted. This is a very similar concept used in some other imaging modalities such as ultrasound and intraoperative gamma camera. However in the PET field, there were very few demonstrations of similar concept, possibly due to some limitations of Positron Emission Tomography itself. It is made possible since I have a very fast GPU-based list-mode image reconstruction as well as the hardware resources to build such a tracked PET detector. I designed and built a small prototype system using in-house detectors and integrated it to the data acquisition system of our plant PET (Siemens Inveon QuickSilver electronics). I also studied several designs by using Monte-Carlo simulation package GATE. Both experiments showed promising results and the image reconstruction speed (only 1 GPU card of previous Kepler architecture) was well within the range that could be improved to near real time.

Second Generation Robot Controlled VP-PET The second generation robot controlled VP-PET was originally a natural extension of the first generation VP-PET system. That system has an insert of half-ring geometry mounted on a three dimensional translation stage and was specifically designed for head and neck cancer imaging. Our group designed the second generation insert to be a flat panel geometry in order to be applicable to a wider variety of patients and other types of cancer imaging. In order to make it more flexible,

we decided to use a 6-DOF robot instead of the translation stage. I started to work on the Monte Carlo simulation of this system in December 2014 and to make adjustment to my reconstruction code for this insert geometry. I took the KUKA robot training in June 2015. During the following year, I worked with 2 undergraduate students to design the entire procedure to integrate the flat panel detector to the robot and precisely into the Siemens Biograph 40® clinical scanner at the Center for Clinical Imaging Research (CCIR). Starting from July 2016, I worked on multiple experiments to test the integrated robotic VP-PET system, designed a calibration procedure to minimize the positioning error and acquired data for reconstruction. I reconstructed images from different types of data acquired by this real system and proved the basic functions of the whole framework for future clinical research by this robotic VP-PET prototype.

2.2 Collaboration with Other Colleagues

Here I briefly describe some other projects that I have participated in.

Framework for Arbitrary Geometry Reconstruction Starting from August 2012, the first project I worked on was to debug the code base for the image reconstruction framework under arbitrary geometry and to optimize the work flow of doing image reconstruction using this package.

Unconventional Geometry PET System As other colleges continued developing I helped to apply this image reconstruction to 4 different PET systems: plant PET, micro

Insert, prototype flat panel insert and the half-ring VP-PET. I went through several experiments in the plant imaging lab and the clinical scanner at CCIR (Center of Clinical Imaging Research).

Optimize and Implement the Penalized Reconstruction for Mars Surface Imaging Starting Oct 2014, I worked part time on a Mars surface imaging project which uses very similar statistical model and optimization algorithms as PET. I used parallel computing techniques to accelerate the original Matlab code by a factor of nearly 150. I also implemented the Trust Region Newton's method to help make the spatial and spectral profiles smoother.

Chapter 3

List Mode GPU-based Image Reconstruction Framework for PET with Flexible Geometry

3.1 Introduction, Background and Motivation

Our lab at WUSM has a history of developing the image reconstruction algorithm and software implementation for customized PET systems. We started from 2D linear and iterative algorithms [38] for a ring-shape insert, then 3D statistical iterative method for a half-ring insert [29] and came to a fully 3D statistical iterative algorithm for an arbitrary geometry [37]. A major motivation for developing in-house image reconstruction is that we build PET systems with unconventional geometries, and we want to use PET insert with more flexibility. Our needs make it difficult to use open source packages such as STIR [58].

The

As an important part of this image reconstruction framework, this algorithm is implemented on a Graphics-Processing-Unit (GPU) computing architecture which allows massive parallelism.

3.2 Penalized EM using Trust Region Newton's Method

In this section we describe the Penalized Expectation Maximization (PL-EM) algorithm for image reconstruction of emission tomographic data. The notation in this chapter is outlined in Table 3.1.

Table 3.1: Notations

$\mathbf{X}\{X_j : j = 1, ..., J\}$	Activity distribution image
$\mathbf{Y}\{Y_i : i = 1, ..., I\}$	Prompt coincidence data
$\mathbf{H}\{H_{ij}\}$	System matrix, detector response function
$\mathbf{S}\{S_j : j = 1, ..., J\}$	Sensitivity image
$\mathbf{r}\{r_i : i = 1, ..., I\}$	Random coincidence data
$\mathbf{sc}\{sc_i : i = 1, ..., I\}$	Scatter coincidence data

The Poisson statistical model of a PET detection process is

$$Y_i = Poisson\{\sum_j H_{ij} X_j\}. \tag{3.1}$$

The image reconstruction task is to minimize the objective function, the negative log-likelihood or equivalently the I-divergence

$$L(Y|X) = \sum_i \{\sum_j H_{ij} X_j \ - Y_i \log \sum_j H_{ij} X_j \ \}. \tag{3.2}$$

In this work, we start from the standard Maximum Likelihood Expectation Maximization (ML-EM) algorithm for emission tomography [48, 31]. The update equation is

$$X_j^{(k+1)} = \frac{X_j^{(k)}}{S_j} \sum_i H_{ij} \frac{Y_i}{\sum_{j'} H_{ij'} X_j'^{(k)} + r_i + sc_i}. \tag{3.3}$$

where

$$S_j = \sum_i H_{ij}. \tag{3.4}$$

$S_j$is called the sensitivity image, which has the physical meaning describing the probability of detection of each voxel in the image space. The term $r_i + sc_i$ is the random and scatter added to the forward projection of the current image estimate. The system matrix H_{ij} describes the probability of a back-to-back photon pair emitted at the j-th voxel being detected by the i-th LOR.

List-mode image ML-EM reconstruction for emission data has been developed in the early days of PET history [50, 6], as the photon counting process of emission tomography intrinsically fits list-mode likelihood model. Here, this histogram-mode EM update equation can be simply changed into a list-mode EM update equation by changing the backward projection of the counts Y_i into individual backward projection of one count. Since there will be Y_i list-mode events detected by the i-th LOR, the addition of their backward projections will be equivalent to the original backward projection of histogram-mode data.

$$X_j^{(k+1)} = \frac{X_j^{(k)}}{S_j} \sum_m H_{i(m)j} \frac{1}{\sum_{j'} H_{i(m)j'} X_{j'}^{(k)} + r_{i(m)} + s_{i(m)}} \tag{3.5}$$

where the subscription m denotes the list-mode events and $i(m)$ denotes the corresponding LOR index that the m-th event is detected.

For penalized image reconstruction, a penalty term is added to the original data fitting term:

$$L(Y|X) = \sum_i \left\{ \sum_j H_{ij} X_j \ - Y_i \log \sum_j H_{ij} X_j \ \right\} + \beta \delta^2 \sum_j \sum_{j' \in N_j} w_{jj'} f\left(\frac{X_j - X_{j'}}{\delta} \right), \quad (3.6)$$

where the β parameter controls the overall balance between the data fitting term and the penalty term. The choice of function f affects the behavior of smoothness. Huber type loss functions are widely used since they smooth out the unwanted noise but preserve transitions in sharp edge areas [8, 51]. We use function $f(x) = logcosh(x)$ which has a Huber type behavior for computational efficiency. The δ parameter controls the transition between linear region and quadratic region of the penalty term.

By using convex decomposition on the log-sum term, it turn into sum-log with an auxiliary variable r_{ji}

$$L(Y|X) = \min_{r_{ji}} \sum_i \left\{ \sum_j H_{ij} X_j \ - Y_i \sum_j r_{ji} \log \frac{H_{ij} X_j}{r_{ji}} \right\} + \beta \delta^2 \sum_j \sum_{j' \in N_j} w_{jj'} f\left(\frac{X_j - X_{j'}}{\delta} \right), \quad (3.7)$$

where the minimization is over probabilities $\sum_i r_{ij} = 1$.

The penalty term is also decoupled using a convex decomposition to allow the update equation to work on individual pixels.

$$
\begin{aligned}
f\left(\frac{X_j - X_{j'}}{\delta}\right) &= f\left(\frac{0.5(2X_j - \hat{X_j} - \hat{X_{j'}}) + 0.5(\hat{X_j} + \hat{X_{j'}} - 2X_{j'})}{\delta}\right) \\
&\leq 0.5f\left(\frac{2X_j - \hat{X_j} - \hat{X_{j'}}}{\delta}\right) + 0.5f\left(\frac{\hat{X_j} + \hat{X_{j'}} - 2X_{j'}}{\delta}\right)
\end{aligned} \tag{3.8}
$$

To form an alternating minimization process, we first minimize the objective function on r_{ji} to get

$$
r_{ji}^{(k+1)} = \frac{H_{ij}X_j^{(k)}}{\sum_{j'} H_{ij'}X_{j'}^{(k)}}. \tag{3.9}
$$

This is equivalent to the E-step in an Expectation Maximization algorithm. Substitute $r_{ji}^{(k+1)}$ into 3.7 using 3.8, remove all of the constant terms and rearrange the order of sum to get

$$
L(Y|X)' = \sum_j S_j X_j - \sum_j X_j^{(k)} B_j^{(k)} \ln(X_j) + \beta\delta^2 \sum_j \sum_{j' \in N_j} w_{jj'} f\left(\frac{X_j - X_{j'}}{\delta}\right) \tag{3.10}
$$

$B_j^{(k)}$ is the backward projection of the ratio between data and estimated mean, normally referred as the update image. We call the entire M-step the image update step, which is independent from the projection method chosen. It works the same for both list mode and histogram mode.

For histogram mode update

$$
B_j^{(k)} = \sum_i H_{ij} \frac{Y_i}{\sum_{j'} H_{ij'}X_{j'}^{(k)}} \tag{3.11}
$$

For list mode update

$$B_j^{(k)} = \sum_m H_{i(m)j} \frac{1}{\sum_{j'} H_{i(m)j'} X_{j'}^{(k)}} \tag{3.12}$$

Note that when we put (3.8) in (3.10), all the sums are over individual image voxels thus giving us an element wise updating equation. The decoupled penalty allows us to solve the maximization step using Trust Region Newton's method on each individual voxel. This greatly reduced the computation and allows us to easily parallelize over the entire image volume.

The most computationally intensive part is to calculate S_j and $B_j^{(k)}$. Calculating S_j requires a full backward projection of system matrix (column sum) including data correction items such as attenuation correction and normalization factors. For systems with large geometry the computation speed of this becomes a limiting factor. Calculating $B_j^{(k)}$ requires a full forward projection and a full backward projection over the entire LOR space or list mode events, depending on the corresponding data mode chosen.

3.3 Multi-GPU Implementation

3.3.1 The GPU computing architecture overview

The Graphics-Processing-Unit (GPU) was invented about 20 years ago, originally to assist the CPU to do graphics related tasks. The nature of graphics rendering involves highly intensive arithmetic operations in parallel, which motivates the GPU architecture design to take a quite different approach when considering the resources on the chip. The CPU is intended for general purpose computation, which requires a lot of control logic. The compute

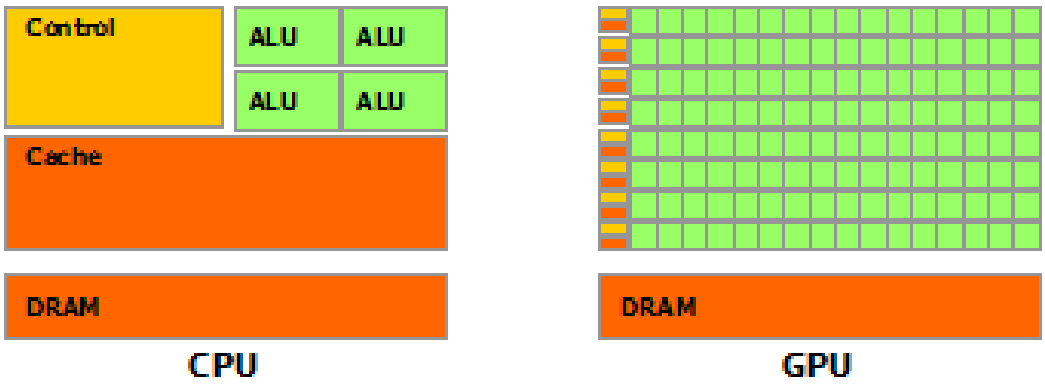

Figure 3.1: Illustration of CPU and GPU architecture, figure from CUDA programming guide v8.0 http://docs.nvidia.com/cuda/cuda-c-programming-guide

unit (ALU) is also complex enough to accomplish different kinds of computation. Through the history of CPU development, most CPUs have implemented large on-chip cache. This is because the increasing computation power requires higher data transfer bandwidth and lower memory latency, making it necessary to use cache systems to narrow down the discrepancy between the computation speed and the slow data transfer from main memory. The cache system on a typical CPU has a different hierarchy and is managed by hardware, making it transparent to the programmers. Thee complex management and large cache size consumes a lot of chip space.

However, the GPU only performs a limited number of tasks. So to increase the number of cores, a GPU has a large number of cores (ALU) with limited functions. To reduce the control unit, a GPU takes a Single-Input-Multiple-Data (SIMD) approach: multiple cores are controlled by the same control unit, which means in the programming perspective, multiple thread are going through the same execution path. In terms of cache, the GPU still maintains a hierarchical memory layout, but requires the programmer to carefully organize

the data flow to maximize the effective bandwidth, which is a challenging problem to do computations on GPU.

As a result, a newest GPU card has one order of magnitude higher floating point operations per second (FLOPS) than a newest multi-core CPU. A similar advantage holds when comparing the theoretical bandwidth. In a bandwidth-bonded application (arithmetic operation is less intensive than memory access operation), the goal is to optimize the program to get bandwidth as close to the theoretical limit as possible.

3.3.2 On-The-Fly Projection Kernel

The Siddon's ray tracing algorithm was originally used in the CPU reconstruction in our lab. While it is a very efficient algorithm to run on a CPU, it does not suit the GPU architecture because it relies on a branching operation at the boundary of each voxel. Tracing a ray through a large 3D volume involves a large number of branching operations. The GPU architecture sacrifices the control unit for more computation cores, which leads to the fact that 32 threads (in a warp) are always going through the same execution path. Too many branching operations will soon cause the threads in the same warp to diverge, significantly increasing the execution time. In our CPU reconstruction, the ray tracing algorithm makes up a major part of the computation especially when we add sub-division to compute the average interaction length by a large number of sub-LORs.

The Gaussian kernel is a method suitable for on-the-fly calculation and well fits into the massive parallelism structure of GPU platform. It is a branchless method so that warp divergence is avoided. To efficiently perform a Gaussian-kernel based projection, the intersection volume of the Tube-Of-Response (TOR) and the 3D image volume needs to be

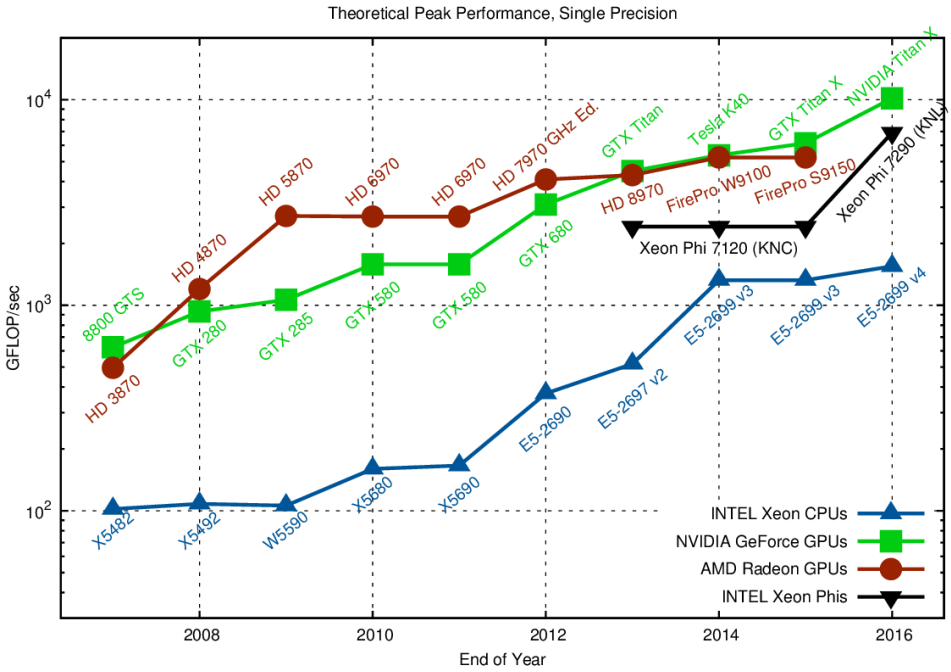

(a)

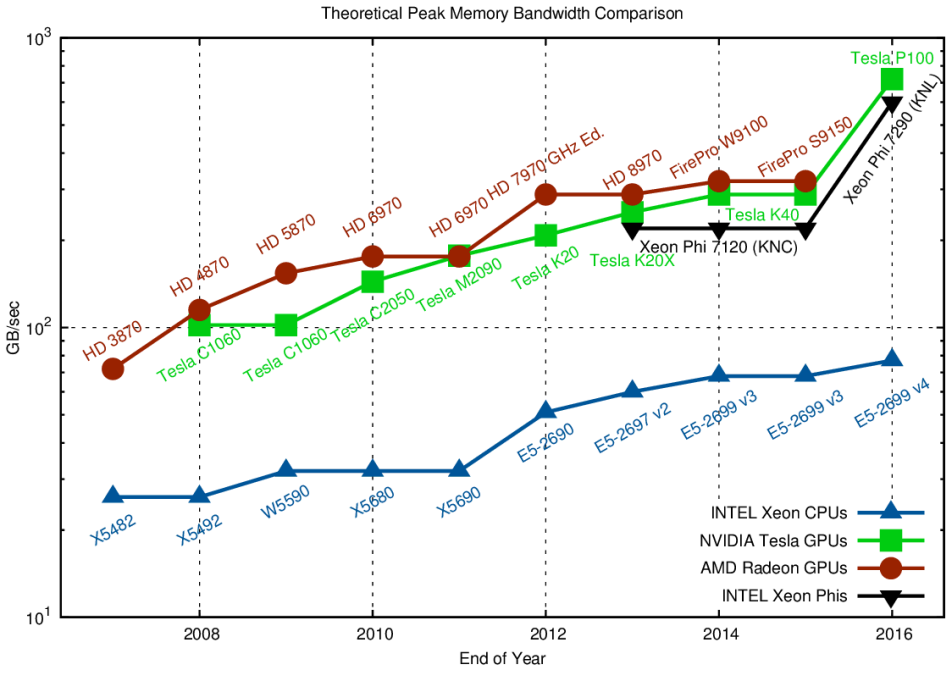

(b)

Figure 3.2: Comparison between the CPU and GPU computation power in terms of single precision FLOPS and memory bandwidth, figure from Karl Rupp's blog available at https://www.karlrupp.net/2013/06/cpu-gpu-and-mic-hardware-characteristics-over-time/

bonded in order to balance the computation on each thread [11]. We pre-sort the list mode events by its dominant direction. In most PET systems with smaller axial length than in-plane dimension, events are sorted into two grouped: oriented mostly in X direction and oriented mostly in Y direction. For the events oriented mostly in X direction, we calculate their intersection with the 3D volume per YZ plane, as shown in Figure 3.3a. For the events oriented mostly in Y direction, we use XZ planes to calculate the intersection.

In this arrangement, the intersection angle of the TOR with the plane is always kept less than 45 degrees, making the number of intersected voxels bonded by the size of the TOR, as shown in Figure 3.3b. We loop through all the intersected voxels in a single thread and compute the distance to the center of the TOR. The weighting factor of a intersected voxel to this TOR is computed by a Gaussian kernel given by

$$H_{ij}\ exp(-\frac{d^2_{j-th\ voxel\ to\ i-th\ TOR\ distance}}{\sigma^2}). \tag{3.13}$$

The σ in (3.13) is determined by the FWHM of the corresponding TOR using a Gaussian function.

3.3.3 Multi-GPU Scalability

To further improve the image reconstruction speed, a multi-GPU approach is used to perform the most computationally intensive projections simultaneously on different GPUs.

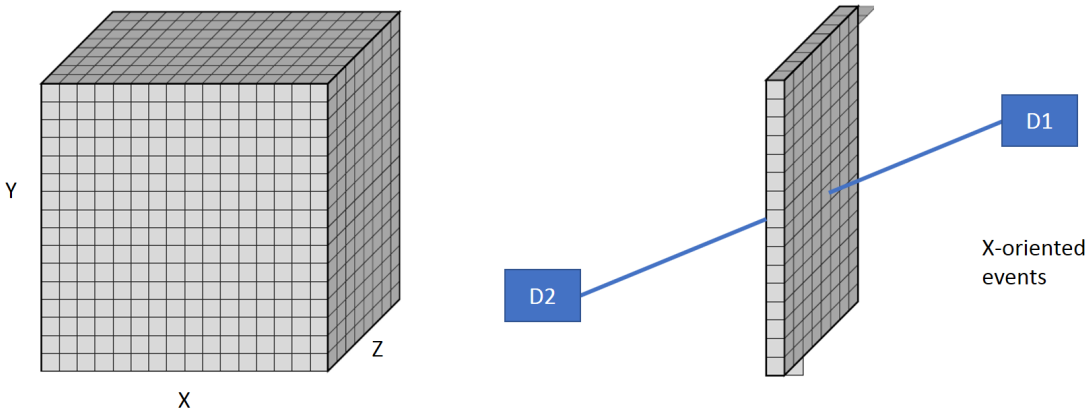

(a)

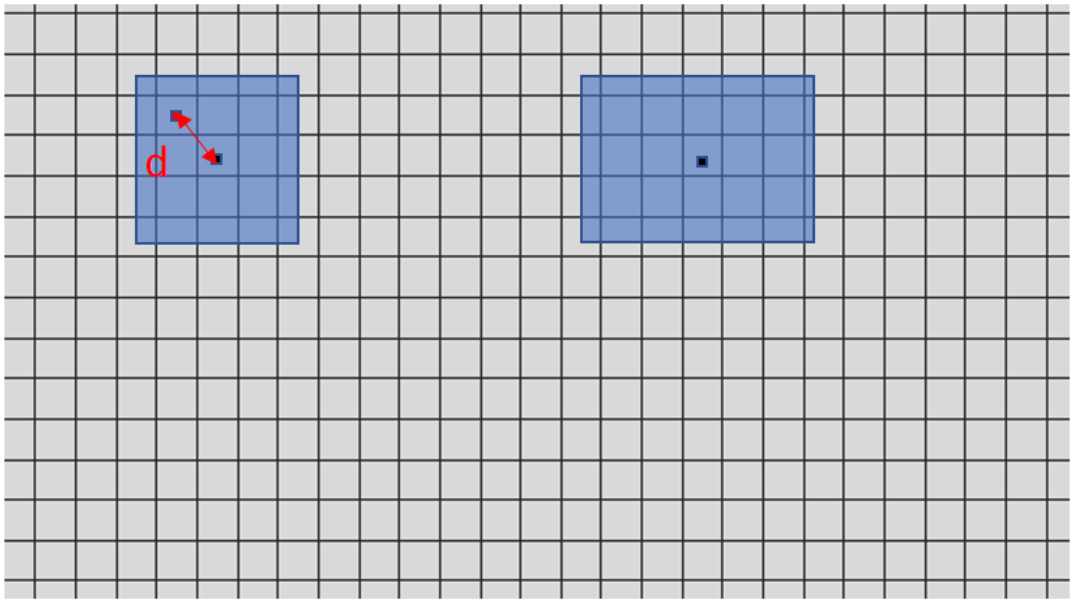

(b)

Figure 3.3: (a) Illustration of TOR intersection with the volume. For X oriented events, YZ planes are used to calculate their intersections. (b) TOR intersection with a single slice, with number of intersected voxels bonded. Distance of voxel to TOR center is calculated by looping through all the intersected voxels.

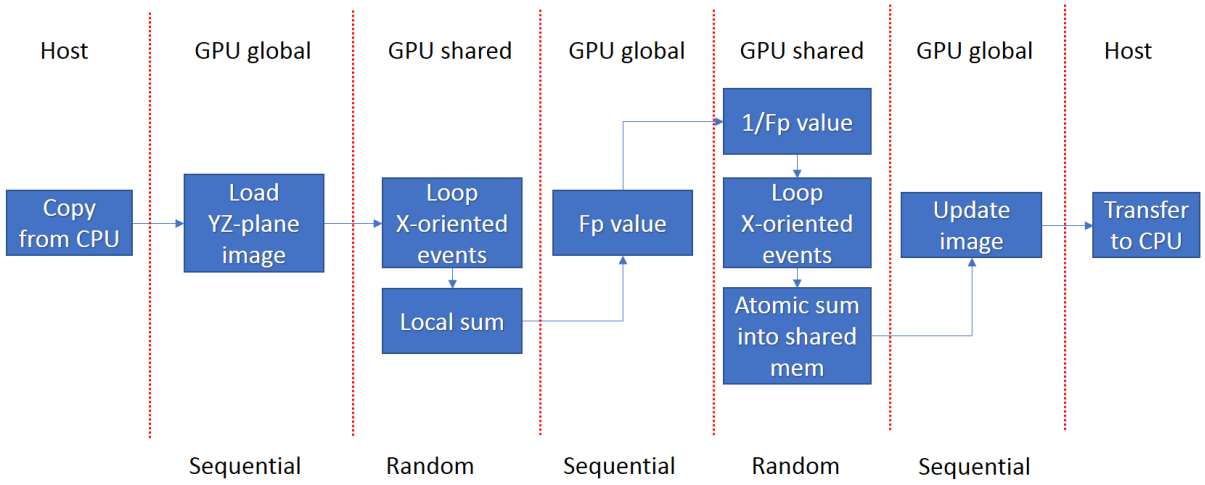

(a)

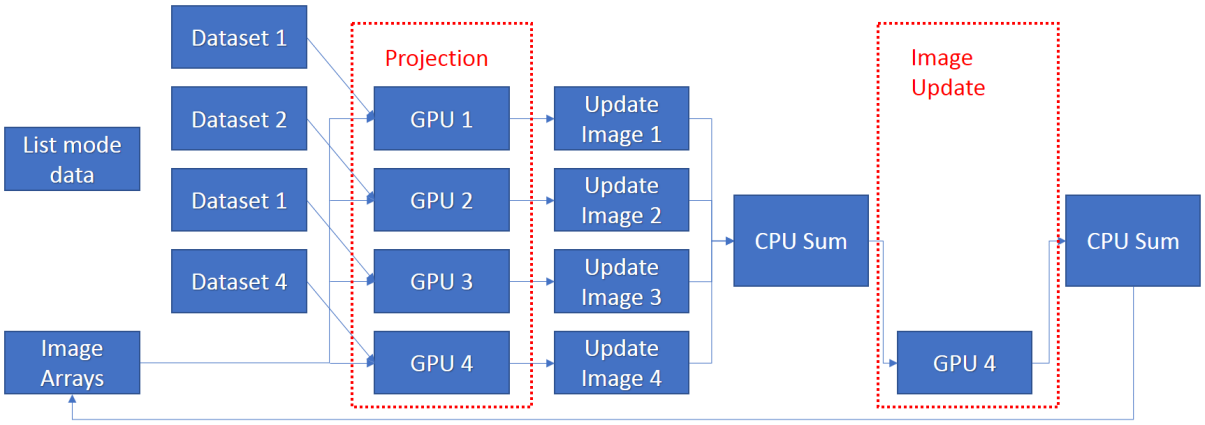

(b)

Figure 3.4: Block diagram of (a) the forward and backward projection implemented on a single GPU card and (b) the implementation of image reconstruction on multi-GPU.

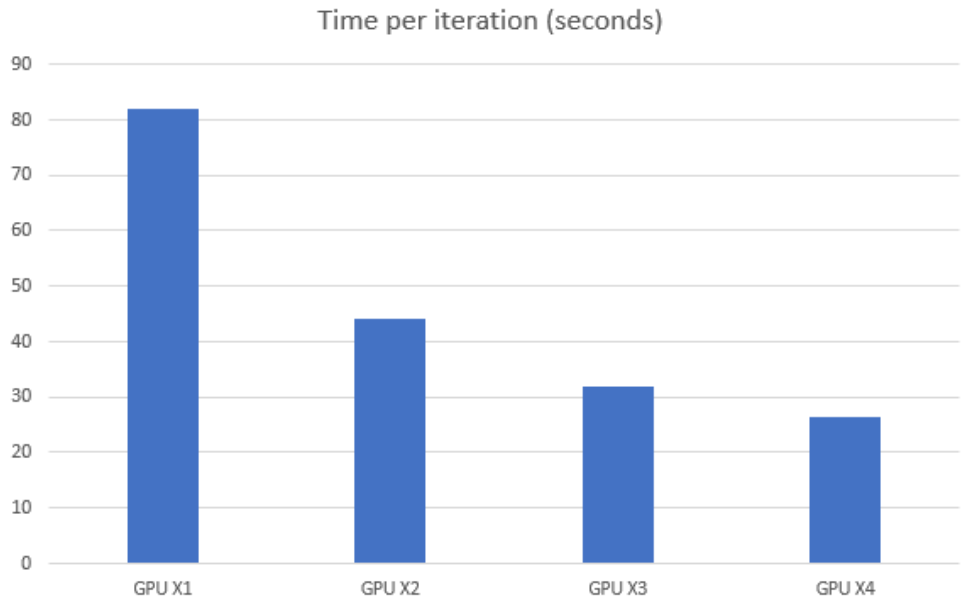

(a)

Figure 3.5: Comparison of image reconstruction time per iteration when different numbers of GPUs are used.

We tested one list mode data set using the same parameters but only changed the number of GPUs used. The image reconstruction time is measured by the difference in file written time per iteration, averaged from the first to the fifth iteration. Figure 3.5 shows a nonlinear scalability of current implementation for ML reconstruction. Compared to only using 1 GPU, we get 1.86, 2.60 and 3.12 times of the speed when using 2, 3 and 4 GPUs, respectively. The parallel portion of the implementation mainly consists of list mode forward and backward projections, is naturally segmented and distributed to multiple GPUs, and the computation is balanced. The nonlinear increase in speed is a result of the serial portion of the implementation and mainly consists of data transfer and CUDA execution overhead. For example, every iteration includes a 2 seconds of file writing, which is not improved when more GPUs are in use.

The majority of the computation is in the parallel portion, making it possible to further optimize by hiding the serial portion when computing the projections. For example, multiple CPU threads can be used to handle the data transfer between the host memory and the GPU global memory on different cards. The file writing time can also be eliminated by temporarily storing the reconstructed images in the host memory and writing during the GPU projection computation.

3.4 Extensions

3.4.1 Dynamic Geometry

It is more natural to incorporate dynamic geometry information into image reconstruction using list-mode projection than using histogram-mode projection, because each list mode event can come from any LOR randomly. To reconstruct data that is acquired when detectors are moving during the scan, we first model the scanning trajectory using a step-and-shoot approach, by recording translation and rotation vectors for each detector position along with its duration of scan in a list. For every incoming list-mode event, we read its time-of-arrival and look up this information in the list of translation and rotation using binary search method. The corresponding translation and rotation vectors are then used to transform the geometric location of the two crystals involved in this event. Forward and backward projections are done along the LOR joining these two new coordinates. Further information of incorporating this dynamic information from the robotic system are explained in Section 4.3.2.

3.4.2 OSEM and Parallelization

Traditionally, Ordered-Subset-Expectation-Mnimization (OSEM) is done through grouping the projection data into an ordered sequence of subsets [20]. To balance the coincidence counts that each subset iteration uses to calculate the update image, the most common way is to group the projection data (sinogram) by the LOR angle. Ideally the order of applying these subset projections should be arranged according to how much new information each subset could bring to the current estimate of the image [20]. However, in a conventional whole body PET system with a ring geometry, information is uniformly distributed by LOR angles if the image is unknown. This makes the choice of the order arbitrary. When it comes to PET systems of unconventional geometry, this becomes complicated as there is no standard sinogram for such systems. The Insert-Scanner and Insert-Insert LORs do not provide full sampling coverage in all angles, so grouping by LOR angle will break down the balance of information provided by each subset. So in our previous reconstruction for a half-ring insert [29], no ordered subsets are applied.

In the image reconstruction framework for PET under different arbitrary geometries, we implemented an ordered subset update by randomly grouping non-symmetric LORs into (Symmetry Encoded Detector Cluster) SEDC groups. While doing projecting, we use a sequence of non-overlapping subsets arbitrarily drawn from these SEDC groups [37]. The number of SEDC groups is much larger than the number of subsets, providing a natural way to distribute the computation load onto a parallel architecture. The random grouping and selection is to ensure a good load balancing because for such PET systems, coincidence counts may be heavily unevenly distributed across LORs.

However, when it comes to list-mode reconstruction with a dynamic geometry, all these previous methods will not hold because all of them require rebinning the list-mode events into histograms, eliminating all the benefits brought by list-mode reconstruction. So here I uses a time frame based OSEM approach, breaking the data set of entire time duration into subsets that each contains a segment time duration. To balance the computation on each subset, roughly equal time duration is used for each subset. When we segment the data set sequentially into equal time frames, the events are randomly distributed among all possible LORs. This brings the advantage that we can used the same sensitivity image with only applying a scaling factor according to the length of duration.

3.5 Application to Different Systems

To demonstrate the flexibility and wide application, we have applied this image reconstruction framework to a lot of systems, including simulated systems, an in-house developed PET system and a clinical PET scanner. This tool is a key to the study of novel PET systems described in the next 2 sections. Here, Table 3.2 shows the image reconstruction parameters for a few different systems that this image reconstruction framework has been applied to.

Table 3.2: Image reconstruction parameters for 3 different PET systems

System	Number of Crystals	Image Volume	Voxel Size
Plant PET	18176	$256 \times 256 \times 160$	$0.8 \times 0.8 \times 0.8$
Micro Insert	44800	$336 \times 336 \times 160$	$0.8 \times 0.8 \times 0.8$
Biograph 40	32448	$600 \times 600 \times 224$	$1.0 \times 1.0 \times 1.0$

We use the Plant PET and Micro Insert - Micro PET systems to demonstrate the ability to work on PET systems with unconventional but static geometry. The application to dynamic geometry will be presented in the next 2 chapters. By comparison with Siemens clinical

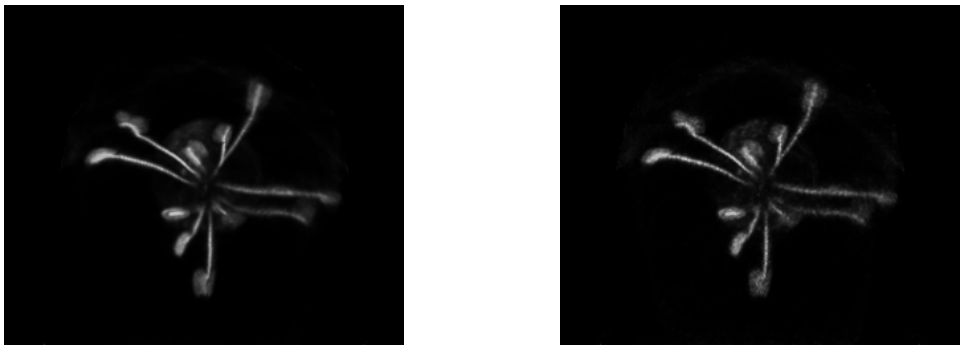

(a) (b)

Figure 3.6: One slice of the 3D maximum intensity projected reconstruction images at 15th iteration for a Venus flytrap using data acquire by plant PET system with (a) 14 million counts and (b) 1.6 million counts.

software, we show the performance of our image reconstruction and several drawbacks where improvements are needed.

3.5.1 Plant PET System

Plant PET system is an in-house developed dedicated PET system dedicated for plant imaging studies [60]. It is installed inside a climate controlled growth chamber to allow plant biologists study the biological response of plants given certain stimulation. The system consist of two half-rings. The larger half ring has 5376 crystals of $2.4 \times 2.4 \times 10$ mm^3 each while the small ring has 12800 crystals of $1.59 \times 1.59 \times 10$ mm^3 each.

Figure 3.6 shows side by side the Venus flytrap image reconstructed from the same data set but using different number of counts. The high counts image on the left side is obviously smoother than the low counts image on the right side. The reconstruction time it takes on a Geforce GTX 680 is 47 seconds and 5.5 seconds respectively, per iteration. By using the latest hardware and multiple GPUs together, the reconstruction time can further improve.

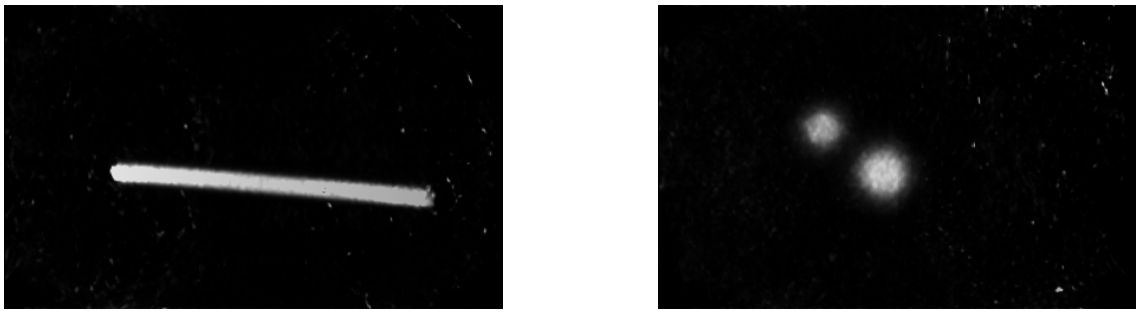

(a) (b)

Figure 3.7: One slice of the 3D maximum intensity projected reconstruction images at 10th iteration for a (a) line source and (b) two ^{68}Ge spherical bead sources imaged by the standalone insert system.

It is possible to reconstruct a low counts image within 10 seconds. This is helpful in dynamic imaging study, where the measured data is segmented into frames based on time stamps to study the activity concentration changing by time in the plant. One frame of data usually contains a small number of counts from a short period of scan. Fast image reconstruction could make it possible to get the image of last frame reconstructed before the data acquisition of current frame is finished.

3.5.2 Micro Insert - Micro PET System

Micro Insert - Micro PET is an in-house developed system that incorporates a high resolution full ring geometry insert into a small animal PET scanner. Currently we only investigated the standalone insert system without doing joint reconstruction with the scanner. The insert consists of 19200 crystals of $0.8 \times 0.8 \times 3$ mm^3 each arranged in a diameter of around 6 cm. Figure 3.7 shows maximum intensity projection of some preliminary reconstructed images by the standalone insert system.

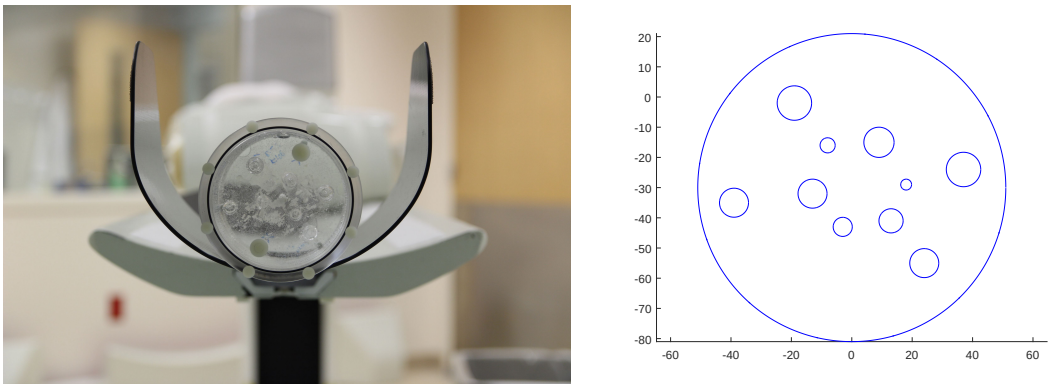

(a) (b)

Figure 3.8: (a) Experiment phantom imaged by Siemens Biograph 40® clinical PET-CT and (b) Illustration of the spherical tumors arrangement in the phantom.

3.5.3 Siemens Biograph 40 Clinical Scanner

Siemens Biograph 40® PET/CT is a commercial clinical scanner used for daily patient study at CCIR. The scanner has 192 block detector modules arranged in a 4 ring geometry with radius of 42.7 cm. Each block detector has 13×13 lutetium oxyorthosilicate LSO crystals of $4 \times 4 \times 20$ mm^3 pitch size, totaling 32448 for the entire scanner.

We performed a phantom study on the Siemens Biograph 40® clinical system. The phantom includes 10 spherical tumors with diameters shown in Figure 3.9. Initially, the background of the phantom is filled with activity concentration of 1.856μCi/cc and all spherical tumors have 4 times the activity concentration. We scanned the phantom for 600 seconds using the brain imaging protocol and reconstructed using different parameter combinations.

All images in Figure 3.9 are reconstructed using the entire 600 seconds data of 54805209 prompt events. All of them are reconstructed into a $336 \times 336 \times 56$ image volume of $1.0182 \times 1.0182 \times 4$ mm^3 voxel size. A Gaussian filter with FWHM of 2 mm is applied in the post processing step. Clearly we see that in Figure 3.9a filtered back projection

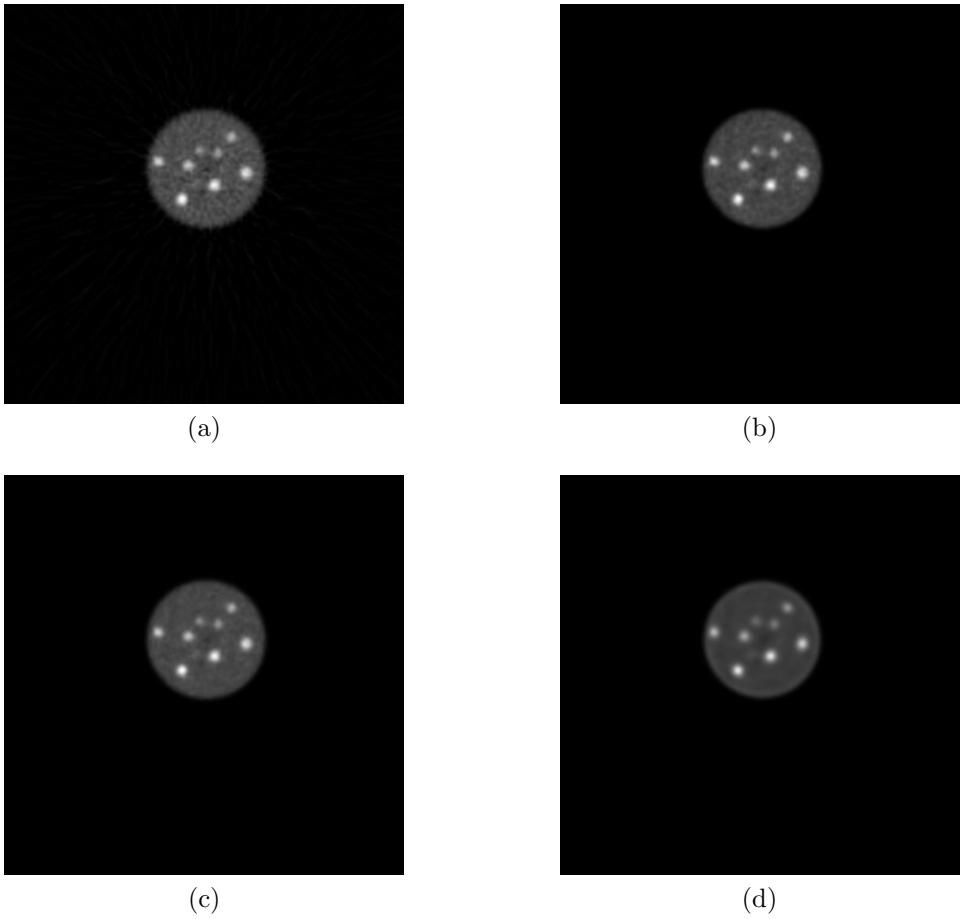

(a) (b)

(c) (d)

Figure 3.9: Reconstructed images of the phantom via standard clinical software using (a) filtered back projection (b) OSEM method of 2 iterations and 24 subsets (c) OSEM method of 8 iterations and 4 subsets (d) OSEM method of 8 iterations and 4 subsets with PSF TrueX algorithm.

method introduced streak artifacts and small tumors are less visible. The two OSEM methods are most commonly used because they achieve a balance between image quality and reconstruction speed for 3D PET. Since the clinical software has a limitation on the number of iterations and the number of subsets that can be used, we reconstructed in Figure 3.9b the default configuration of fewest iterations and most subsets, while Figure 3.9c shows the result of using the most iterations and fewest subsets. The second one provides slightly better background uniformity and less noise, at a cost of increased reconstruction time of 310 seconds compared to 210 seconds. The last one is reconstructed using Siemens True X algorithm, which is a resolution recovery algorithm incorporating experimentally measured point spread function into the system matrix. There are many studies claim that algorithm provides better quantification for small tumors. However in our case, this method introduced artifacts such as bright edges. As a result, I'll use the OSEM with 8 iterations and 4 subsets to compare with the GPU-based list-mode reconstruction I developed.

Before going through the clinical software, the same phantom was scanned through a command-line interface without using any preset imaging protocols, in order to get the 64-bit format list mode coincidence data that contains time information for all events. To make a fair comparison, we only use roughly the same number of prompts for image reconstruction. The GPU reconstruction runs on a desktop workstation that has 4 Nvidia Geforce Titan X (Maxwell generation) without using peer-to-peer memory link. We measure the performance through the time stamp of images written to the hard drive. For 55 million list-mode events, it takes 115 seconds per iteration for the non-penalized version (GPU ML) while 128 seconds per iteration for the penalized version (GPU PL-ML) to reconstruct a $600 \times 600 \times 224$ volume. Images in Figure 3.10 are shown at the 30th iteration and at the same window level. The images reconstructed by Siemens software are in integer format by default. In order to make a quantitative comparison, it is normalized through dividing the entire image voxels by

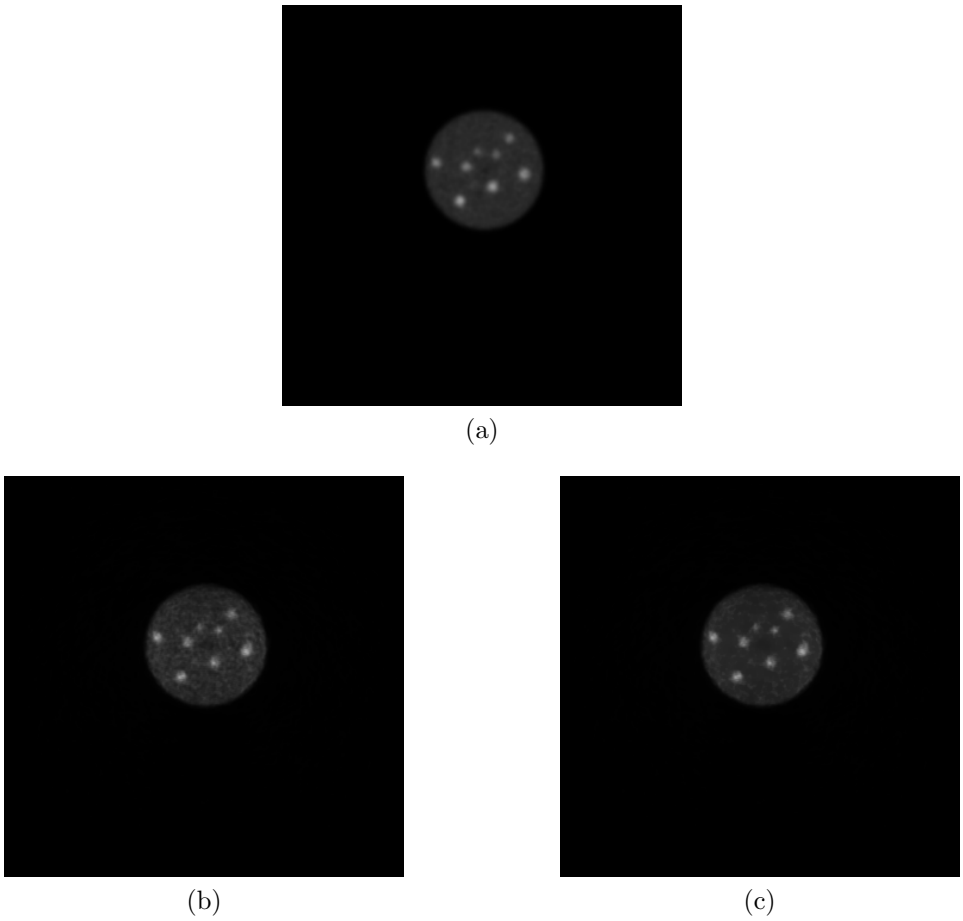

(a) (b) (c)

Figure 3.10: Experiment phantom reconstructed image by (a) Siemens Biograph 40® clinical PET-CT and (b) GPU list mode reconstruction with no penalty and (c) GPU list mode reconstruction with smoothness penalty. Images are reconstructed using roughly the same number of coincidence counts and shown at the same window level.

the average value measured in a selected background region. Profiles are drawn in a 2-pixel wide region.

Although this is not a rigorous comparison between our GPU list-mode reconstruction framework and the Siemens clinical software, it does show that these two reconstructions present similar recovery for these tumor sizes and contrast level. The Siemens image has applied a Gaussian post-filter of 2 mm FWHM. Without knowing its implementation details, it is

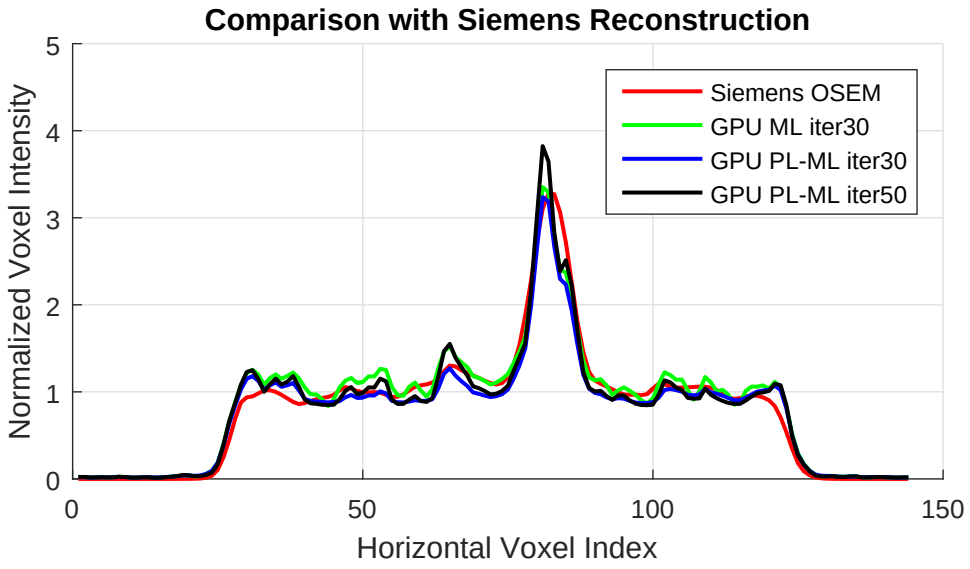

Figure 3.11: Plot of profiles for the Siemens Biograph 40® and GPU reconstructed images.

difficult and not meaningful to blur our images by post filtering to match the Siemens image. There is also a fundamental difference between these two image reconstructions. The Siemens reconstruction is essentially a 3D reconstruction re-binned into 2D slices by axial compression while our GPU list-mode reconstruction is by its nature fully 3D without any data compression.

These differences make it difficult to evaluate the computational speed by directly comparing the time per iteration. The number of image voxels used in our GPU reconstruction is 12.8 times of that of Siemens. Considering this factor, our image reconstruction speed could increase to roughly 10 seconds per iteration if larger voxels and smaller FOV are used. Using 3D data re-binned into 2D sinograms and exploring 16-fold symmetry in ring geometry also helps greatly reduce the computational load.

We note that the tumors in our reconstructed images are not as round as those shown in the Siemens image. The main peak in the plotted profile also suggests this difference between the two reconstruction results. The edges of the phantom in our reconstruction have a tendency to light up while the Siemens image preserves nice smooth edges. These differences come from a combination of several physical process that are not corrected in our reconstruction. First, our attenuation correction is based on calculated values assuming the entire phantom volume is filled with water. However the phantom has plastic walls, internal structures and glass sphere walls that need to be corrected based on a CT scan. Second, our image reconstruction does not compensate for the different efficiency of LSO crystals, which creates artifacts in the reconstructed images. Without this correction, regions where it should be uniform may exhibit a certain pattern, normally in ring or arc shape. Last, the absence of scatter correction also adds to these artifacts.

It is difficult to compare the noise property because the Siemens reconstruction uses a very large voxel in the axial direction, in addition to the post filtering. The addition of artifacts due to lack of complete data correction also amplifies the noise for our reconstruction. We do observe that the noise is largely reduced when comparing the GPU ML and GPU PL-ML results. The performance should be further improved if all the proper data correction is addressed in future development.

Quantitative accuracy of PET imaging heavily depends on the completeness and correctness of modeling all physical processes happening during PET data acquisition. It is out of the scope of my work to develop an image reconstruction software that performs better than clinical software. Since our image reconstruction serves as an important tool to perform all kinds of PET studies on the in-house developed hardware, most of which are beyond the capability of standard commercial or open source software. It is important to perform some kind of validation before applying to scientific study. The comparison here is mainly to establish a baseline of the overall function and performance when our reconstruction is applied on standard clinical PET, besides any drawback mentioned above.

3.6 Performance Comparison with Previous Work

We compare this list-mode GPU-based image reconstruction framework with the previously developed CPU-based reconstruction [37] to show the different aspects they focus on. The GPU reconstruction is not simply a CPU transported version. They are both designed under the concept that they can be easily adapted to PET systems with arbitrary geometry. However, besides the different computing architectures they are running on, there are major

differences in the choice of projection kernel and the way of organizing data. These changes are specifically made to suit the architecture and our application needs.

A major advantage of the GPU reconstruction is the speed. It's difficult to compare the speed between a list-mode method and a histogram-mode method. The speed of list-mode method is proportional to the number of list-mode events, while the speed of histogram-method method is a fixed number depending on the size of the image FOV and the number of LORs. If we compare the situation in a typical clinical PET scan, the list-mode data acquired from one bed position is on the same order of magnitude of the number of possible LORs. The list-mode method does not have a clear advantage over the histogram-mode method, especially when symmetry is used to optimize the projection. However, this comparison is based on the fact that the GPU reconstruction uses on-the-fly projection, while the CPU reconstruction uses a pre-computed projection matrix. The system matrix itself takes more than 1 hour to compute. For PET systems with static geometry, either pre-computation or on-the-fly computation will work. While in situations where the geometry changes during the scan, the projection matrix has to be re-computed when any geometry change happens. If we consider the time it takes to generate the projection matrix, the GPU image reconstruction will have a significant advantage over the CPU version.

We tried to establish a fair comparison with the same voxels sizes and FOV dimensions. It turns out the pre-computed system matrix required by the previously developed CPU-based image reconstruction exceeds the limit of our storage space on the supercomputer. Instead we scale down the reconstruction parameter to $2 \times 2 \times 4$ mm^3 voxel size and $430 \times 430 \times 56$ image FOV. This scaled-down version does not represent the best image quality that can be achieved by this CPU image reconstruction. Table 3.3 does not serve as a rigorous comparison in terms of speed since they are fundamentally different in many aspects. But

Table 3.3: Comparison between GPU and CPU image reconstruction for clinical scanner

	GPU recon	**CPU recon**
FOV	$600 \times 600 \times 224$	$430 \times 430 \times 56$
LUT size	N/A	400 GB
Voxel size	$1 \times 1 \times 1$ mm^3	$2 \times 2 \times 4$ mm^3
Projection Kernel	Gaussian-Distance	Siddon's ray tracing (single)
Penalty Implementation	Convex Decoupled	One-Step-Late
OSEM strategy	Time-segmented	Random selection
Time/iteration	24 sec	5040 sec
Data Format	List mode	Histogram mode
Data Size	8778092 events	Histogram mode
Hardware	4 Titan X	Intel i7-4770k 4 cores
Geometry Flexibility	Dynamic	Static

the improvement in terms of reconstruction time per iteration on a practical dataset does illustrate the benefits of implementing a list-mode reconstruction on GPU. Images shown in Figure 3.12a are interpolated to $1 \times 1 \times 4$ mm^3 voxel size bilinearly to give the same display size.

3.7 Conclusion and Summary

In this part of work, I developed a list-mode image reconstruction framework running on the GPU computing platform. Compared to previous development, this reconstruction is capable of modeling actively controlled geometry in an efficient implementation on the GPU platform. It maintains the capability of working with flexible geometry PET systems while providing additional benefits by organizing the data in list mode. It is currently used in routine experiments in our plant PET imaging lab because of its efficiency, especially for applications with relatively low statistics when reconstructing dynamic images segmented by time frames. By comparison with Siemens clinical reconstruction and our previous work,

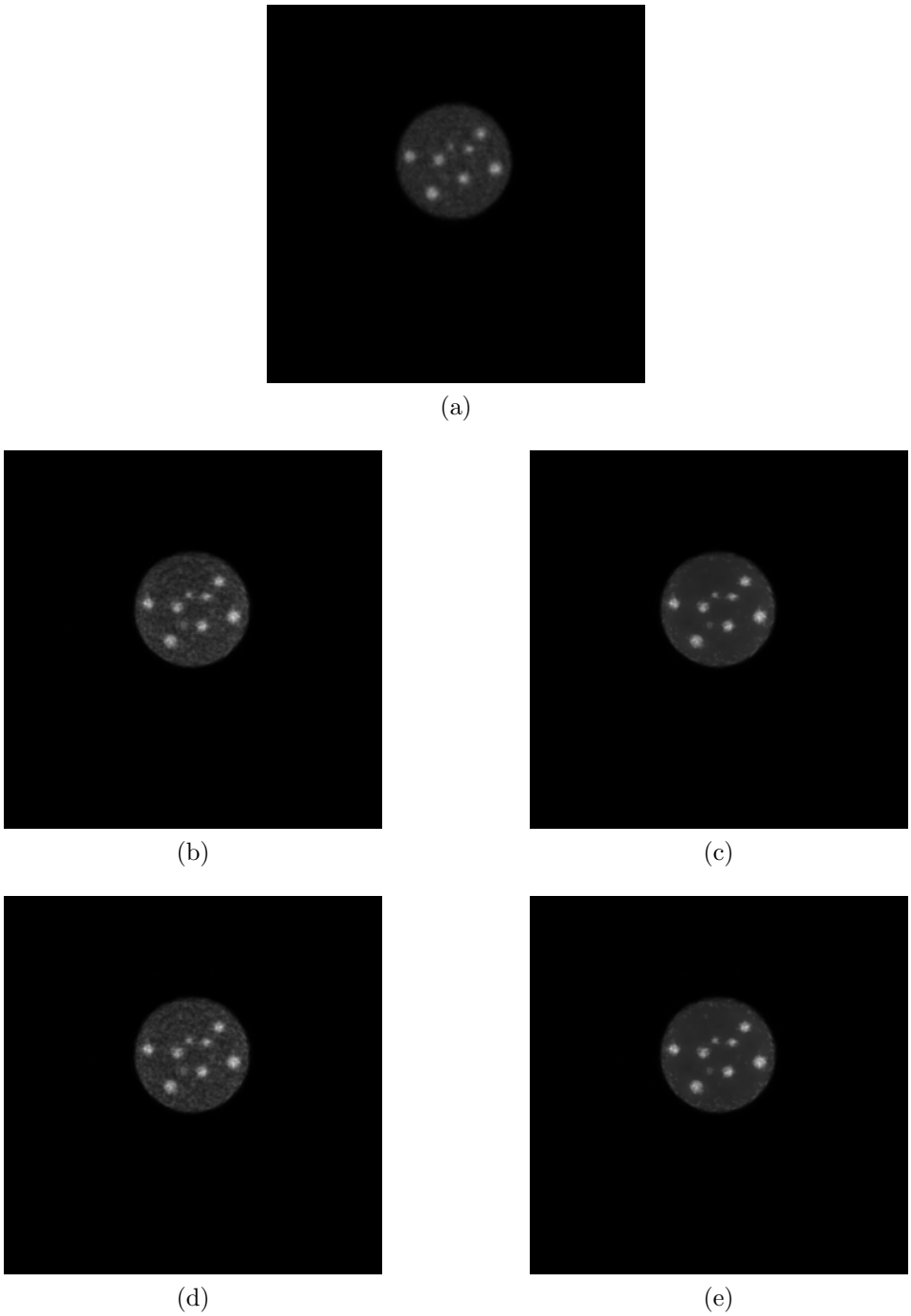

Figure 3.12: GATE simulated phantom reconstructed image by (a) previously developed CPU based reconstruction without penalty and (b) GPU list mode reconstruction without penalty; (c) GPU list mode reconstruction with penalty; (d) GPU list mode reconstruction with TOF information (TOF FWHM = 528 ps) without penalty; (e) GPU list mode reconstruction with TOF information with penalty.

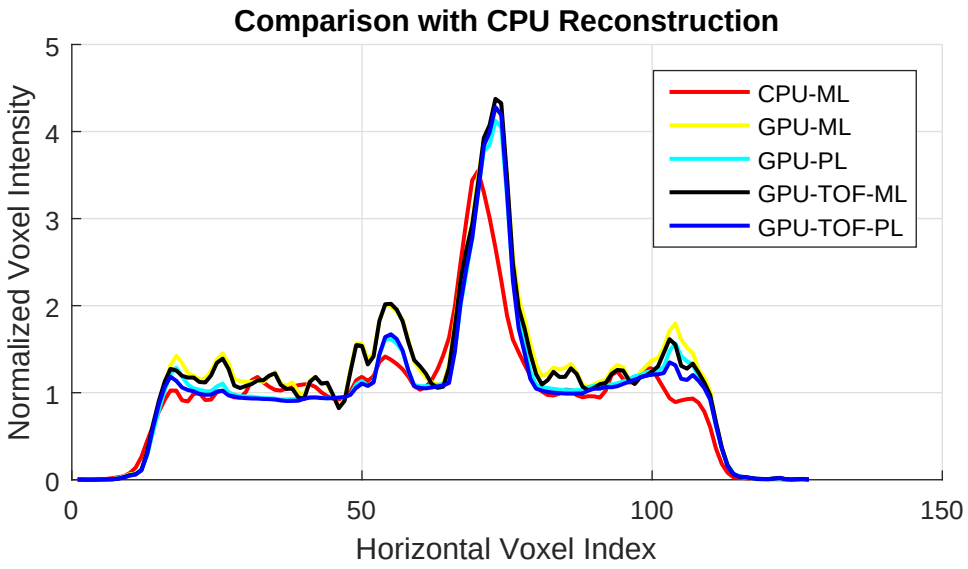

Figure 3.13: Plot of profiles of reconstructed images by CPU and GPU with different parameters.

this reconstruction provides similar image quality in a much shorter time. This work serves as an essential tool to carry out the Point-Of-Care (POC) PET and second generation robotic Virtual Pinhole PET (VP-PET). Performance of these two proposed systems will be studied using this image reconstruction tool. Other features such as incorporating with KUKA robot, reconstruction of TOF data will be presented in the following chapters.

Chapter 4

Second Generation Robot Controlled Virtual Pinhole PET

We are developing a second-generation robot controlled VP-PET insert that can enhance the image resolution and lesion detectability of a whole-body PET/CT scanner for an arbitrary organ-of-interest. A robotic system is used to place a high resolution flat panel PET detector as an insert device in the scanner field-of-view (FOV). A procedure has been developed to calibrate the robotic controlled insert to move in the scanner coordinate system at a precision within 0.5 mm repeatability in a practical clinical setting. List-mode Maximum a Posterior (MAP) image reconstruction running on a multi-GPU platform is used to jointly reconstruct the Scanner-Scanner (SS) and Insert-Scanner (IS) coincidence events acquired from arbitrary insert locations. In order to validate the functionality of the system and image reconstruction, as well as to evaluate its potential improvement in small lesion detectability, we performed Monte Carlo simulation and real experiment under a realistic clinical condition. Monte Carlo results show expected improvement in the resolution and detectability of small lesions. Experimental results validated the overall functionality of the system and work flow

but also indicate the requirement for developing a more accurate and robust robot positioning method.

4.1 Introduction and Background

Positron Emission Tomography (PET) provides in vivo measurement of imaging ligands that are labeled with positron emitting radionuclide. A typical whole-body scan using fludeoxyglucose (18F) (18F-FDG) reflects the glucose metabolism in the patient body, with increased activity shown in cancer cells. Commercial clinical PET scanners are designed for whole body imaging application such as cancer staging. Image resolution and sensitivity are important in such application since the ability to identify small lymph nodes and metastasized tumors affects the diagnostic accuracy. Conventional clinical PET scanners normally have detectors arranged in a ring geometry which is large enough to accommodate most patients' body. As we described in Chapter1, photon non-collinearity affects the overall image resolution. When the scanner gantry diameter is large enough, it becomes a limiting factor of resolution since the small deviation in the opposing angle of the back-to-back gamma photons results in more significant error after traveling a long distance before they hit the detector. This kind of resolution degradation cannot be overcome by simply upgrading all the detectors, when the photon non-collinearity effect contributes to the overall resolution at similar level or more than the intrinsic resolution of detectors. As PET is a photon counting system, sensitivity is another significant factor that affects the detectability of tumors or lymph nodes in smaller sizes. Systems with higher sensitivity require less scan time to achieve the same image quality as systems with lower sensitivity.

Effective solution to the resolution and sensitivity of whole body PET requires a redesign of the detector geometry. Organ-specific PET systems answer this question with detectors arranged in an organ-specific geometry. For example, commercial positron emission mammography (PEM) systems provide better detectability of small breast tumors compared to whole body PET. Many groups have investigated different PET systems specifically designed for head, breast and prostate. While these systems did address the resolution issue with whole body PET, their advantages are limited to the specific organ and application, and they cannot be used when whole body imaging is required.

To bring the benefits of high resolution organ specific PET to where whole body imaging is needed, many groups including our group have investigated various approaches under the similar principle: placing high resolution detectors closer to the Region-Of-Interest (ROI). We have demonstrated virtual-pinhole geometry in the past that we can increase the image resolution and lesion contrast by inserting a high-resolution PET detector device into a whole-body scanner. Other groups have shown different forms of high resolution PET detectors being used as a zoom-in device [66] or a silicon probe [9]. Bringing a high resolution detector closer to the ROI not only reduces the photon non-collinearity effect but also improves regional sensitivity.

Our first generation of VP PET has a half-ring geometry which consists of 28 block detectors with crystal size of $2 \times 2 \times 5$ mm^3. It has a diameter of 24.6 cm which is supposed to accommodate the patient head as this insert is specifically designed for head and neck cancer. Having a half ring geometry aligned (in in-plane and axial directions) with the scanner brings several benefits. Besides Insert-Scanner coincidence events, it also generates the Insert-Insert coincidence events which provide the most information and highest resolution. Aspects of the symmetry commonly used in whole body PET image reconstruction can still be used

for Insert-Scanner and Insert-Insert coincidence events [29], which results in reduction of reconstruction time.

In real applications, one difficulty that we have faced when using this half ring shaped insert was to accurately place the insert at the required position in the scanner FOV. As the insert is mounted on a three-dimensional linear translation stage, it is time consuming to calibrate this system precisely in a practical clinical environment. We used to spend more than 3 hours to run through the calibration procedure before actually scanning the patient, leaving the whole system inconvenient to use. The half ring insert itself also creates limitations when scanning patients of different body shape, as it must be aligned with the center axis of the scanner. Depending on the shape of the head and neck of a patient and the tumor location, it might not be possible to place the ROI in the center of the insert FOV. This will degrade the image quality because the insert system also has highest resolution and sensitivity in the axial center position.

As a partial solution of this problem, we developed a flexible image reconstruction framework which allows us to lower the insert to the bottom of the scanner gantry. The head and neck of some patients who do not fit into the original setting can be simply placed above the lowered insert. This solution came at a cost of losing some Insert-Inset data as well as increasing the distance between the insert and tumor in Insert-Scanner data, while still providing the most valuable information in terms of resolution. Another side effect is that this solution breaks down some symmetry properties and results in increased size of system matrix and running time for image reconstruction.

With this prior knowledge in mind, one goal of our second-generation VP-PET is that it has to be convenient to use in a clinical environment. It should provide improved flexibility so that the insert position can be adaptively adjusted according to the patient type and

organ-of-interest. We previously used a MicroScribe® device (referred as microscribe in this chapter) to measure the position of a small detector probe. In medical applications, optical tracking devices have been used in other Single Photon Emission Computed Tomography (SPECT) and PET devices that incorporate free moving detectors. Optical tracking is a contactless approach that achieves best flexibility and occupies the least amount of space. Compare to linear translation stages, optically tracked detectors can be moved in all 6 Degree Of Freedom (DOF) freely with least limitation caused by mechanical structure. This is a significant benefit over mechanical tracking method when designing a portable system for intraoperative application, where doctors maneuver the detector by hand to image any organ-of-interest from different angles. However, using an optical tracking device still requires additional positioning mechanism to hold the detector in place. We propose to use a commercial robot with a force torque (F/T) sensor to actively control our high resolution panel detector with precision and repeatability. With the aid of a 6-DOF robot, our detector panel can be placed near a ROI at a desired direction and distance, simultaneously when the patient undergoes a standard whole body PET scan. Depending on the imaging task and protocol, the placement of detector panel can be pre-programmed into the robot, or manually controlled on-the-fly by the operator. In some cases, enabled by the F/T sensor, we can guide the detector to a desired position and orientation by hand and lock the robot.

4.2 Integration of Robotic Controlled Flat Panel Insert with Clinical Scanner

The robot we used for this study is KUKA AGILUS® KR10 R1100 sixx. The six axes small robot provides 6-DOF control of the device mounted on it. It is capable of handling a 10 kg

payload within a range of 1.1 meters. Our high resolution PET detector has a total weight of less than 2 kg. Considering the F/T sensor with some connection accessories and the extended holder of the detector, the entire package is well within the capability of this robot. The robot itself can achieve repeatability of ± 0.03 mm which meets the requirements of our application.

In this section, we use "scanner base" to describe the coordinate system of the clinical scanner, which is registered as the base in the robot controller. We use "alignment tool", "insert tool" to describe the coordinate system of the corresponding object mounted on the robot, which is registered as different tools in the robot controller.

4.2.1 High Resolution Flat Panel PET Insert

The flat panel detector comprise 32 high-resolution detectors arranged in 8×4 array, see Figure 4.1a. Each array contains a 4×4 Silicon Photomultiplier (SiPM) array and 16×16 lutetium-yttrium oxyorthosilicate (LYSO) crystals with each crystal measuring $0.92 \times 0.92 \times 3.00$ mm^3. With 1 mm gap between each block detector, the flat panel detector ends up having a detection area of 141.4×70.2 mm^2. The insert is housed in a rectangular case made with carbon fiber. The light-weight material maintains a steady structure as well as minimizes the attenuation that affects the photon detection. The panel is connected to a carbon fiber tube of 30 cm in length.

The detectors in each array are coupled to a resister network as the output signals are reduced to 4 channels. These signals are being pre-amplified before sent into Siemens Detector Electrronic Assembly (DEA) modules of the Biograph 40 PET scanner. In order to read out

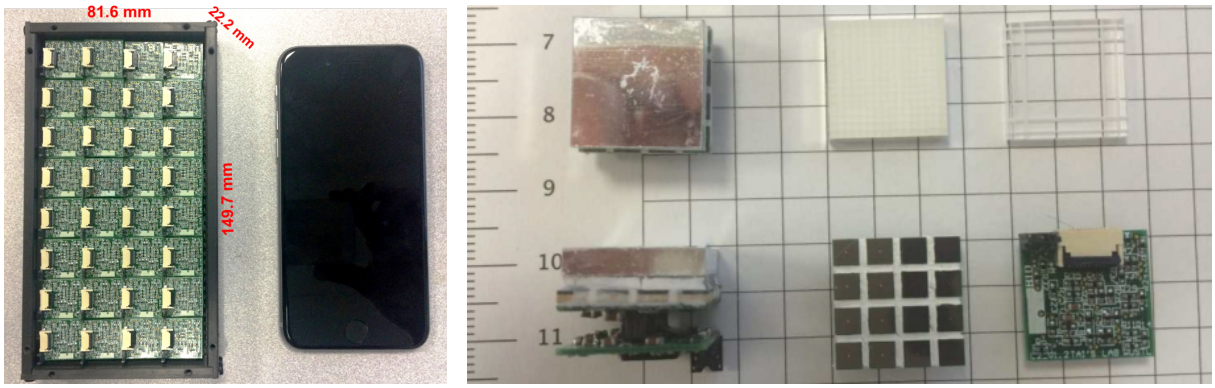

(a) (b)

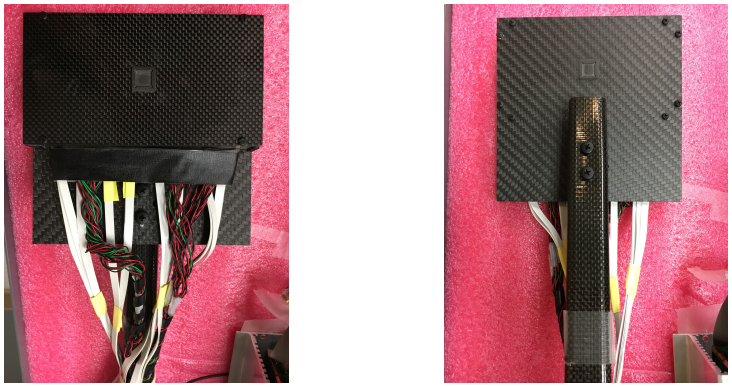

(c) (d)

Figure 4.1: (a) Detector blocks arranged in 8×4 array inside the case, compared with a cell phone with 5.5 inch screen. (b) Internal view of block detectors and crystals. (c) Front view and (d) back view of the panel and tube holder assembly.

the signals by this insert, customized firmware and software were developed to support the additional detector signals without compromising the scanner functions [61].

4.2.2 Integration of Insert and Robotic Arm

The carbon fiber tube is first connected to the robot via a quick release connector, then a Force-Torque (F/T) sensor and finally to the flange of the robot. Our flat panel detector is treated as a tool of the robot. To establish the tool coordinate system, we use direct measurement method to calculate the transform matrix for the robot. We use the microscribe as a Coordinate Measurement Machine (CMM) to measure a few characteristic points on the flat panel detector assembly and the adapter plate, which is the mating surface to the robot flange.

4.2.3 Establishing the Coordinate System of Whole Body Scanner

Our robot is mounted on a cart to allow us move the robot in and out of the clinical scanner room, and to put the robot at a workable position. While in use, cart locks its wheels to prevent unexpected movement which will break the established coordinate system. This section describes the procedure to integrate the whole system with the clinical scanner. However, the cart design and locking mechanism may not satisfy the need for a real patient scan. Future plans for fixing the robot are still under evaluation.

Our goal is to register the PET scanner coordinate system into the coordinate system of robot controller, so that the robot can perform movement scanner base coordinate system. The most common way to establish a base in the KUKA robot is to touch the origin, a point

along the X-axis and a point in the XY-plane. However, in our case, it's not possible to find the origin and the XY-plane. So we designed our registration process using a customized tool piece and three alignment pins on the back metal panel of the clinical scanner.

The alignment tool piece is a machined rotatory counterpart of the alignment pin (shown in Figure 4.2a) with slight tolerance to allow the F/T sensor to find the right path. After the robot cart is set at a fixed position, the alignment tool is moved to the roughly estimated positions of the three alignment pins in the sequence. At each position, the F/T sensor is engaged with searching direction pointing in the tool positive z-axis (the alignment hole axial direction, pointing front towards the scanner gantry). The F/T sensor is set to stop if the following conditions are met: 1. The Z-force reaches 5 N and 2. The force on the other two axis are within 0 ± 0.2 N and 3. The torque along all three axes are within 0 ± 0.1 N·m. While searching, the second and third conditions force the robot to correct for its tool position and direction frequently to maintain near zero force and torque. Oscillations are prevented by introducing a larger opening of the alignment tool and small tolerance of its inside. The F/T sensor will finally stop when the tool is pushed hard on the metal back panel surface of the scanner, as shown in Figure 4.2b. The current coordinate of tool center point (TCP) is recorded for the following computations.

4.2.4 PET Data Based Coordinate System Calibration

We evaluated the positioning accuracy of the robot by (1) mounting a Na-22 point-source to the flat-panel and stepping the source across known scanner lines-of-response (LOR); (2) comparing centroids of the coincidence count profiles to their theoretical values.

(a) (b)

Figure 4.2: Customized alignment tool guided by force-torque sensor automatically searching for best contact with the metal back panel of the scanner (a) during the searching process and (b) firm contact is made and TCP is recorded for coordinate system calculation

We developed a data-based method to precisely calibrate the scanner base coordinate system established by the procedures above, to eliminate the difference between this coordinate system and the true coordinate system defined by the PET crystals. After this calibration process, these two coordinate system should coincide within an acceptable error margin and the established coordinate system will be used for image reconstruction.

The true coordinate system of the robot is determined by the crystal module of the scanner. In an ideal situation, the previous step registers this coordinate system to be the "base" in the robot controller. However, this method is purely based on mechanical structure and even with zero measurement error we can register the coordinate determined by the mechanical parts to the robot. In reality, there is system error between the true coordinate system and the mechanical coordinate system. Possible sources of error include:

1. The CAD drawing may not reflect the most accurate design specifications.

2. The tolerance of individual components adds up and makes the whole structure have larger error than desired.

3. The housing of a block detector is not exactly concentric with the internal crystals.

4. Misalignment could happen during the manual installation of detectors.

These issues are less severe when dealing with whole body PET that uses $4mm$ crystals. However, since our flat panel has $1mm$ crystals, we need to have a position precision well below the crystal dimensions. Our approach was similar to the one we used for the first generation of half-ring insert [29], but capable of correcting all 6 DOF instead of only the 3 translation dimensions.

4.3 Image Reconstruction for Second Generation Robot Controlled VP-PET

4.3.1 Geometry Modeling

The resolution in terms of FWHM of Scanner-Scanner and Insert-Scanner TOR R_{det} can be roughly estimated by (4.3), as described in [57].

$$w_b = w_1 + \frac{w_2 - w_1}{D} \cdot x \tag{4.1}$$

$$w_p = \frac{|(D - x) \cdot w_1 - x \cdot w_2|}{D} \tag{4.2}$$

$$R_{det} = \frac{w_b + w_p}{2} \tag{4.3}$$

These equations calculate the detector TOR resolution by FWHM of a pair of front facing detectors of size w_1 and w_2 separated at a distance D. The whole system resolution is roughly estimated as a combination of detector TOR resolution, non-collinearity and blurring from the source emission process.

Figure 4.3 shows the FWHM of the TOR formed by a front facing insert-scanner crystal pair of 1 mm and 4 mm separated at a distance of 647.6 mm, as a function of distance from the insert crystal. Due to the large difference in crystal size, the best resolution 0.85 mm is not observed at the middle point, but much closer to the insert crystal. During the scanning process, our panel is placed in a way that the best resolution falls onto our region of interest, in order to get the maximum benefits from our insert detector.

An important thing to note is that this only considers pure geometric effects for a pair of front facing crystals. In reality, photons coming in an oblique angle will not only hit the front face of the crystal, but also the side. This will increase the effective crystal cross section thus degrading the resolution. Besides, almost all PET scanners use block detectors, which introduces the block effect. The block effect is a combination of different physical processes [59] that makes it uncertain to determine the interaction position of the gamma photon in a block detector. It degrades the actual resolution of the TOR and should be studied by experiment.

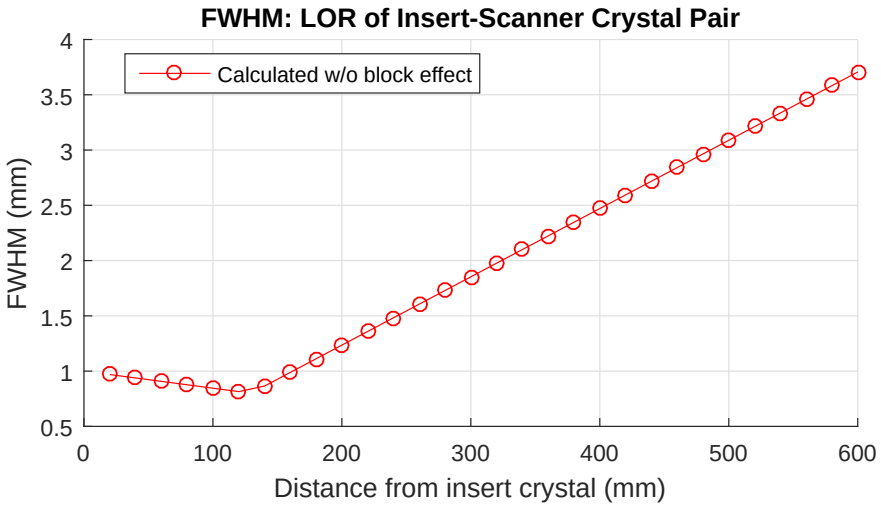

Figure 4.3: FWHM of the tube-of-response from the front facing insert-scanner crystal pair

4.3.2 Incorporating Robotic Information into Reconstruction

During a robotic VP-PET scan, the robot will move the detector panel to a desired position and this position information is needed when doing image reconstruction. It is desired to make our image reconstruction compatible with what our robot provides. The robot position information is provide in KUKA's 6-DOF representation, using 6 parameters $[X\ Y\ Z\ A\ B\ C]$ to localize a rigid body in space. The $[X\ Y\ Z]$ is the tool center point translation while the $[A\ B\ C]$ is the rotation in Tait-Bryan angles following the yaw, pitch and roll convention. This convention is also known as the $Z \Rightarrow Y' \Rightarrow X''$ moving frame. By exploring the equivalency between moving frame and static frame from (4.4) we can easily calculate the point rotation matrix from given $[A\ B\ C]$ angles.

$$Z(A) \Rightarrow Y'(B) \Rightarrow X''(C) \qquad \equiv \qquad X(C) \Rightarrow Y(B) \Rightarrow Z(A) \tag{4.4}$$

The translation vector and rotation matrix is then used to transform the crystal in the geometry definition of insert crystals to where they should be. If we apply a global correction, which is required if we want to correct any systematic positioning error after data acquisition is finished, the geometry definition of all insert crystals will be correct at the beginning of the reconstruction.

4.3.3 Data Correction

4.3.3.1 Attenuation Correction

Attenuation correction is performed in a standard μ-map based method. The μ-map is generated from a CT scan of the object and then mapped to equivalent μ values at 511 KeV energy level. Since acquiring the CT image and the conversion to 511 KeV μ-map is a separate issue and is outside of the scope of this thesis, I did not use the real CT generated μ-map for studies performed here. Instead, I directly used the calculated μ-map for Monte Carlo simulation when reconstructing the simulation data. For the phantom experiments, since the phantom is a regular cylinder of known dimension and mostly filled with Fluorine-18 water solution, I created an artificial μ-map using attenuation values of water. The shape of attenuation media are created from images reconstructed without attenuation correction. Note that the cylinder phantom has plastic walls of thickness ranging from 2 mm to 5 mm. There is also an internal plastic supporting structure that holds the spherical tumors in place. The spherical tumors are made of glass and have different wall thickness. All these factors are not taken into account while creating the μ-map thus this method will introduce some discrepancy between the calculated attenuation correction values and the truth. These factors cause some artifacts observed in the reconstructed images shown later.

4.3.3.2 Randoms Correction

In a Monte Carlo study, we use true coincidence events without any randoms correction. However, randoms correction can be done in both simulation and experiments. In GATE simulation, we sort singles events by matching the event ID generated for every radioactive

decay event, or by finding the times of arrival that fall into a defined coincidence window. While sorting the events by coincidence window, we still record the event ID of the two singles detection and determine whether this is a true coincidence or a random coincidence.

4.3.3.3 Normalization and Time Weighting

We refer to normalization the correction of varying detection efficiency of LORs. In theory, normalization corrects for any physical effects which are not modeled by the system response function (system matrix). These effects include: crystal efficiency, block effect, inter-block scattering, oblique angle efficiency, length of LOR and more. For our study, the most important factor is crystal efficiency. This is because the Gaussian-TOR model used for this GPU-based list mode reconstruction only approximates the free space solid angle coverage by the LOR, for voxels within the LOR. It provides relative detection efficiency of the voxels in that LOR. Detection efficiency across different LORs are not comparable, especially for systems with scintillation crystal of different sizes. A major component that this system matrix does not model is the photon-crystal interaction path, where multiple types of interaction may happen. Our scanner and insert have the same types of LSO crystals but with big differences in thickness, which results in different detection efficiencies for Scanner-Scanner and Insert-Scanner LORs.

To account for the difference in the detection efficiency by different LORs, a different weighting factor is applied to the corresponding part of the system matrix. Without considering randoms and scatters correction, these coefficients end up as the weighting factors for the sensitivity image of Scanner-Scanner and Insert-Scanner system matrices.

$$H_{0j} = c_{ss} H_{0j}^{ss} + c_{is} H_{0j}^{is}, \tag{4.5}$$

where c_{ss} and c_{is} are the coefficient for SS and IS and they are obtained by

$$c_{ss} = \frac{N_{ss}}{\sum_j H_{0j}^{ss} E_j} \tag{4.6}$$

and

$$c_{is} = \frac{N_{is}}{\sum_j H_{0j}^{is} E_j}, \tag{4.7}$$

where N_{ss} and N_{is} are the total numbers of the corresponding types of coincidence counts acquired from a known activity distribution E_j, which is normally referred as the normalization phantom. This approach is used by other groups investigating similar kinds of insert to improve image resolution [9]. It is also the first component of the component-based normalization approach we used previously for our half ring insert. These equations are derived by assuming the individual crystal efficiencies are all the same and then solving the likelihood objective function with known activity distribution. The results of weighting coefficient should be independent of the choice of normalization phantom. Since we are only estimating a single parameter from a large number of counts, the size of the phantom and the scanning time do not need to be large. However, if the same normalization data is going to be used for more components, such as individual crystal efficiency, the phantom needs to cover enough LORs and the data needs to have enough counts to avoid over fitting and to reduce noise.

4.4 Methods

The focus of this study is to test the hypothesis whether this second generation robot controlled VP-PET could improve the detectability of small tumors or not. According to our previous experience, VP-PET will improve resolution and contrast recovery, compared to a pure whole body scanner. While these capabilities largely depend on the counting statistics of PET, a purpose of this study is to identify a borderline case that distinguishes this VP-PET from whole body PET in a practical situation. Choice of data acquisition time and contrast level will significantly affect the final detectability results. In clinical use, these parameters change with different imaging task/protocols and the radioactive tracer being used. Without limiting our study to a specific imaging protocol, we consider a typical F18-FDG whole body scan that takes 200 seconds (one bed position) with a tumor-to-background contrast ratio of 4:1 and use this condition for both Monte Carlo simulation and physical experiment study.

4.4.1 Monte Carlo Simulation using GATE

Monte Carlo simulations are performed using the GATE v7.2 package. In GATE simulation, a coincidence processing module takes the singles stream from one system and finds the coincidence events within this stream. This works perfectly with any simulation that involves only one system. However, it's difficult to construct the insert and the scanner in the same system in GATE. So we record the singles data list form both systems and find the coincidence by using our own coincidence processing tool. This tool can find either true coincidence events or regular prompt events using a defined coincidence window. It finds

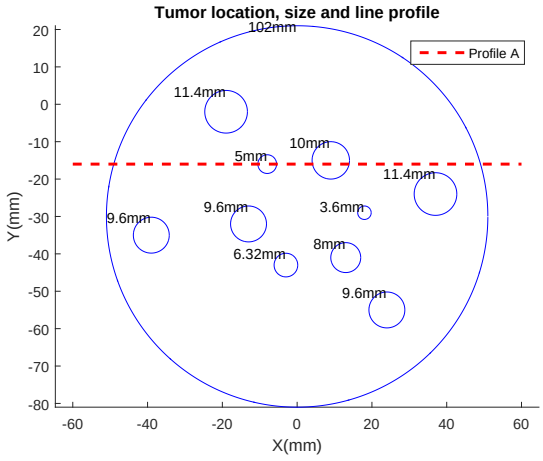

Figure 4.4: Cylindrical phantom with spherical tumors of different sizes simulated.

coincidence events across both singles data list, as well as within each of them. In this study, we use a coincidence window of 4.5 ns to identify all types of coincidence events.

A cylindrical phantom is simulated in GATE with tumor sizes and relative position in the FOV as shown in Figure 4.4 and Figure 4.5. This phantom follows the same pattern as the experimental phantom described in the next section. In order to save computation time, the height of the phantom is reduced to 3 cm, while the diameter of the cylinder is kept at 10.2 cm. Water is used as the attenuation material and no plastic component is simulated. The activity concentration of the background is 5284 Bq/cc, equivalent to the typical activity level of injecting 10 mCi radioactive tracer into a 70 kg patient body, assuming body density is the same as water. The tumors have higher activity concentration equal to 4 times that of the background, making it a 4:1 contrast ratio. The phantom is designed that some small tumors that will be hardly detected by a whole body scanner alone, under a typical 200 seconds acquisition time.

The whole body scanner configuration shown in Figure 4.5b follows the same geometry of Siemens Biograph 40® clinical scanner. The phantom is placed down towards the bottom

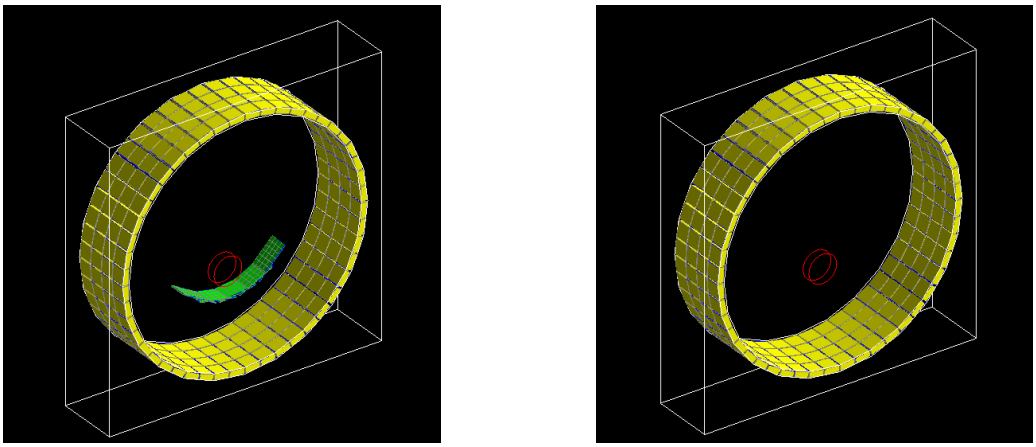

(a) (b)

Figure 4.5: (a) Configuration of VP-PET in GATE simulation. Insert panel at 5 positions are shown. (b) Configuration of scanner only in GATE simulation.

with a distance to the center of 137 mm, which is at the lowest possible bed position limited by the clinical scanner. The insert panel positions are shown in Figure 4.5a. In order to increase the coincidence sampling coverage, we use 5 positions practically chosen to avoid the patient bed according to our real experiment study. These 5 positions follow a circular trajectory where the insert is firstly moved down by 220 mm and then rotated around the center axial direction by -30, -20, 0, 20 and 30 degrees, sequentially. We acquired 200 seconds Scanner-Scanner and Insert-Scanner data at each position. During the reconstruction, we use a combination of 1000 seconds Insert-Scanner data to simulate a future design of insert panel with improved detection efficiency.

4.4.2 Experimental Phantom Study

The phantom used in the experimental study has the same spherical tumor pattern as the GATE simulated phantom. The cylinder has a longer length of about 12.7 cm. The total volume of tumors and background region are measured at 4 cc and 1040 cc, respectively. At

(a)

(b)

Figure 4.6: ^{18}F solution filled phantom

time of preparation, we injected the phantom with a total radioactivity of 1.96 mCi. The contrast ratio is kept at 4:1 while the background activity concentration is roughly 13 times typical clinical activity in a patient's body. Since F-18 has a short half life of 110 minutes and our experiments last for a few hours, we changed our data acquisition time for different experiments.

The insert panel is controlled by the robot and placed at exactly the same positions as described in Section 4.4.1. At the time of scan, our phantom still had a much higher activity

concentration level than typical clinical condition. So during the reconstruction process, we adjusted the number of events used for each insert position to compensate for activity decay and we only use 200 seconds equivalent counts in order to make a fair comparison with the Monte Carlo simulation. During our scan, the insert is always kept underneath the head holder which contains the phantom, maintaining enough safety margin required in future patient study.

4.5 Results

4.5.1 Simulation Results

We noticed an interesting statistical effect of the GATE simulation package when we reconstruct the same phantom image using different 200 second portions of the same piece of simulated data. In the scanner only configuration, Figure 4.7a provides very limited visibility of the 5 mm tumor and its contrast is not recovered well. Figure 4.7b and Figure 4.7c are both from the VP-PET configuration but only Scanner-Scanner data are used for image reconstruction. Their only difference is that they are reconstructed from different time segment of the same piece of simulation data. However we observed that the 5 mm tumor looks much sharper in Figure 4.7b than it looks in Figure 4.7c. In theory, due to the interference of the insert device, images from the scanner only should be better than images from VP-PET configuration with Scanner-Scanner data only. But here only the image in Figure 4.7c agrees with this. We hypothesize that under such a short acquisition time, detectability of such small tumors are affected by statistical noise, due to the low counts from them. The ability to resolve this 5 mm 4:1 tumor under 200 seconds scan time is uncertain for a whole

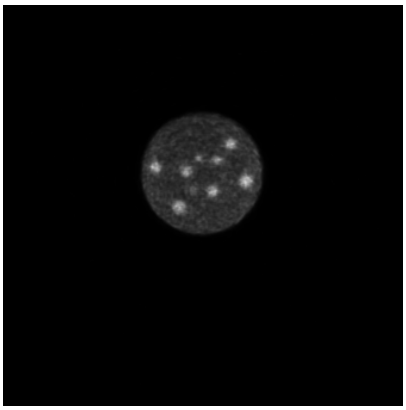

(a)

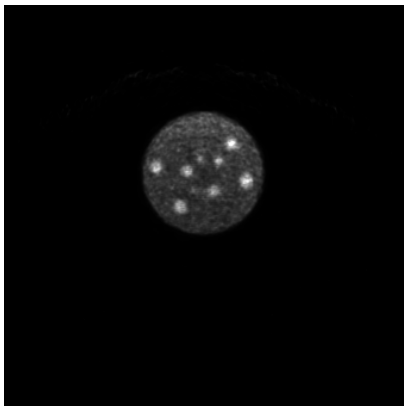

(b)

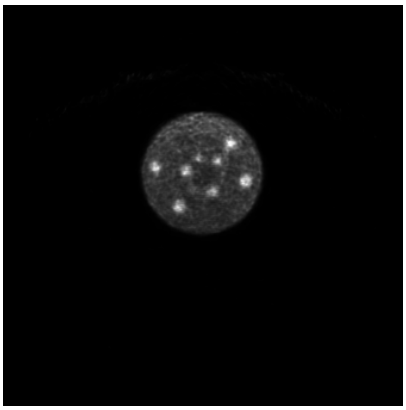

(c)

Figure 4.7: Reconstructed images at 30th iteration of 200 seconds equivalent simulation data with no penalty by (a) scanner only and (b) VP-PET using SS data set 1 only and (c) VP-PET using SS data set 2 only.

body scanner and VP-PET with SS data only. We also hypothesis that by incorporating the Insert-Scanner data, our VP-PET can consistently outperform a whole body scanner and a VP-PET system using its SS data only.

To prove this, we make the comparison by adding 5 positions of Insert-Scanner data to the Scanner-Scanner data used in Figure 4.7c to form a complete VP-PET data set. In order to show the benefit of using insert, we also compare with 400 seconds and 800 seconds of

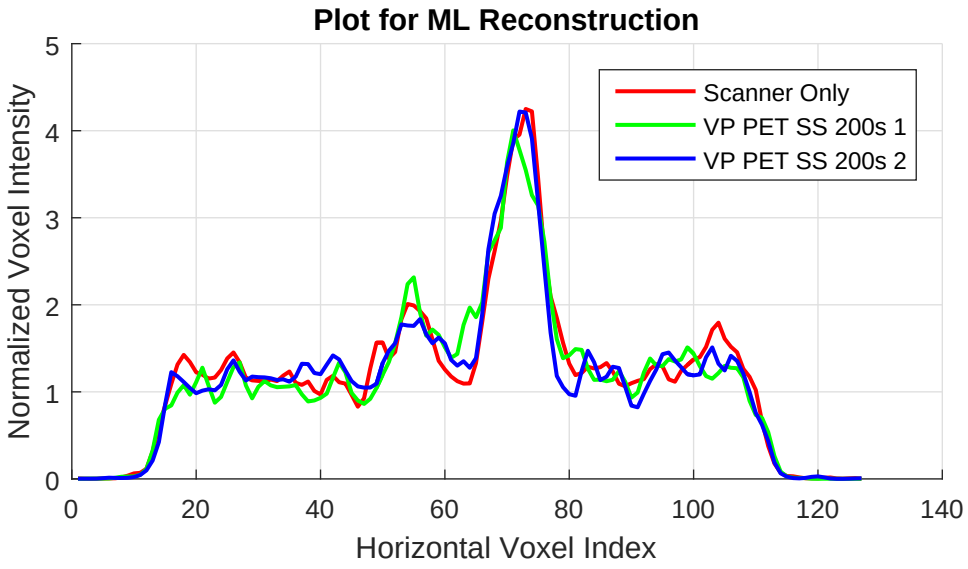

Figure 4.8: Plot of line profiles comparing images in Figure 4.7.

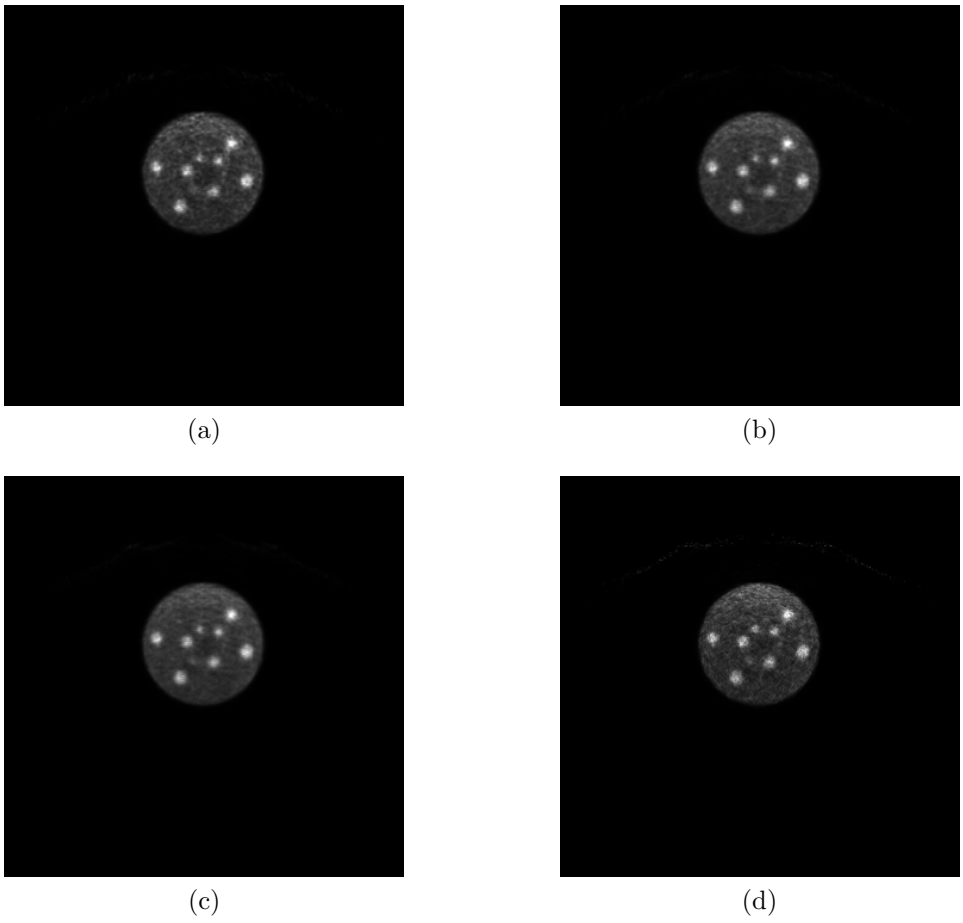

(a) (b)

(c) (d)

Figure 4.9: Reconstructed images at 30th iteration with no penalty by VP-PET using SS simulation data only of (a) 200 seconds and (b) 400 seconds and (c) 800 seconds data. Reconstructed images at 30th iteration with no penalty by VP-PET including Insert-Scanner data of (d) 200 seconds data.

SS data from VP-PET. Figure 4.9 shows the comparison of reconstructed images without applying a penalty.

The images in Figure 4.11 are reconstructed following the same configuration of Figure 4.9 but with a penalty applied to enforce smoother images.

With Insert-Scanner data, the contrast recovery of the 5 mm tumor is improved. In both non-penalized and penalized images, considering the peak to valley ratio of the 5 mm tumor,

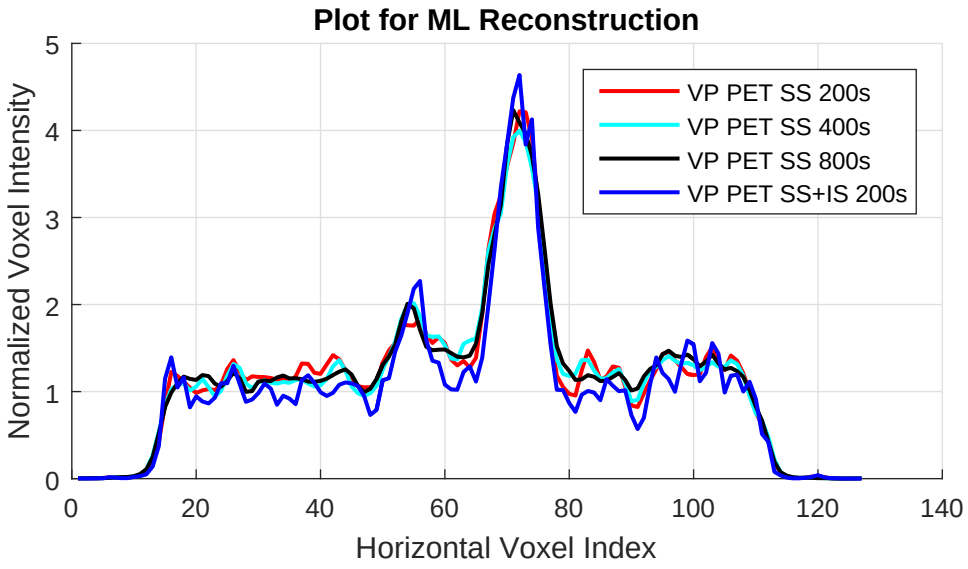

Figure 4.10: Plot of line profiles of Monte Carlo simulation VP-PET images reconstructed with no penalty in Figure 4.9.

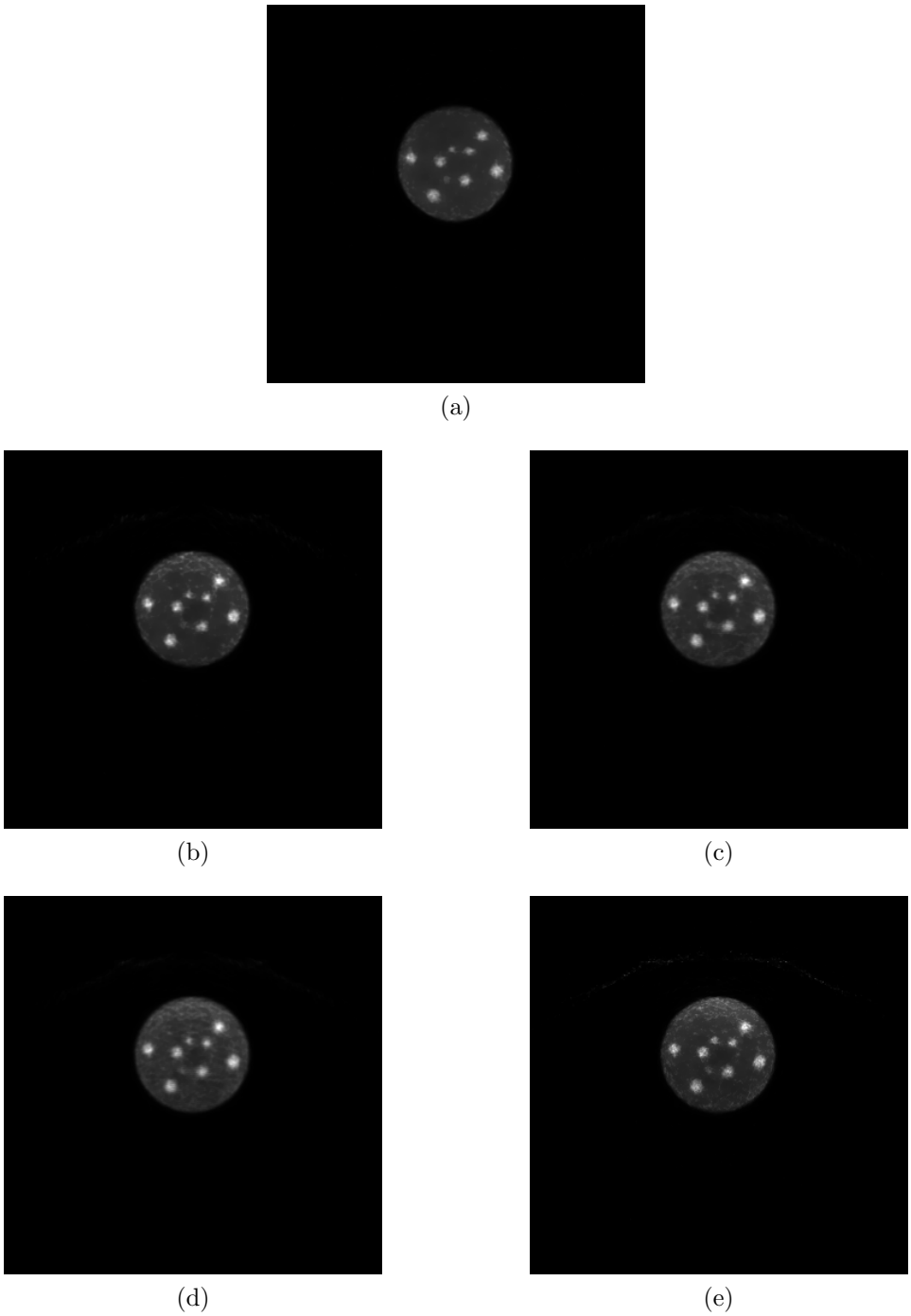

(a)

(b)

(c)

(d)

(e)

Figure 4.11: Reconstructed images at 30th iteration of 200 seconds equivalent simulation data with penalty by (a) scanner only. Reconstructed images at 30th iteration with penalty by VP-PET using SS simulation data only of (b) 200 seconds and (c) 400 seconds and (d) 800 seconds data. Reconstructed images at 30th iteration with penalty by VP-PET including Insert-Scanner data of (e) 200 seconds data.

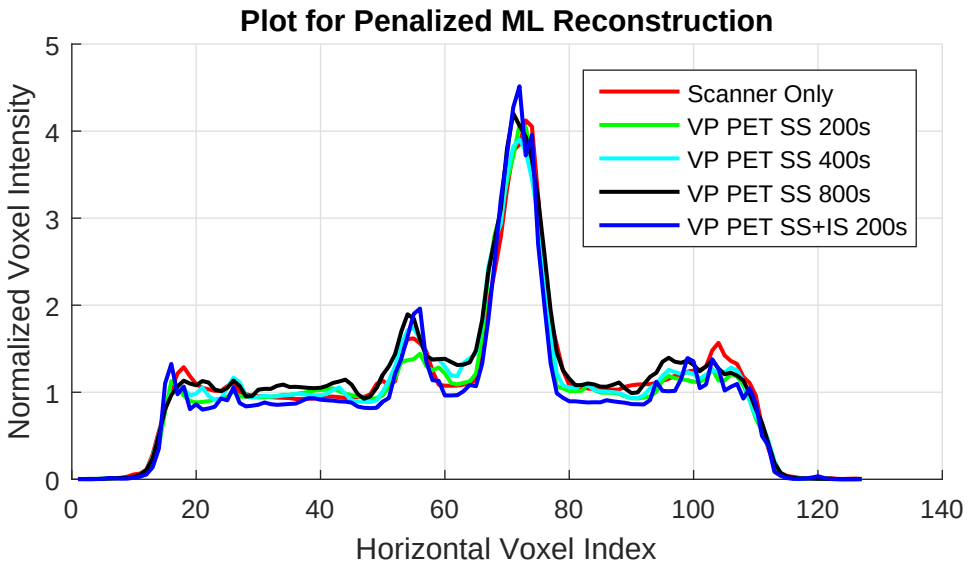

Figure 4.12: Plot of line profiles of Monte Carlo simulation VP-PET images reconstructed with penalty in Figure 4.11.

VP-PET with IS data out performs all other systems including using 800 seconds of SS data from VP-PET.

4.5.2 Experimental Results

We reconstructed images from the experimental phantom data using the same configuration as in the previous section. However, we do not notice any performance improvement by VP-PET. In fact, the detectability of most tumors in Figure 4.13c is even worse than that in the other two images. This unexpected experimental result disagrees with the Monte Carlo simulation results.

To find out the reason for this unexpected result that VP-PET with Insert-Scanner data even makes the image worse, we reconstructed the experimental and simulation data using Insert-Scanner events only. The experimental result in Figure 4.14a looks much worse than simulation image in Figure 4.14b. In the experimental case, there is almost no detectability in the Insert-Scanner image for small tumors and the image is full of artifacts in many regions. We understand the reason VP-PET can improve the image resolution is that Insert-Scanner events carry more information and the Insert-Scanner reconstructed images should have a higher resolution than the Scanner-Scanner images. In current situation, we can not expect any improvement from using these under performed Insert-Scanner data.

In the simulation and experimental data, the insert detector panel follows exactly the same trajectory. The simulation data validates that our image reconstruction works under a near ideal situation but the experimental data shows it fails under real situation. Most probable reasons for this include incorrect detector setup and inaccurate robot positioning. Since our

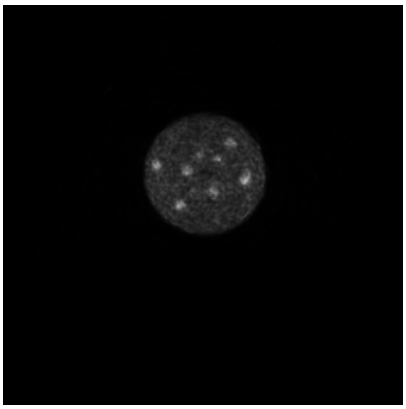

(a)

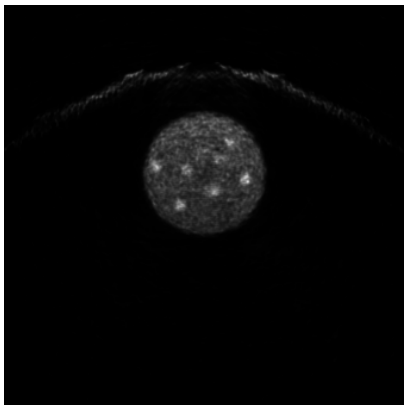

(b)

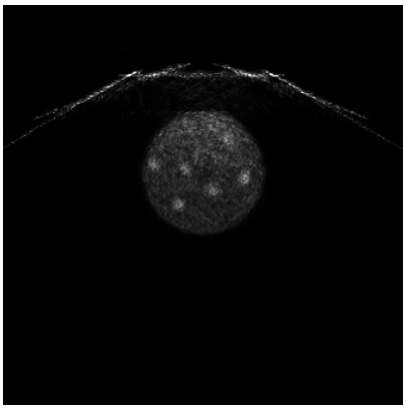

(c)

Figure 4.13: Reconstructed images at 30th iteration of 200 seconds equivalent experimental data with no penalty by (a) scanner only and (b) VP-PET using SS data only and (c) VP-PET using both SS and IS data.

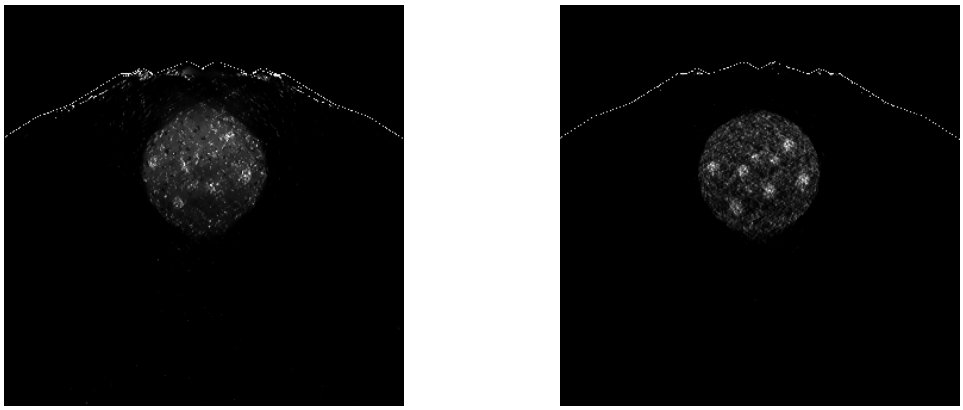

(a) (b)

Figure 4.14: Reconstructed images at 30th iteration of 200 seconds equivalent (a) experimental data and (b) simulation data, with no penalty by VP-PET using only IS data.

in house made detector panel has relatively large variations in the detection efficiency by individual crystals, complete normalization is crucial to compensate for this issue. Incomplete data correction will result in visible artifacts. Our robot positioning approach although has a proven accuracy of below 0.5 mm for placing a point source according to the Scanner-Scanner coincidence data, it is not guaranteed that our insert detector panel matches with the point source center. The machining work, assembly and installation of detectors and the tool measurement all introduce some kind of error that cannot be corrected by the only using Scanner-Scanner events. A joint Scanner-Scanner and Insert-Scanner data based calibration is required to align the two data sets properly in the 3D space.

4.6 Discussion

The results give us some insight on how to further optimize the design and application of this VP-PET system. We do observe a lack of detection efficiency in our current detector design. Although 3 mm detector thickness is a good choice for higher resolution, the sacrifice in

detection efficiency is significant. We see around 2% counts coming from insert-scanner when the insert is in the scanner FOV. Almost no improvement is observed when this amount of insert-scanner data is jointly reconstructed with scanner-scanner data. When we artificially triple our insert-scanner through Monte-Carlo simulation, we do see a visible improvement in the image quality. This means we need to find a better balance point between resolution and detection efficiency.

The artifacts in the Monte-Carlo images suggest that the data correction is not good enough. The bright edges may be a result of no scatter correction. With the robotic arm holding the insert moving in the scanner FOV, a new scatter correction strategy needs to be developed. We also see that the top region of the phantom is slightly brighter than the rest of the phantom. A probable cause for this is the attenuation correction of the insert. The current way of computing attenuation correction factor is based on assuming the voxel is spherical, to reduce computation load. However, when the insert detector is only 3 mm in thickness while the cubic voxels are 1 mm^3, this method may result in larger error when compared to exactly computing the interaction length of the ray path through the voxel.

The experiment data of VP-PET prototype shows marginal improvement over scanner only data. We suspect this is a result of the positioning error of the insert. Although we claim that we developed a calibration procedure that can achieve sub-mm precision, this is based on the assumption that the center of the carbon fiber case coincides with the center of the 8×4 insert crystals inside the case. However, due to installation tolerance, we expect there might be some inconsistency. To improve our experimental results to what is similar to the simulation results, we need to use a better calibration method that jointly estimates the offset from both the scanner-scanner data and the insert-scanner data.

Currently this image reconstruction framework only considers a weight coefficients between the scanner-scanner and insert-scanner data, which is enough for the Monte-Carlo study. For real experiments, component-based normalization is important to compensate for the variation in crystal efficiency. This GPU reconstruction can take crystal efficiency coefficient computed by our previous developed methods. However, all methods are developed for system with static geometry. While having an insert detector moving in space, the crystal efficiency varies with the facing angle and distance to scanner. A more complex component-based model is needed for this problem and it is challenging to estimate the parameters from an Insert-Scanner data set of limited time and from limited insert positions.

4.7 Conclusion

We have developed a robotic controlled VP-PET prototype system integrated with a clinical whole body scanner. We have demonstrated that our image reconstruction framework can handle a VP-PET system with arbitrary and dynamically changing geometry, through both Monte Carlo simulation and preliminary experimental data sets. The system integration is time consuming and we are still not achieving a satisfactory positioning precision. The image reconstruction framework uses existing statistic model and optimization methods. The GPU-based efficient implementation shows a potential to do reconstruction in similar amount of time of a typical bed scan. However the major innovation and unique feature of this entire framework is that it provides a relatively complete procedure to do robotic controlled VP-PET imaging. Although there are data correction components that need to

be further developed or improved, this serves as a tool for the starting point of robotic VP-PET. We expect to use this framework to investigate the optimal way to perform VP-PET scans for a variety of applications.

4.8 Future Development of Robotic VP-PET

In the current phase of robotic VP-PET development, we have limited our application to using pre-defined insert position and scan trajectory. This is a trade-off between the current insert detector capability and the image reconstruction speed. As we keep increasing our reconstruction speed by optimization and computational techniques, we expect to calculate the optimal scanning trajectory adaptively on-the-fly.

4.8.1 Targeted ROI imaging

The system can also be used in application where the best image quality is needed for a targeted ROI. As PET is a count limited imaging modality, counting statistics have a significant impact on the image quality in terms of detectability and quantification. In clinical imaging protocol, a patient will only be scanned for about 3 minutes at each bed position, which limits the coincidence events of detection and is a limiting factor on detectability of small lesions. This targeted zoom mode is suitable for application where an identified ROI has the highest impact on diagnosis and outcome. It requires a targeted ROI to be pre-selected by the doctor according to images from other modalities or previous scout PET image. Then the insert detector is controlled by the robot to be placed at the optimal position for this ROI, in up to three bed positions. The first and third bed position are prior

to and after the ROI is imaged by the center FOV of the scanner in the second bed position, respectively. In the first and third bed position, the insert is outside the scanner FOV and functions similar as the whole body surveillance mode. While in the second bed position, the insert is placed in side scanner FOV as studied in the current Monte Carlo simulation and experiments. When three data sets are used to jointly reconstruct the image, we maximized the counts from the ROI being detected and thus provides best possible image resolution and contrast recovery, without sacrificing the whole body imaging capability. This can be viewed as a direct extension to our first generation VP PET with additional isnert-scanner coincidence events from 2 more bed positions. It should be noted that it is possible the first bed position is not easily accessible by the robot using the current insert holder design.

4.8.2 Safety Concern

Having a robotic controlled insert detector moving around proximity of the patients creates great concern of the patient safety. We have already investigated multiple solutions including using the force torque sensor to detect any collision and using pre-defined safety region and forbidden zone to restrict the moving range of the insert. Although all these solutions have a good technical basis and are used in some industrial application, we are looking for more redundancy in the safety measure and robot control due to the nature that our insert need to be operating at a very close distance to the patient.

4.8.3 Adaptive Scan

There are already a lot of existing benefits that this insert system brings to whole body PET imaging including better detectability for smaller lesions and higher contrast recovery for

larger lesions. The power of having a robotic controlled insert system with a fast list-mode image reconstruction engine is not fully expressed until we actually fully use this system adaptively. There are literature study showing that better image quality can be achieved by adaptively placing the insert detector in angular direction where the ROI information carried by these insert-scanner LORs can be maximized. With a 6-DOF robot, our insert can have even more freedom when imaging a particular ROI. In the multi-bed surveillance mode, a ROI is first imaged by the scanner and then moved into the insert-scanner region in the next bed position. In this way, a preliminary image of the ROI is reconstructed using the fast reconstruction engine before starting the next bed position. By analyzing the tumor location, shape and structure, we can adaptively choose the optimal position to guide the insert placement in the next bed position. We are close to get a clinical image reconstructed within the time frame of one bed scan. The image reconstruction speed could further benefit from additional numerical acceleration techniques and increasing computation power brought by new hardware, which will make adaptive imaging practical.

Chapter 5

A Feasibility Study of a Point-of-Care PET System

We propose a portable, low-cost Point-of-Care PET imaging system platform that consists of one or more movable detectors in coincidence with a detector-array behind a patient. The detectors are hand movable so that the operator can control the scanning trajectory freely to achieve optimal coverage and sensitivity for patient-specific imaging tasks. This platform does not require a conventional full ring geometry, and as such it can be portable and low cost for bed-side or intraoperative imaging. We developed a prototype that consists of a compact high resolution MPPC detector mounted on a probe and a half ring of conventional detectors. The detector on the probe has 20×20 crystals of $0.74 \times 0.74 \times 3.0$ mm^3 each, in 0.8×0.8 mm^2 pitches, read out by a multi-pixel photon-counting (MPPC) array. The probe is attached to a MicroScribe® device (referred as microscribe in this chapter), which tracks the location and orientation of the probe in 3D space as it moves. We also performed Monte Carlo simulations for two POC-PET geometries with TOF (Time-Of-Flight) capability, one with a movable front panel and fixed back panel, the other one with both movable front and back panels. A fully 3D list-mode TOF image reconstruction algorithm has been developed to

incorporate the dynamically changing geometry information acquired from the microscribe. The algorithm is implemented on a GPU to achieve fast reconstruction (on the order of seconds), under practical count rate conditions. In this study, we report results from actual experiments using this prototype and a point source, as well as Monte Carlo studies with a Derenzo phantom using GATE.

5.1 Introduction

Typical clinical PET systems take up a full room and require patients be transported to the scanner. A low-cost, compact and mobile PET imager that can be brought to immobilized patients to provide important functional information may be of value.

Previous work on development of PET systems with unconventional geometry mainly aims at increasing image resolution for a specific application. Examples include virtual-pinhole PET [57], or zoom-in PET [65], whereby a high resolution detector is inserted into a conventional whole-body scanner. The joint image reconstruction of different types of coincidence data shows an improvement in image resolution and contrast recovery near the high resolution insert device [36]. In recent years, work has been reported on studies of integrating a probe type detector into a whole body scanner or a partial ring system [9, 23]. The latter type features highly incomplete sampling and methods are adopted to compensate for this issue.

Commercial SPECT systems with freehand movement capability [62] are entering the market. In such a system, a handheld probe of detectors replaces traditional detectors mounted on a gantry. Events detected by the gamma camera are registered and projected using the

position information from the optical tracking device. A major advantage of such a system is that they can be used in an intraoperative situation since it provides maximum flexibility and portability. For PET systems, the coincidence detection nature prevents people from building a PET scanner into only a single handheld device as portable as the freehand SPECT. However, PET offers significantly higher sensitivity than SPECT. Combined with the TOF detectors, a freehand PET system can potentially achieve higher image quality than a freehan SPECT system. Recently, the wide use of silicon-based photon multipliers makes it possible to build a very compact and light weight PET system with TOF capability. The EndoTOFPET-US collabration has reported building a dual modality PET/ultrasound system that consists of an endoscopic PET/ultrasound probe and external PET panel for high resolution of targeted imaging applications [40]. Similar to the freehand concept, both of the the endoscopic and external PET detectors are tracked. A certain degree of freedom of movement for the detectors is allowed so that they can provide tomographic information to reconstruct a 3D image.

The advantage of having freehand or maneuverable detectors is not limited to building high resolution insert probes. It can also be taken to build portable and flexible PET systems that provide adaptive imaging capability. Without using a full ring of detectors, much cost is saved. The lower cost and portability could possibly expand the clinical uses of PET and provide better support for nuclear medicine research and development. In this paper we describe a point-of-care PET (POC-PET) system that is built upon freehand manueverable detectors for imaging a region-of-interest.

Having maneuverable detectors allows us to do task specific scanning by adaptively changing the scanning trajectory, which includes the detector position, orientation, time duration and how these parameters are combined. In a limited angle imaging problem, the quality of the

final image will depend on how you design this trajectory and it is usually object dependent, which means there is not always a predetermined optimal trajectory. To achieve optimal image quality, one possible approach is that the scanning trajectory being progressively optimized during the scanning, based on interpreting the image reconstructed from accumulated data from the beginning of the scan. Since this is not a whole body PET scanner and only images a region-of-interest, it is also important to confirm that correct and useful information are collected before the end of a scan.

To solve these problems, timely image reconstruction is essential for this POC-PET. In high resolution 3D image reconstruction, due to the size of images and number of LORs, the system matrix requires a heavy computation and a large storage space. Two major types of implementation could be found based on whether the system matrix is precomputed or computed on-the-fly. The precomputed system matrix models more physical processes and numerical methods can be used to achieve high resolution image reconstruction, at the cost of computational complexity [29, 19, 21]. Methods that incorporate automatic system symmetry encoding and sparseness compression are used to reduce the size of the system matrix, however the computation cost is still too high for instant feedback [37]. Recently, GPU techonology is used to accelearte the image reconstruction and promising results are reported. For precomputed system matrices, due to limited memory of GPU, factorization is needed [67]. For on-the-fly system matrix computation, simplified model is used to fully utilize the massive parallel structure of GPUs [11, 42]. For list-mode data, on-the-fly computation avoids the low speed random access of GPU memory compared to using a precomputed system matrix. For POC-PET system, due to the dynamically changing geometry, symmetry is not useful to increase the speed and reduce the storage. As we want to get timely feedback from list-mode data, an on-the-fly projection engine is the best choice.

In this work, we report on a feasibility study of such systems using Monte Carlo simulation. Different POC-PET geometries are compared. We also report a prototype design based on this concept but without TOF capability.

5.2 Methods

5.2.1 Prototype System Design

A protype non-TOF PET demonstrating the point-of-care concept was built by integrating a MPPC based high resolution detector into an existing PS-PMT based half ring detector of a plant PET system. The MPPC detector was built in house and mounted on a cumstomized hand-held probe which allows free movement in space with its location and orientation being tracked by a microscribe. The half ring PS-PMT based detector is identical to the Siemense Inveon small animal PET [60].

5.2.1.1 Detectors Setup

The detector mounted on the microscribe uses a LYSO array with 20×20 crystals ($0.74 \times 0.74 \times 3$ mm^3 in 0.8 mm pitch size), coupled to a 4×4 MPPC array from Hamamatsu Photonics through a cumstomized light guide. It is set up to collect coincidence events with 32 Siemens Inveon block detectors arranged in a half ring geometry of 8 sectors and 4 blocks for each sector. Each Inveon block detector reads out a 20×20 LSO crystal array and each crystal has a size of $1.51 \times 1.51 \times 10$ mm^3 in 1.6×1.6 mm^2 pitch size. The diameter of the half ring system is 87.1 mm so this prototype is a for small animal or plant imaging.

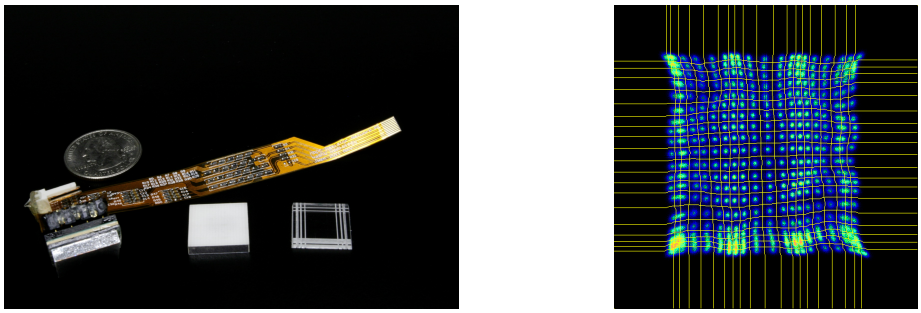

(a) (b)

Figure 5.1: (a) LYSO crystals, light guide, MPPC detector and resistor network on a flexboard. (b) Crystal segmentation of the 20 × 20 flood image

Figure 5.1 shows the LYSO array, light guide, MPPC detector and the resistor network on a flexboard. Further detector performance of the half ring detector can be found in [60].

5.2.1.2 Tracking The detectors

Several other groups have reported the use of electron magnetic tracking, mechanical tracking and vision based tracking technology for similar purposes [63, 40]. For this preliminary investigation, we chose to track the detector using the microscribe which is typically used to digitize 3D objects into computer models. Originally it takes point-by-point measurements on an object surface by touching through a stylus. By using the SDK we created our own program to track the detector moving in 3D space and record the time-stamped positions. The device has a semi-spherical working range of 0.63 meters in radius, with a spatial resolution of 0.05 mm, which meets the precision requirement for our experiment.

Prior to scanning, a coordinate registration process must be done in order to correlate the two separate systems. As the microscribe takes point-by-point measurement, we simply used it to measure points of several known positions on the half ring Inveon PET detectors and calculated the coordinate transform matrix. Define the affine transformation matrix

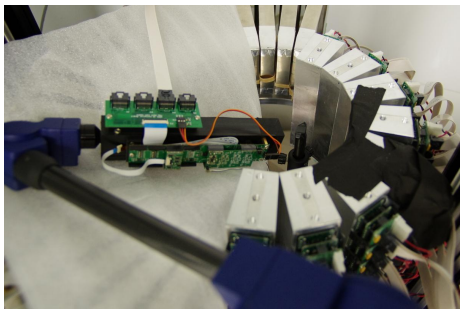

Figure 5.2: MPPC detector mounted on the microscribe in coincidence with a half ring Inveon detectors.

(rotation and translation) to be $T \in R^{4\times4}$. Let $\{\mathbf{x_1}, \mathbf{x_2}, ..., \mathbf{x_m}\}$ be m known positions in the PET half ring coordinate system, and $\{\mathbf{y_1}, \mathbf{y_2}, ..., \mathbf{y_m}\}$ be the corresponding measurement from the microscribe. Then the T is easily calculated using least-square-error method by:

$$T^t = (XX^t)^{-1}XY^t \tag{5.1}$$

$$\begin{pmatrix} y_x \\ y_y \\ y_z \\ 1 \end{pmatrix} = \begin{pmatrix} \mathbf{T_0} \in R^{3\times3} & \mathbf{b} \\ \mathbf{0} & 1 \end{pmatrix} \begin{pmatrix} x_x \\ x_y \\ x_z \\ 1 \end{pmatrix} = T \begin{pmatrix} x_x \\ x_y \\ x_z \\ 1 \end{pmatrix} \tag{5.2}$$

where $X \in R^{4\times m}$ is defined as,

$$X = \begin{pmatrix} \mathbf{x_1} & \mathbf{x_2} & \cdots & \mathbf{x_m} \\ 1 & 1 & \cdots & 1 \end{pmatrix} \tag{5.3}$$

$$Y = \begin{pmatrix} \mathbf{y_1} & \mathbf{y_2} & \cdots & \mathbf{y_m} \\ 1 & 1 & \cdots & 1 \end{pmatrix} \tag{5.4}$$

and $Y \in R^{4\times m}$ is defined in the same way.

During the scan, the microscribe continuously refreshes and records the coordinate and three rotation angles (roll, pitch, yaw) of the stylus (where the detector is mounted on through a holder) at 50 frames per second. The three normal vectors of the detector surfaces can be calculated through the three rotation angles. Both the coordinate of the detector center and the three normal vectors are be mapped into the PET half ring coordinate system by applying the transformation matrix T.

5.2.1.3 Imaging Experiment

A cubic Na-22 point source with 4 μCi activity was placed at a location slightly off center within the half ring FOV. 5.2 shows the experiment setup during a point source scan, where the cubic Na-22 point source is at the end of the black stick. The maneuverable detector probe was placed at 20 randomly selected positions by hand, roughly facing the point source. We acquired coincidence events for roughly 75 seconds per detector position. 5.5 shows the scanning positions and their relevant position to the point source and half ring system. The arrows in the figure represent where the center of LYSO crystal array was. Note that these scanning positions were randomly selected and we did not assign a specific order to them.

5.2.2 Monte-Carlo Simulation

We performed multiple Monte-Carlo simulation studies using GATE v6.2 to test this POC-PET concept for multiple flexible geometries, as well as study how TOF capability affects the image quality. We record all the singles streams from the output of different systems defined in the GATE simulation script. Then an offline sorting program was used to find all the coincidence events not only within the same system, but also across different systems. The sorting program also finds the true coincidences by comparing the event ID generated by GATE. The output of the sorting program are list-mode events with time stamped as to mimic the data format of the real system. The time stamps were used to correlate with the location data from the microscribe.

5.2.2.1 Simulation for Prototype Experiment

We performed a simulation based on experimental hardware setup and scanning trajectory to further explore the capability of this prototype. The random locations and orientations of the movable detector picked by hand during the actual experiment were recorded in a file, and then used to create a "generic movement" detector block in GATE, algined to the time stamp recorded by the microscribe. In the experiment, we did not accurately measure the position of the point source, thus we could not replicate the experiment in GATE by setting a same point source at the same position. However, we manually identified the position in the reconstructed image from the experimental data and used that position as an source input for GATE simulation.

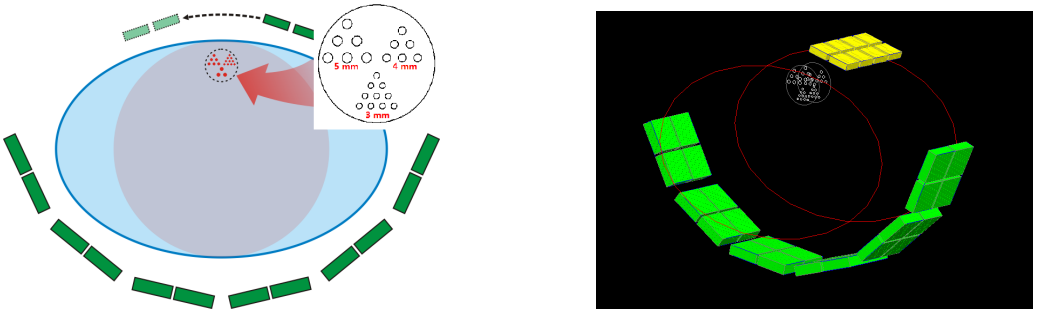

(a) (b)

Figure 5.3: Illustration of the scanning scheme of POC-PET Simulation Scenario 1 (a) showing the scanning trajectory of the front(top) panel (b) showing the system definition in GATE

5.2.2.2 POC-PET Simulation Scenario 1

In this design, we studied a human scale POC-PET system that consists of a moving panel detector in the front (upper) and a static arc of multiple panel detectors in the back (lower), as shown in Figure 5.3.

The front (upper) detector panel consists of 8 PET block detectors (2 transaxially, 4 axially). Each detector contains 16x16 LSO crystals of $1.92 \times 1.92 \times 10$ mm^3 each, arranged in 2 mm pitch. The rear (lower) detector panels consist of 24 PET block detectors arranged to form 6 panels of 2×2 arrays. Each detector contains 16×16 LSO crystals of $2.92 \times 2.92 \times 15$ mm^3 each, arranged in 3×3 mm pitch. Additional system parameters include:

- energy resolution: 15% FWHM;
- energy window: 350 650 keV;
- timing resolution: 200 (and 500) ps FWHM for individual detectors, 282 (and 705) ps FWHM for coincidence timing.

The object imaged to mimic a patient torso was an elliptical tube with the following parameters:

- semi-major axis: 20 cm;
- semi-minor axis: 13 cm;
- tube height: 20 cm;
- material: water.

Radioactivity in the torso phantom include a uniform background within the central cylindrical volume (radius=13 cm, height=20 cm) and 3 sectors of hot rods to simulate lesions (radius = 1.5, 2.0 and 2.5 mm, respectively; height = 30 mm). The spacing between hot rods is two times the diameter of the rods (typical Derenzo phantom pattern). Radionuclide was F-18; activity concentration was 0.14μCi/mL in the background (equivalent to 9.8 mCi of activity uniformly distributed in a 70 kg person). The contrast ratio between lesions and the background ranges from 6:1 to 21:1. The front detector panel was moved from one side of the lesions to the other side in 20 steps to collect coincidence events for a total of 20 minutes (1 min/step). For simplicity, in this simulation, the movement of the front panel has regular and uniform steps.

5.2.2.3 POC-PET Simulation Scenario 2

In this design, we re-arranged the block detectors to form larger panels, but reduced the total number of panels in the system, as shown in Figure 5.4. Compared to the fist POC-PET design, an important difference is that this design has a back panel moving in conjunction

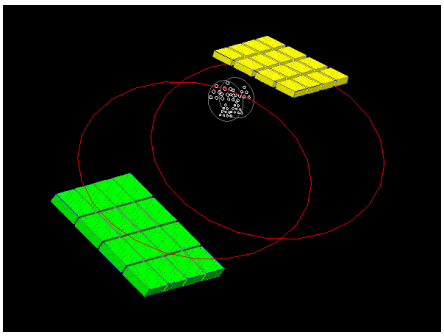

Figure 5.4: Illustration of the scanning scheme of POC-PET Simulation Scenario 2

with the front panel. In our simulation, we simply make the back panel rotate at roughly the same angular steps, so that the center of rotation of the front and back panels are roughly where the ROI is located. With moving capability for both panels, it is possible to keep them facing each other properly so that parallax error is reduced.

The front (upper) detector panel consists of 16 PET block detectors (4× transaxially, 4× axially). Each detector contains 16×16 LSO crystals of $1.92 \times 1.92 \times 10$ mm^3 each, arranged in 2×2 mm^2 pitch. The rear (lower) detector panel also consists of 16 PET block detectors (4 transaxially and 4 axially) but each detector contains 16×16 LSO crystals of $2.92 \times 2.92 \times 15$ mm^3 each, arranged in 3×3 mm^2 pitch. Additional system parameters are kept the same as those in the POC-PET Simulation Scenario 1.

5.2.3 Image Reconstruction

We have previously developed an 3D image reconstruction framework for unconventional PET system with arbitrary geometry. As with many conventional image reconstruction implementation, this framework incorporates symmetry computation and is running on a super computing cluster with scalability to multiple nodes through hybrid OpenMP and

MPI. However, despite the advantage of getting high precision quantitative images, this framework does not provide the flexibility to handle time-varying geometry and to do list-mode image reconstruction in a very fast manner. In this work, we developed a fully 3D list-mode TOF image reconstruction algorithm running on GPU, with additional capability to incorporate a time varying system geometry

5.2.3.1 Image Reconstruction for Multiple-Position Scanning

Although continuous freehand movement is our goal, the trajectory is discretized into a series of static locations. Each location is represented by a location vector (including crystal block center vector and its normal vectors), an absolute time and a time duration within which the moving detectors stayed static. Accounting for the different time duration at different locations requires slight modifications to data model of conventional PET image reconstruction.

We use the subscript $d = 1, 2, ..., N$ to represent a series of N discrete locations of the scanning trajectory for the moving detectors. The radionuclide concentration within a voxel is modeled as λ_j, where $j = 1, ..., J$ (number of voxels). We consider all λ_j to be time invariant through out the scanning procedure and post reconstruction decay correction method will be used. Within the $d - th$ scanning location, the total counts of emitted positrons from a voxel is approximated by a Poisson random variable with mean equal to $\lambda_j \tau_d$, where τ_d denotes the time duration for the maneuverable detector to be located at this position. We use $h_{t,i,j,d}$ to describe the TOF detector response function (system matrix), where t denotes TOF bins and i denotes line-of-response (LOR).

Consider the measurements of each LOR at different locations are independent, the joint log likelihood function is:

$$L(y|x) = \sum_d \sum_i \sum_t \{y_{i,d} \log(H_{t,i,j,d}\lambda_j\tau_d) - H_{t,i,j,d}\lambda_j\tau_d\} \tag{5.5}$$

Expectation maximization (EM) algorithm is used to seek the maximum likelihood (ML) solution for λ_j . The list-mode TOF ML-EM update equation can be described as:

$$\lambda_j^{(k+1)} = \frac{\lambda_j^{(k)}}{\sum_d \tau_d \sum_t \sum_i h_{(t,i,j,d)}} \sum_d \sum_m h_{t(m),i(m),j,d} \frac{\tau_d}{\sum_{j'} \lambda_{j'}^{(k)} \tau_d h_{t(m),i(m),j',d} + r_{i(m),d}} \tag{5.6}$$

where m is the index for list-mode events. As randoms and scatters are also dependent on the location of the moving detectors $r_{i(m),d}$ denotes the random and scatter counts for the LOR corresponding to the m-th event at the d-th location. The time duration τ_d at different locations affects the sensitivity term $\sum_d \tau_d \sum_t \sum_i h_{(t,i,j,d)}$, which requires computation of τ_d time-weighted backward projection of all LORs at each location and could be a speed limiting factor for image reconstruction when continuous movement of detectors is considered.

5.2.3.2 GPU Implementation

Since our system features a maneuverable detector that changes its position during the scan, pre-computed system response matrix usually used for static system does not provide enough flexibility. On-the-fly calculation of system response matrix is generally slower but could incorporate arbitrary geometric position of detectors as projecting list-mode events. For the same reason, symmetry is not taken into consideration.

In order to satisfy our goal that POC-PET could be moved to bed side and fast image reconstruction is essential to provide timely feedback to the scanner operator, we implemented our ML-EM algorithm on GPU using CUDA. To achieve faster speed and also to fit the massive parallel GPU architecture, we moved from Siddon's ray tracing method with sub-crystal division to a spacial invariant Gaussian function, to compute the geometric detector response matrix[11, 42]. For TOF reconstruction, a Gaussian kernel with FWHM determined by the system timing resolution was applied along the LOR direction, centered at the TOF bin center. We use a parallelization scheme similar to [11, 42], where the computation is parallelized in both voxel and data space. During forward projection, backward projection and image update, a group of voxels are simultaneously assigned to different blocks of threads. While within each block, threads loop through all the list mode events. So it is more analogous to a ray driven approach. In forward projection, voxel values are projected to be stored sequentially in the same order as list-mode events. This increase the memory access speed since coalesced reading and writing operations are achieved. In backward projection, the matched ray driven approach takes advantage of coalesced addressing at the cost of memory writing conflicts in image space. However, the conflicts could be easily handled by hardware atomic operation in recent newer generations of GPU devices.

Table 5.1: Image reconstruction parameters for 3 systems

System	Image FOV	Voxel Size	Number of LORs
POC-PET Prototype	$256 \times 256 \times 160$	$0.8 \times 0.8 \times 0.8$ mm^3	400×12800
POC-PET Simulation 1	$400 \times 400 \times 200$	$1.0 \times 1.0 \times 1.0$ mm^3	2048×6144
POC-PET Simulation 2	$400 \times 400 \times 200$	$1.0 \times 1.0 \times 1.0$ mm^3	4096×4096

Table 5.1 shows reconstruction parameters for the three different systems. Note that choosing the parameters for image FOV is critical to reach higher performance. This particular implementation relies on using the fast but very limited shared memory to speed up the projection. A very large FOV with very fine voxel size will result in splitting the image volume to fit into shared memory part by part, which will significantly reduce the reconstruction speed. In theoretical analysis, using an extra fine voxel size for a fixed crystal resolution will increase the computational load even more than the increase of number of voxels. For performance evaluation, we ran our program on a single Nvidia GTX Titan Black Edition graphis card, with 2880 stream processors. As our algorithm is parallelized in voxel space, it is not difficult to extend this algorithm for multiple GPU implementation.

5.2.4 Scan-Reconstruction-Rescan

We briefly demonstrate how one can potentially benefit from this POC-PET with its unique real time feedback information. The geometry used here is the same as that in Section 5.2.2.2 with a stationary back detectors arranged in an arc. For a particular region of interest, a scanning procedure can be customized according to the target shape and contrast ratio. Before an image is reconstructed, there is no information on how to design a task specific scanning procedure. In this POC-PET setup, as the scanning is in progress, images are continuously being reconstructed using accumulated coincidence events from the beginning of this scan process. Based on the preliminary images, one could decide whether more

scanning positions are needed to resolve the lesions, and/or more scanning time is needed to recover the contrast.

We use the POC-PET design with fixed back panel as an example. The 20 maneuverable front detector positions are sequentially grouped into 5 groups, with 4 positions inside each group. Since the 20 positions span only roughly 25 cm in horizontal direction, they are highly overlapped. Location 1, 10 or 11 and 20 do not overlap which means the trajectory can fit 3 non-overlapping detector positions. We grouped the 1st, 3rd and 5th data set to construct scanning trajectories which consist of these 3 groups of data in different order. For a predetermined ROI, better image quality can be achieved if more sampling angles are provided by coincidence LORs and more coincidence counts are detected from the ROI. This means we can optimized the positions used for the detector to improve image quality. The order of the scanning positions also matter since we want to get the images as fast as possible.

5.3 Results

5.3.1 Non-TOF Prototype Experiment and Simulation

5.3.1.1 Experimental Results

Shown in Figure 5.5 is the scanning trajectory of the experiment. The arrow is roughly where the center of detector front surface is located. All the 20 positions are randomly picked to maximize the coverage angle of the FOV. However, on one side the approaching angle of the probe is limited by the detector case of the half ring system. On the other side it is limited

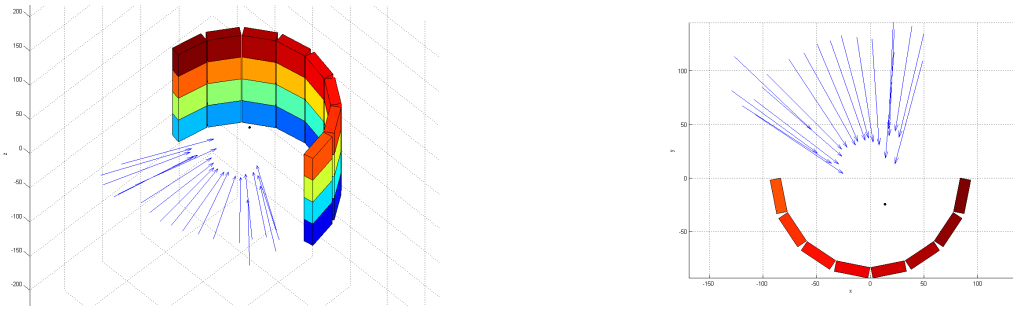

(a) (b)

Figure 5.5: Illustration of scanning trajectory drawn in Matlab (a) side view, (b) top view

by the range and degree of freedom of the miroscribe. As shown here, the sampling angle of the point source is less than 90 degrees from the probe detector's perspective.

Figure 5.6a shows the reconstructed image of the point source using experimental data. As we expected, there are visible blurring effect along the direction orthogonal to where LORs are missing (The reconstructed images have reversed Y axis compared to the Matlab drawing of the point source position). We cannot measure any performance properties solely from this point source experiment. We cannot claim the resolution of this system by using iterative reconstructed image of a point source with zero background activity. Because in such situation, image usually converges to a very few number of pixels thus producing artificial resolution. This experiment does validate the positioning accuracy to a certain extent. More quantitative experiments are needed to further investigate the tracking and positioning system.

5.3.1.2 Simulation Results

Shown in Figure 5.6b is the reconstructed image of the point source using Monte Carlo data. It is very similar to the experimental image except for that the point source in Monte

(a) (b)

Figure 5.6: Reconstructed image of (a) experimental data, (b) Monte Carlo simulation

Carlo image looks sharper and smaller. This is normal for most Monte Carlo study where all settings are nearly ideal. For example, the point source in Monte Carlo simulation is a point in theory while the experimental point source is a 0.5 mm source enclosed in a plastic disk. Besides such systematic factor, the positioning accuracy of the tracking system in our experiment is possibly the major contributor to this blurring. Detector assembly, probe machining and installation, microscribe calibration and coordinate system registration all involve a lot of hand operations and all the errors will propagate into the final image resolution.

5.3.2 POC-PET Simulation Scenario 1

Figure 5.7 shows the images reconstructed using different Coincidence Resolving Time (CRT) for POC-PET design with fixed back panels. We do not show the results using 6:1 contrast ratio here because even with 282 ps CRT, the rod tumors in this configuration are not resolvable. The purpose of this comparison is to illustrate the importance of good timing performance in this kind of limited angle PET scanning. As we can see, the first two

images with 282 ps CRT have much fewer artifacts in the background region than the other two images with 717 ps CRT. The later images exhibit artifacts related to the geometric arrangement of the back detector panels. We observe artificial activity distribution coming outside the simulated source region from places where there are gaps between the back detector panels. It is also noticed that the circular source shape is not well recovered near the bottom side. This is clearly because of the lack of horizontal LORs. Part of the artifacts also come from the fact that these images do not have attenuation correction applied. These artifacts are greatly reduced in the first two images simply because of better CRT. It is widely known that good TOF capability can improve the contrast recover and reduce noise level for limited angle systems. By comparing Figure 5.7b with Figure 5.7d, we clearly notice that all the tumors have better contrast and looks more circular when CRT is 282 ps. By comparing Figure 5.7a with Figure 5.7c we find that the big tumors which are not well separated in Figure 5.7c now becomes easily resolvable in Figure 5.7a. So, better CRT can help both improve contrast recovery and tumor detectability under low contrast situation.

Results shown in Figure 5.7 suggest that CRT 717 ps is not enough for our design of POC-PET with limited sampling angles. Considering the detector technology development recently, it is reasonable to plan the use of fast detectors that can achieve CRT 282 ps when we start to build our POC-PET systems. So in the following simulation studies, we fix the CRT at 282 ps and study the system performance of different design under different contrast ratio. Shown in Figure 5.8 are images from the fixed back panel design in 5.2.2.2, reconstructed from simulated data using different rods to background activity ratio. From Figure 5.8a to Figure 5.8d the ratio is 6:1, 11:1, 21:1 and no background activity, respectively. All rods in Figure 5.8a with a contrast ratio of 6:1 are not resolvable. In comparison, conventional whole body PET scanner has the ability to resolve some big tumors under such a contrast ratio, if enough scanning time is given. With from contrast ratio of 11:1,

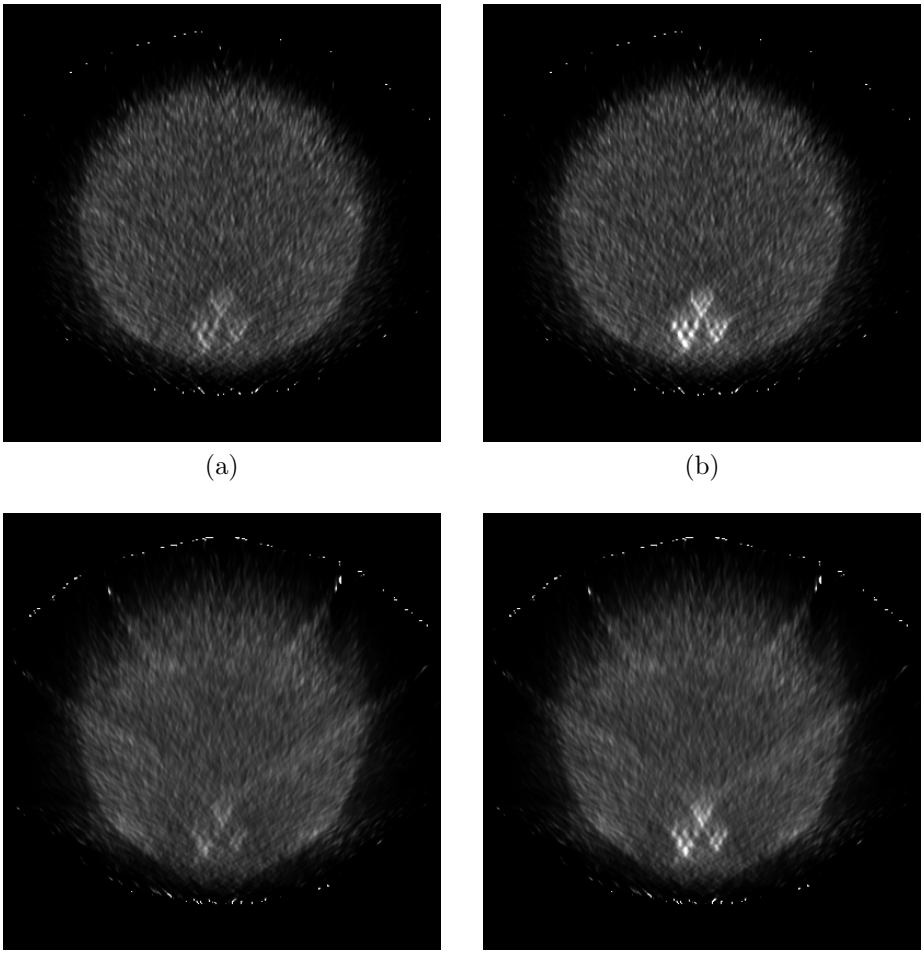

(a) (b)

(c) (d)

Figure 5.7: Reconstructed images for a body phantom with Derenzo-like pattern rods with different contrast ratio and CRT imaged by POC-PET design in 5.2.2.2: (a) contrast ratio 11:1, CRT 282 ps and (b) contrast ratio 21:1, CRT 282 ps and (c) contrast ratio 11:1, CRT 717 ps and (d) contrast ratio 21:1, CRT 717 ps.

5 mm rods become resolvable. We include the image for no background activity to show that this system is capable of resolving all the 3 types of rods under such an extreme case and the degradated image quality is due to inadequate rods to background activity ratio. It is noticed that the 5 mm and 4 mm rods in Figure 5.8d has different FWHM along the horizontal and vertical direction. This suggest a non-uniform spatial resolution (FWHM) of such kind of POC-PET system. This is expected due to the fact that POC-PET does not have a 360 degree full tomographic sampling. There is not enough information to regulate the estimation of activity distribution perpendicular to the missing sampling angles.

To better visualize the resolvability of the such a system under different contrast ratio, line profiles are plotted in Figure 5.9. Rods with diameter of 5 mm are resolvable in both 21:1 and 11:1 contrast ratio situation.

5.3.3 POC-PET Simulation Scenario 2

Shown in Figure 5.10 are images from the moving back panel design in 5.2.2.3, reconstructed from simulated data using different rods to background activity ratio. From Figure 5.10a to Figure 5.10d the ratio is 6:1, 11:1, 21:1 and no background activity, respectively. Compared with images from the static back panel design, images from this design with moving back panel have some advantage. In the lowest 6:1 contrast ratio case, 4 mm and 5 mm tumors are visible in Figure 5.10a while not visible in Figure 5.8a. In the 11:1 contrast ratio case, tumors in this moving panel design appear uniform in their shapes and are very well separated. However in the other design, the 5 mm tumors are mostly resolvable but obviously in a poorer shape while the 4 mm tumors are only marginally resolvable.

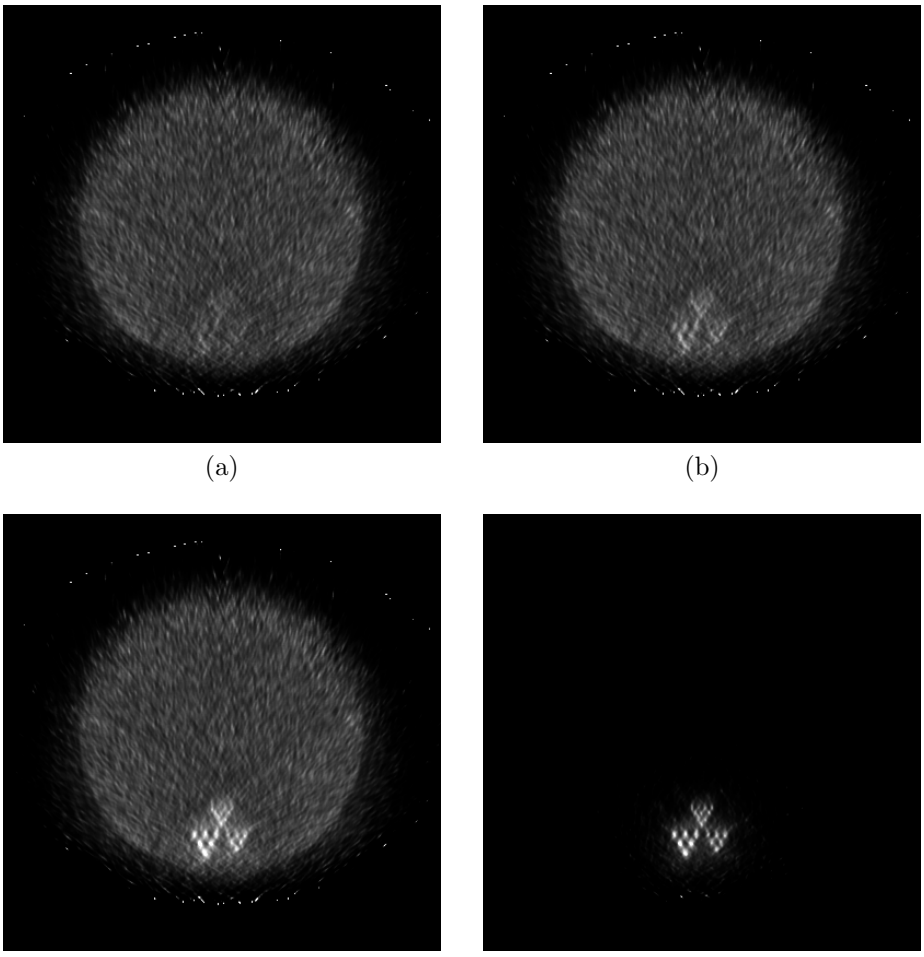

(a) (b)

(c) (d)

Figure 5.8: Reconstructed images for a body phantom with Derenzo-like pattern rods with different contrast ratio imaged by POC-PET design in 5.2.2.2 with CRT 282 ps: (a) contrast ratio 6:1 and (b) contrast ratio 11:1 and (c) contrast ratio 21:1 and (d) zero background activity.

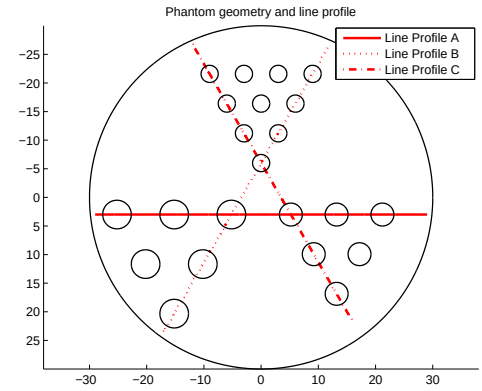

(a)

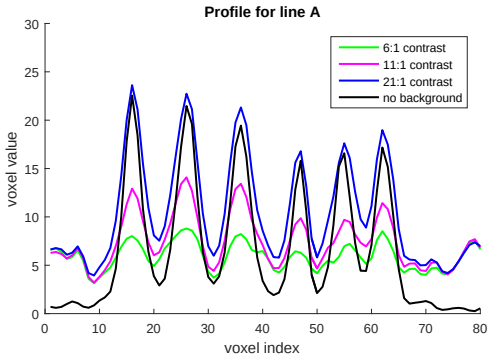

(b)

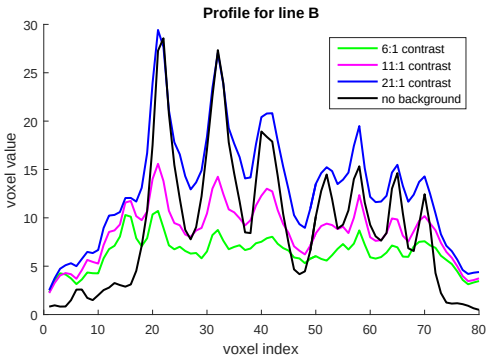

(c)

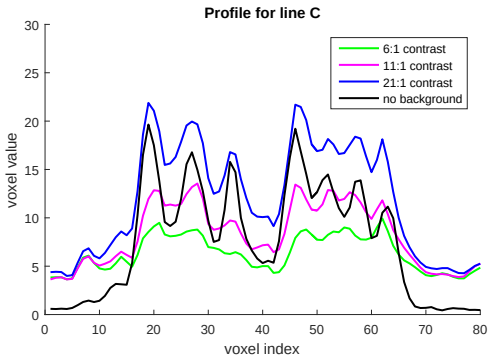

(d)

Figure 5.9: (a) The position of profiles related to the phantom. Plot of line profiles for images in Figure 5.8: (b) line profile A and (c) line profile B and (d) line profile C.

In terms of resolution in a local region, the second geometry design with moving back panel is more desirable. However we do notice that the cylindrical background activity region is not properly reconstructed as there are some regions completely missed by the LORs joining the front and back moving detectors. This illustrates a trade off between local resolution and the overall image FOV. The second design has larger front and back panels with more detectors in each panel, which leads to higher sensitivity and better axial coverage. The fact that there is only one front panel and only one back panel raises the need to rotate the panels in order to form enough in plane sampling coverage. If our FOV is properly located around the rotation center of the detectors, we can benefit from both the high sensitivity and large sampling angles, producing images of better resolution and contrast recovery. We may sacrifice some regions that are not our interest which will not be sampled by enough number of LORs. This provides a nice approach to design POC-PET systems with limited number of detectors while the choice of scanning trajectory in this design is patient dependent and needs to be carefully studied.

5.3.4 Scan-Reconstruction-Rescan

Images in Figure 5.11 are reconstructed by progressively using more data sets acquired from different sampling angles. The images values are normalized to the same level and shown in the same display window level in order to make the comparison. By looking at the images, individual tumors are not recovered when only the 1st data set is used, as shown in Figure 5.11a. By adding the 3rd data set, because of the increased sampling angle, most of the tumors are resolved as shown in Figure 5.11b. However, due to the lack of LORs from the direction where the 5th group of data orients, we noticed that this image has orientation dependent resolution. This is clearly shown in Figure 5.12f that line A and line

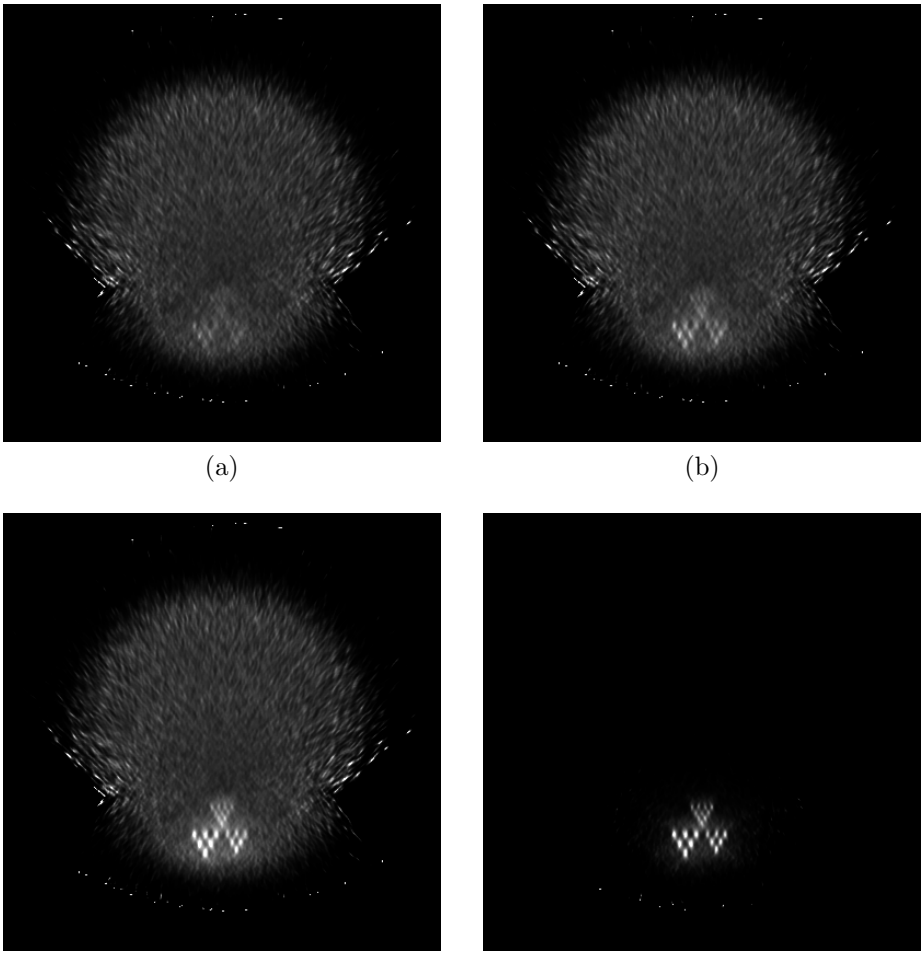

(a) (b)

(c) (d)

Figure 5.10: Reconstructed images for a body phantom with Derenzo-like pattern rods with different contrast ratio imaged by POC-PET design in 5.2.2.3: (a) Contrast ratio 6:1 (b) Contrast ratio 11:1 (c) Contrast ratio 21:1 (d) No background activity.

B are recovered well but line C has poorer separation between tumors. By adding the 5th data set, as shown in Figure 5.11c, resolution in the line C direction is improved and this can be verified by comparing the red and green curves in Figure 5.12d. The overall image quality is very similar to the image reconstructed using the entire data set.

This suggests that in order to get a decent image quickly, we do not need to follow every scanning position step-by-step. In future clinical application, we can potentially design a trajectory that quickly builds up complete sampling angles and then starts to fill in the gaps between them to improve the image quality. With the help of fast image reconstruction, we can get preliminary images before the complete scan is finished.

5.3.5 A Panel - Half Ring Scanner Example

We further illustrate the Point-Of-Care idea using a PET system built for the ACTIV-PET. Different from ACTIV-PET, we redesigned the scanning trajectory of the flat panel detector to allow larger coverage angle. In this experiment, the cylindrical phantom is positioned at the rough center of the clinical scanner. The panel detector is rotated from negative 90 degrees to positive 90 degrees around the z axis (axial direction) of the scanner, by a rotation radius of 128 mm. Data is acquired for around 5 minutes at every 15 degrees, for a total of 13 positions. To simulate the "back panel" of POC-PET, we only use data from the upper half of the whole body scanner ring in coincidence with the flat panel detector. In the ideal case, the detector pairs enabled should change accordingly with the panel position. However, in clinical PET, this involves re-program the FPGA of the coincidence processor which cannot be done on-the-fly. So we took a simplified approach with fixed combination of crystal pairs between the panel and the scanner, where only the upper half portion is enabled.

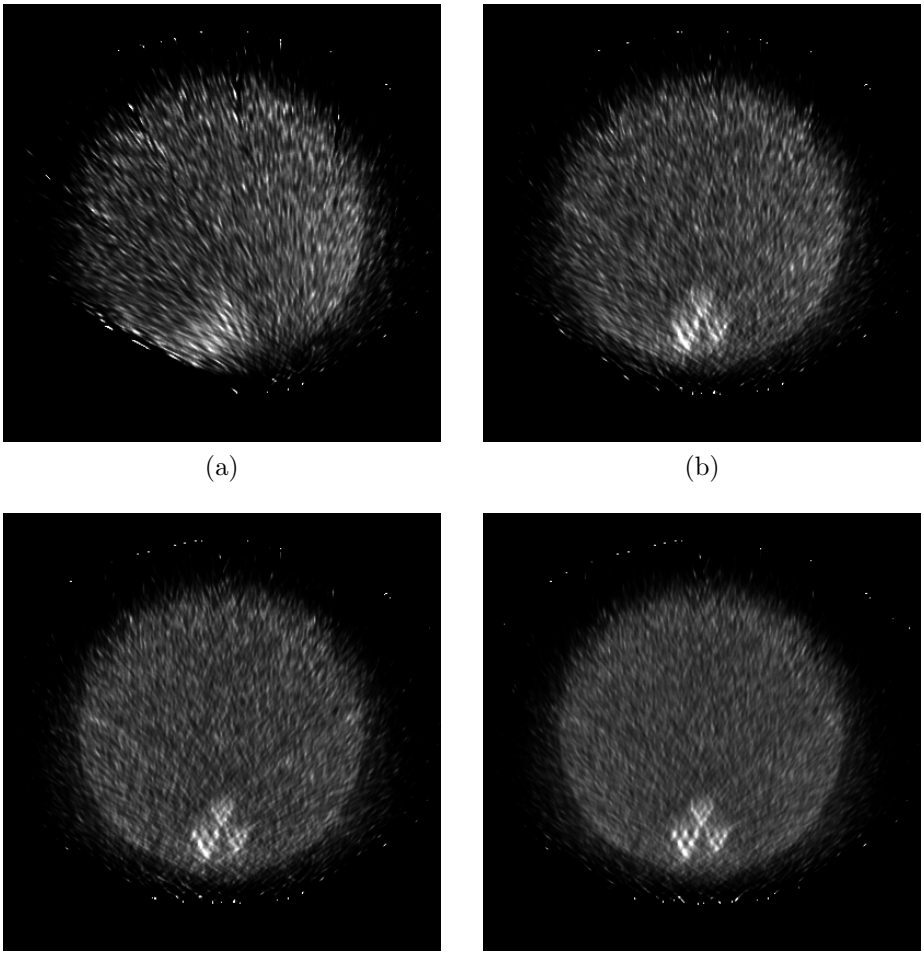

(a) (b)

(c) (d)

Figure 5.11: Image reconstructed at 15th iteration of 21:1 background activity using CRT 282 ps from data set acquired at (a) 1st group of positions, (b) 1st and 3rd group of positions, (c) 1st, 3rd and 5th group of positions, (d) all groups of positions.

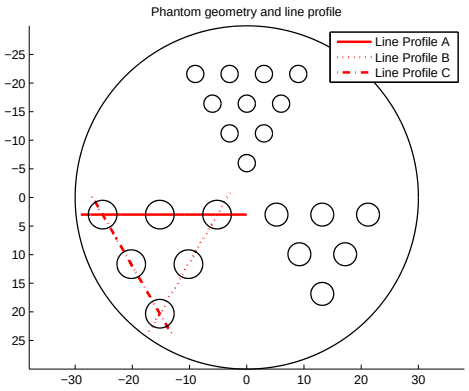

(a)

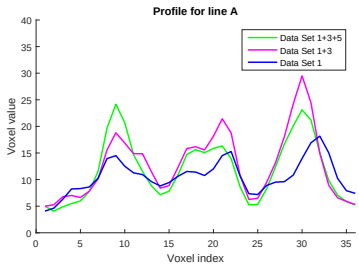

(b)

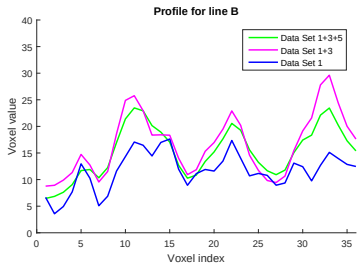

(c)

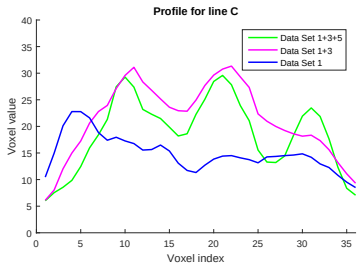

(d)

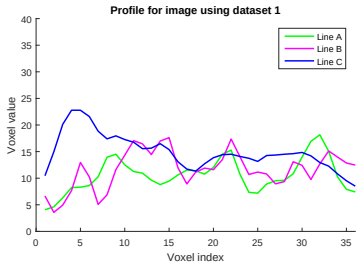

(e)

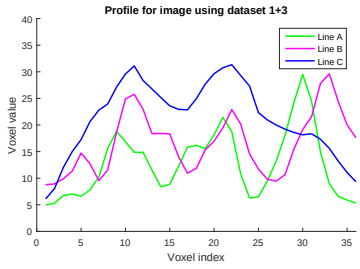

(f)

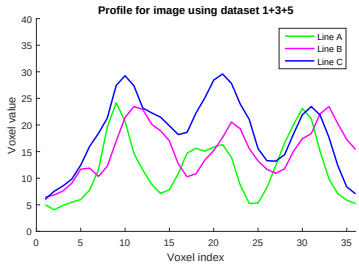

(g)

Figure 5.12: Line profile for reconstructed images in Figure 5.11.(a) The position of profiles A, B and C related to the phantom. Line profiles showing the voxel value of (b) line profile A, (c) line profile B, (d) line profile C, in images reconstructed using different groups of data. Line profiles A, B and C in images reconstructed from (a) 1st group of data, (f) 1st and 3rd group of data, (g) 1st, 3rd and 5th group of data.

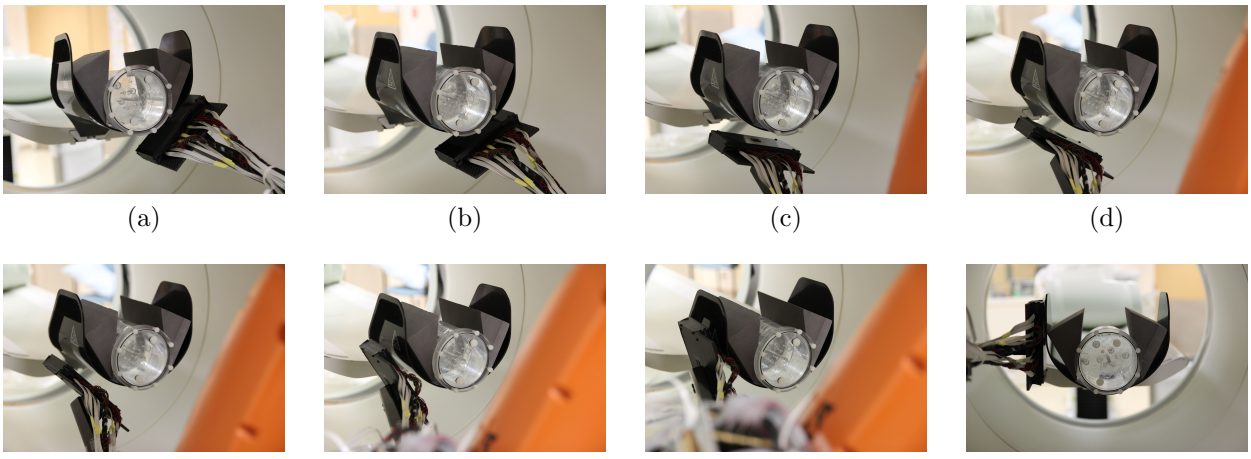

(a) (b) (c) (d)

(e) (f) (g) (h)

Figure 5.13: Experiment setup of using robotic controlled flat panel detector together with Siemens Biograph 40 whole body scanner to demonstrate the idea of Point-Of-Care PET

Fig 5.13 illustrates the scanning trajectory in this experiments. Photos are taken after data acquisition is done, which may not reflect the exact position where data is being acquired. During the data collection, we scan the first position for 211 seconds and normalized the scanning time for the rest of positions for decay correction. Since the activity concentration level at the time of scan was higher than the normal 5285 Bq/cc, the scanning time at each positions is roughly 350 seconds equivalent to 200 seconds scan of normal concentration. List mode GPU image reconstruction is used to reconstruct only the panel-scanner events of 13 positions, totaling 21 million counts. This number is roughly the same as a 200 seconds equivalent scan of the same phantom of normal activity concentration by the scanner only. By maintaining such a similar level of coincidence counts we can compares the image quality across different systems.

Image of this system is reconstructed with a $320 \times 320 \times 224$ image volume of voxel size $1 \times 1 \times 1$ mm^3. Due to the limited number of counts and smaller FOV size, it only takes 8 seconds per iteration for non-penalized ML reconstruction to run on a 4 GTX Titan X system.

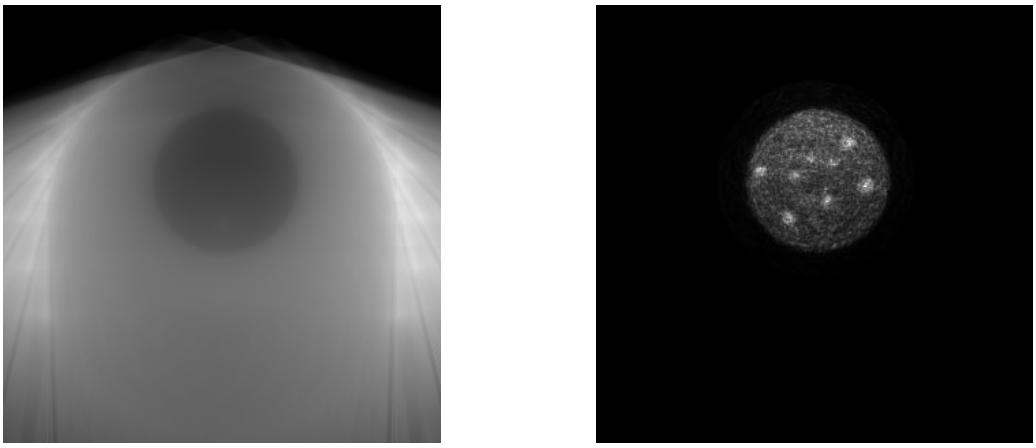

(a) (b)

Figure 5.14: (a) Sensitivity image showing the relative position between panel positions and the phantom. (b) The 20th iteration of ML reconstructed images using panel-scanner only prompt events

Figure 5.14 shows the maximum likelihood reconstructed image at 20th iteration of the panel-scanner system to demonstrate the POC-PET idea. Compared to the images reconstructed by the whole body scanner or the robotic VP-PET in Chapter 4, this image shows higher noise level and poorer resolution for small tumors. The smallest 2 tumors are not resolvable in this image. As we have explained in Chapter 4, the current hardware setup is likely to have some systematic positioning error that needs to be corrected. We expect better image quality from this setting once the error is corrected.

5.4 Discussion and Conclusion

We have demonstrated through simulation a new type of PET system design suitable for use in point of care situation. Compared to conventional whole body scanner, this new type of PET system consists of fewer number of detectors and readout channels, resulting in much lower cost and compactness. For the system we simulate, it has 32 block detectors

in total, which is only about 1/6 of a clinical scanner. We compared two different geometry implementation, one with a static arc of detectors in the back, the other one with a moving flat panel of detectors in the back. A resolution improvement could be seen in the second geometry implementation however it has smaller FOV.

We also showed that customized scanning for different imaging tasks using POC-PET could potentially save the scanning time. While scanning, images are being reconstructed to help the operator decide if additional scanning is need or not. In some cases, lesions with higher contrast ratio need less scanning time so that not all tasks are scanned at a fixed time.

We demonstrated the POC-PET concept on a larger scale panel-scanner PET system and the corresponding image reconstruction running on a multi-GPU workstation. We noticed that the images are very noisy and exhibit different kinds of artifacts. A very likely reason for this is due to our robot positioning accuracy during the entire experiment. Since our robot system is only calibrated using a scanner based approaching, the carbon fiber housing of the panel detector is accurately positioned but the crystals inside the housing may not be well positioned. Many artifacts also relates to the lack of crystal efficiency normalization. In this case because our flat panel detector array has a large variations in detection efficiency of different crystals, not correcting for them will end up with visible artifact in the images.

We investigated some essential technology for POC-PET systems. Time-of-flight capability is essential to make this POC-PET to be useful. Since POC-PET does not provide complete sampling angles even with moving the maneuverable detectors around a ROI, non-TOF data does not provide enough information to resolve the rods in all directions. It is known that contrast recover ratio also depends on the sensitivity of the system. System with fewer sampling angles tend to have poorer contrast recover. We show through simulation it is hard to recover activity distribution with low tumor-to-background contrast ratio and POC-PET

typically has worse contrast recover than whole body PET scanner. It is reported that TOF information improves the image quality in terms of signal to noise ratio, contrast recover ratio by reducing uncertainty along the LOR. Our simulation results show 300 ps may be a base line for requirement of timing resolution for POC-PET.

It is possible to move this POC-PET to patient bedside for a variety of applications. The maneuverable detectors in this design allow dynamic geometry change during the scan. For a local region of interest, this could partially compensate the incomplete sampling angles caused by limited number of detectors and result in improved image quality. We show that with additional information from TOF capability, 5 mm rods are resolvable in human scale simulation setup. We also demonstrated a GPU implementation of a fast fully 3D list mode image reconstruction with capability to handle this dynamic changing geometry. For a practical count rate when imaging a patient, timely feedback could be achievable. A natural extension of this work will be using the instant feedback from reconstructed images to guide the ongoing scanning procedure (for example, optimize the scanning trajectory) in real time to get improved images.

In our work, all images are reconstructed assuming the detectors having uniform sensitivity, invariant to many factors that could happen during a real scan. In practical situation, normalization is essential to get quantitatively accurate images especially when considering a dynamically changing geometry. Compared to conventional PET system with static geometry, the dynamic changing geometry of POC-PET makes it favorable to use component based normalization instead of direct LOR based normalization. This is because there could be infinite number of possible combinations of scanning positions which leads to a low count rate for each LOR and this could make direct LOR normalization very noise. In component based normalization, dynamically changing geometry adds extra degrees of freedom to the

parameter space of component-based normalization. A way to acquire the minimal data for normalization of POC-PET system requires future investigation.

Image reconstruction implement on GPU devices significantly reduces the computation time (reported by several groups). Although same or even faster speed is achievable using a super computing cluster, a single computer with multiple GPUs will be much more favorable to POC-PET since it could be compactly integrated and made low cost. In theory, a single GPU has no more than one order of magnitude higher computation power than a multiple core single CPU. Further optimization is need to achieve even more significant speed up. With dynamically changing geometry, an important part of the optimization is to find an efficient on-the-fly forward/backward projection engine that fully utilize the massive parallel structure of GPUs. Compared to offline computation of system matrix where we can use numerical methods to ensure accuracy, the projection engine we use here is a spatial invariant Gaussian kernel applied to the LOR connecting the surface center of the crystal pair, which is a trade off between speed and accuracy. With no sub crystal division, this method suffers from incorrect modeling of parallax effect. However, as a potential advantage of a POC-PET system, the scanning trajectory can be designed to minimize this effect.

Attenuation correction is challenging for POC-PET system as there is no integrated CT scanner. In ideal situation where the PET scanner has very high TOF resolution, it is possible to estimate the attenuation image while reconstructing the emission image simultaneously, without using a CT scan[12, 45, 46]. This could be one option for PET systems without other robust attenuation correction tools. However, the POC-PET has a limited angle of sampling and this makes it more difficult to estimate the correct attenuation image.

References

[1] S. Agostinelli, J. Allison, K. Amako, J. Apostolakis, H. Araujo, P. Arce, M. Asai, D. Axen, S. Banerjee, G. Barrand, F. Behner, L. Bellagamba, J. Boudreau, L. Broglia, A. Brunengo, H. Burkhardt, S. Chauvie, J. Chuma, R. Chytracek, G. Cooperman, G. Cosmo, P. Degtyarenko, A. Dell'Acqua, G. Depaola, D. Dietrich, R. Enami, A. Feliciello, C. Ferguson, H. Fesefeldt, G. Folger, F. Foppiano, A. Forti, S. Garelli, S. Giani, R. Giannitrapani, D. Gibin, J.J. Gómez Cadenas, I. González, G. Gracia Abril, G. Greeniaus, W. Greiner, V. Grichine, A. Grossheim, S. Guatelli, P. Gumplinger, R. Hamatsu, K. Hashimoto, H. Hasui, A. Heikkinen, A. Howard, V. Ivanchenko, A. Johnson, F.W. Jones, J. Kallenbach, N. Kanaya, M. Kawabata, Y. Kawabata, M. Kawaguti, S. Kelner, P. Kent, A. Kimura, T. Kodama, R. Kokoulin, M. Kossov, H. Kurashige, E. Lamanna, T. Lampén, V. Lara, V. Lefebure, F. Lei, M. Liendl, W. Lockman, F. Longo, S. Magni, M. Maire, E. Medernach, K. Minamimoto, P. Mora de Freitas, Y. Morita, K. Murakami, M. Nagamatu, R. Nartallo, P. Nieminen, T. Nishimura, K. Ohtsubo, M. Okamura, S. O'Neale, Y. Oohata, K. Paech, J. Perl, A. Pfeiffer, M.G. Pia, F. Ranjard, A. Rybin, S. Sadilov, E. Di Salvo, G. Santin, T. Sasaki, N. Savvas, Y. Sawada, S. Scherer, S. Sei, V. Sirotenko, D. Smith, N. Starkov, H. Stoecker, J. Sulkimo, M. Takahata, S. Tanaka, E. Tcherniaev, E. Safai Tehrani, M. Tropeano, P. Truscott, H. Uno, L. Urban, P. Urban, M. Verderi, A. Walkden, W. Wander, H. Weber, J.P. Wellisch, T. Wenaus, D.C. Williams, D. Wright, T. Yamada, H. Yoshida, and D. Zschiesche. Geant4a simulation toolkit. *Nuclear Instruments and Methods in Physics Research Section A: Accelerators, Spectrometers, Detectors and Associated Equipment*, 506(3):250–303, 2003.

[2] J. Allison, K. Amako, J. Apostolakis, H. Araujo, P. Arce Dubois, M. Asai, G. Barrand, R. Capra, S. Chauvie, R. Chytracek, G.A.P. Cirrone, G. Cooperman, G. Cosmo, G. Cuttone, G.G. Daquino, M. Donszelmann, M. Dressel, G. Folger, F. Foppiano, J. Generowicz, V. Grichine, S. Guatelli, P. Gumplinger, A. Heikkinen, I. Hrivnacova, A. Howard, S. Incerti, V. Ivanchenko, T. Johnson, F. Jones, T. Koi, R. Kokoulin, M. Kossov, H. Kurashige, V. Lara, S. Larsson, F. Lei, O. Link, F. Longo, M. Maire, A. Mantero, B. Mascialino, I. McLaren, P. Mendez Lorenzo, K. Minamimoto, K. Murakami, P. Nieminen, L. Pandola, S. Parlati, L. Peralta, J. Perl, A. Pfeiffer, M.G. Pia, A. Ribon, P. Rodrigues, G. Russo, S. Sadilov, G. Santin, T. Sasaki, D. Smith, N. Starkov, S. Tanaka, E. Tcherniaev, B. Tome, A. Trindade, P. Truscott, L. Urban, M. Verderi, A. Walkden, J.P. Wellisch, D.C. Williams, D. Wright, and H. Yoshida. Geant4 developments and applications. *IEEE Transactions on Nuclear Science*, 53(1):270–278, feb 2006.

[3] J. Allison, K. Amako, J. Apostolakis, P. Arce, M. Asai, T. Aso, E. Bagli, A. Bagulya, S. Banerjee, G. Barrand, B.R. Beck, A.G. Bogdanov, D. Brandt, J.M.C. Brown, H. Burkhardt, Ph. Canal, D. Cano-Ott, S. Chauvie, K. Cho, G.A.P. Cirrone, G. Cooperman, M.A. Cortés-Giraldo, G. Cosmo, G. Cuttone, G. Depaola, L. Desorgher, X. Dong, A. Dotti, V.D. Elvira, G. Folger, Z. Francis, A. Galoyan, L. Garnier, M. Gayer, K.L. Genser, V.M. Grichine, S. Guatelli, P. Guèye, P. Gumplinger, A.S. Howard, I. Hivnáčová, S. Hwang, S. Incerti, A. Ivanchenko, V.N. Ivanchenko, F.W. Jones, S.Y. Jun, P. Kaitaniemi, N. Karakatsanis, M. Karamitros, M. Kelsey, A. Kimura, T. Koi, H. Kurashige, A. Lechner, S.B. Lee, F. Longo, M. Maire, D. Mancusi, A. Mantero, E. Mendoza, B. Morgan, K. Murakami, T. Nikitina, L. Pandola, P. Paprocki, J. Perl, I. Petrović, M.G. Pia, W. Pokorski, J.M. Quesada, M. Raine, M.A. Reis, A. Ribon, A. Ristić Fira, F. Romano, G. Russo, G. Santin, T. Sasaki, D. Sawkey, J.I. Shin, I.I. Strakovsky, A. Taborda, S. Tanaka, B. Tomé, T. Toshito, H.N. Tran, P.R. Truscott, L. Urban, V. Uzhinsky, J.M. Verbeke, M. Verderi, B.L. Wendt, H. Wenzel, D.H. Wright, D.M. Wright, T. Yamashita, J. Yarba, and H. Yoshida. Recent developments in Geant4. *Nuclear Instruments and Methods in Physics Research Section A: Accelerators, Spectrometers, Detectors and Associated Equipment*, 835:186–225, 2016.

[4] N Aubry, E Auffray, F B Mimoun, N Brillouet, R Bugalho, E Charbon, O Charles, D Cortinovis, P Courday, A Cserkaszky, C Damon, K Doroud, J M Fischer, G Fornaro, J M Fourmigue, B Frisch, B Fürst, J Gardiazabal, K Gadow, E Garutti, C Gaston, A Gil-Ortiz, E Guedj, T Harion, P Jarron, J Kabadanian, T Lasser, R Laugier, P Lecoq, D Lombardo, S Mandai, E Mas, T Meyer, O Mundler, N Navab, C Ortigão, M Paganoni, D Perrodin, M Pizzichemi, J O Prior, T Reichl, M Reinecke, M Rolo, H C Schultz-Coulon, M Schwaiger, W Shen, A Silenzi, J C Silva, R Silva, I Somlai Schweiger, R Stamen, J Traub, J Varela, V Veckalns, V Vidal, J Vishwas, T Wendler, C Xu, S Ziegler, and M Zvolsky. EndoTOFPET-US: a novel multimodal tool for endoscopy and positron emission tomography. *Journal of Instrumentation*, 8(04):C04002, 2013.

[5] E Auffray, F Ben Mimoun Bel Hadj, N Brillouet, P Coudray, K Doroud, G Fornaro, B Frisch, S Gundacker, A Knapitsch, P Jarron, T Meyer, M Paganoni, K Pauwels, M Pizzichemi, M Vangeleyn, and P Lecoq. Design and performance of detector modules for the endoscopic PET probe for the FP7-project EndoTOFPET-US. In *Nuclear Science Symposium and Medical Imaging Conference (NSS/MIC), 2012 IEEE*, pages 3236–3240, oct 2012.

[6] H H Barrett, T White, and L C Parra. List-mode likelihood. *Journal of the Optical Society of America. A, Optics, image science, and vision*, 14(11):2914–23, nov 1997.

[7] Christina Bluemel, Andreas Schnelzer, Asli Okur, Alexandra Ehlerding, Stefan Paepke, Klemens Scheidhauer, and Marion Kiechle. Freehand SPECT for image-guided sentinel lymph node biopsy in breast cancer. *European journal of nuclear medicine and molecular imaging*, 40:1656–61, 2013.

[8] C A Bouman. Model Based Image Processing. In *https://engineering.purdue.edu/˜bouman/publications/pdf/MBIP-book.pdf*, 2015.

[9] K Brzeziński, J F Oliver, J Gillam, and M Rafecas. Study of a high-resolution PET system using a Silicon detector probe. *Physics in Medicine and Biology*, 59(20):6117–6140, oct 2014.

[10] C. Byrne. Likelihood maximization for list-mode emission tomographic image reconstruction. *IEEE Transactions on Medical Imaging*, 20(10):1084–1092, 2001.

[11] Jing-yu Cui, Guillem Pratx, Sven Prevrhal, and Craig S. Levin. Fully 3D list-mode time-of-flight PET image reconstruction on GPUs using CUDA, 2011.

[12] Michel Defrise, Ahmadreza Rezaei, and Johan Nuyts. Time-of-flight PET data determine the attenuation sinogram up to a constant. *Phys. Med. Biol.*, 57:885–899, 2012.

[13] Frederic H Fahey. Data acquisition in PET imaging. *Journal of nuclear medicine technology*, 30(2):39–49, jun 2002.

[14] F Garibaldi, S Capuani, S Colilli, L Cosentino, F Cusanno, R De Leo, P Finocchiaro, M Foresta, F Giove, F Giuliani, M Gricia, F Loddo, M Lucentini, B Maraviglia, F Meddi, E Monno, P Musico, A Pappalardo, R Perrino, A Ranieri, A Rivetti, F Santavenere, and C Tamma. TOPEM: A PET-TOF endorectal probe, compatible with MRI for diagnosis and follow up of prostate cancer. *Nucl. Instruments Methods Phys. Res. Sect. A Accel. Spectrometers, Detect. Assoc. Equip.*, 702:13–15, feb 2013.

[15] F. Garibaldi, R. De Leo, A. Ranieri, F. Loddo, M. Floresta, C. Tamma, A. Gabrielli, F. Giorgi, F. Cusanno, P. Musico, R. Perrino, P. Finocchiaro, L. Cosentino, A. Pappalardo, F. Meddi, B. Maraviglia, F. Giove, T. Gili, S. Capuani, M. Turisini, N. Clinthorne, S. Huh, S. Majewski, M. Lucentini, M. Gricia, F. Giuliani, and E. Monno. TOPEM: A multimodality probe (PET TOF, MRI, and MRS) for diagnosis and follow up of prostate cancer. *IEEE Nuclear Science Symposuim & Medical Imaging Conference*, pages 2442–2444, 2010.

[16] E Garutti. EndoTOFPET-US a novel multimodal tool for endoscopy and Positron Emission Tomography. In *Nuclear Science Symposium and Medical Imaging Conference (NSS/MIC), 2012 IEEE*, pages 2096–2101, oct 2012.

[17] R.L. Harrison, S.D. Vannoy, D.R. Haynor, S.B. Gillispie, M.S. Kaplan, and T.K. Lewellen. Preliminary Experience With The Photon History Generator Module Of A Public-domain Simulation System For Emission Tomography. In *1993 IEEE Conference Record Nuclear Science Symposium and Medical Imaging Conference*, pages 1154–1158. IEEE.

[18] E.J. Hoffman, T.M. Guerrero, G. Germano, W.M. Digby, and M. Dahlbom. PET system calibrations and corrections for quantitative and spatially accurate images. *IEEE Transactions on Nuclear Science*, 36(1):1108–1112, 1989.

[19] J Hu, J Qi, J S Huber, W W Moses, and R H Huesman. {MAP} image reconstruction for arbitrary geometry {PET} systems with application to a prostate-specific scanner. In *Proc. Intl. Mtg. on Fully 3D Image Recon. in Rad. and Nuc. Med*, pages 416–420, 2005.

[20] H.M. Hudson and R.S. Larkin. Accelerated image reconstruction using ordered subsets of projection data. *IEEE Transactions on Medical Imaging*, 13(4):601–609, 1994.

[21] R H Huesman, G J Klein, William W Moses, Jinyi Qi, Bryan W Reutter, and P R G Virador. List-mode maximum-likelihood reconstruction applied to positron emission mammography (PEM) with irregular sampling. *Medical Imaging, IEEE Transactions on*, 19(5):532–537, may 2000.

[22] Sam S. Huh, Neal H. Clinthorne, and W. L. Rogers. Investigation of an internal PET probe for prostate imaging. *Nuclear Instruments and Methods in Physics Research, Section A: Accelerators, Spectrometers, Detectors and Associated Equipment*, 579:339–343, 2007.

[23] Sam S. Huh, Eric Cochran, Klaus Honscheid, Harris Kagan, Shane Smith, W. L. Rogers, and Neal H. Clinthorne. The first generation prototype of a surgical PET imaging probe system. In *IEEE Nuclear Science Symposuim & Medical Imaging Conference*, pages 3197–3204, 2010.

[24] Sam S. Huh, W. L. Rogers, and Neal H. Clinthome. On-line sliding-window list-mode PET image reconstruction for a surgical PET imaging probe. In *IEEE Nuclear Science Symposium Conference Record*, pages 5479–5484, 2008.

[25] S.S. Huh, Li Han Li Han, W.L. Rogers, and N.H. Clinthorne. Real time image reconstruction using GPUs for a surgical PET imaging probe system. In *2009 IEEE Nuclear Science Symposium Conference Record (NSS/MIC)*, 2009.

[26] S Jan, D Benoit, E Becheva, T Carlier, F Cassol, P Descourt, T Frisson, L Grevillot, L Guigues, L Maigne, C Morel, Y Perrot, N Rehfeld, D Sarrut, D R Schaart, S Stute, U Pietrzyk, D Visvikis, N Zahra, and I Buvat. GATE V6: a major enhancement of the GATE simulation platform enabling modelling of CT and radiotherapy. *Physics in Medicine and Biology*, 56(4):881–901, feb 2011.

[27] S Jan, G Santin, D Strul, S Staelens, K Assié, D Autret, S Avner, R Barbier, M Bardiès, P M Bloomfield, D Brasse, V Breton, P Bruyndonckx, I Buvat, A F Chatziioannou, Y Choi, Y H Chung, C Comtat, D Donnarieix, L Ferrer, S J Glick, C J Groiselle,

D Guez, P-F Honore, S Kerhoas-Cavata, A S Kirov, V Kohli, M Koole, M Krieguer, D J van der Laan, F Lamare, G Largeron, C Lartizien, D Lazaro, M C Maas, L Maigne, F Mayet, F Melot, C Merheb, E Pennacchio, J Perez, U Pietrzyk, F R Rannou, M Rey, D R Schaart, C R Schmidtlein, L Simon, T Y Song, J-M Vieira, D Visvikis, R Van de Walle, E Wieërs, and C Morel. GATE: a simulation toolkit for PET and SPECT. *Physics in Medicine and Biology*, 49(19):4543–4561, oct 2004.

[28] Judith E. Kalinyak, Wendie A. Berg, Kathy Schilling, Kathleen S. Madsen, Deepa Narayanan, and Marie Tartar. Breast cancer detection using high-resolution breast PET compared to whole-body PET or PET/CT. *European Journal of Nuclear Medicine and Molecular Imaging*, 41(2):260–275, feb 2014.

[29] Daniel B Keesing, Aswin Mathews, Sergey Komarov, Heyu Wu, Tae Yong Song, Joseph A O'Sullivan, and Yuan-Chuan Tai. Image reconstruction and system modeling techniques for virtual-pinhole PET insert systems. *Physics in Medicine and Biology*, 57(9):2517–2538, may 2012.

[30] Christina Kreisch, Raymond E Arvidson, Joseph A O'Sullivan, Ke Li, Daniel Politte, Justin Finkel, Edward Guinness, Nathaniel Stein, and Abigail Fraeman. Log-Likelihood Method of Reducing Noise in CRISM Along-Track Oversampled Hyperspectral Images. In *Imaging and Applied Optics 2015*, page CM4E.5. Optical Society of America, 2015.

[31] K Lange and R Carson. EM reconstruction algorithms for emission and transmission tomography. *Journal of computer assisted tomography*, 8(2):306–16, apr 1984.

[32] Ke Li, A J Mathews, Qiang Wang, Jie Wen, J A O'Sullivan, and Yuan-Chuan Tai. Preliminary Results from a Portable PET Probe System with Fast Image Reconstruction. In *Nuclear Science Symposium and Medical Imaging Conference (NSS/MIC), 2014 IEEE*, 2014.

[33] Ke Li, Aswin Mathews, Qiang Wang, Jie Wen, Joseph O'Sullivan, and Yuan-chuan Tai. A Feasibility Study of Point-of-Care PET System. In *Society of Nuclear Medicine and Molecular Imaging Annual Meeting*, volume 56, page 436, 2015.

[34] Lawrence MacDonald, John Edwards, Thomas Lewellen, David Haseley, James Rogers, and Paul Kinahan. Clinical imaging characteristics of the positron emission mammography camera: PEM Flex Solo II. *Journal of nuclear medicine : official publication, Society of Nuclear Medicine*, 50(10):1666–75, oct 2009.

[35] A J Mathews, Ke Li, S Komarov, Qiang Wang, B Ravindranath, J A O'Sullivan, and Yuan-Chuan Tai. An image reconstruction framework for arbitrary positron emission tomography geometries. In *Nuclear Science Symposium and Medical Imaging Conference (NSS/MIC), 2013 IEEE*, pages 1–6, oct 2013.

[36] Aswin John Mathews, Sergey Komarov, Heyu Wu, Joseph A O'Sullivan, and Yuan-Chuan Tai. Improving PET imaging for breast cancer using virtual pinhole PET half-ring insert. *Phys. Med. Biol.*, 58(18):6407, 2013.

[37] Aswin John Mathews, Ke Li, Sergey Komarov, Qiang Wang, Bosky Ravindranath, Joseph A. O'Sullivan, and Yuan-Chuan Tai. A generalized reconstruction framework for unconventional PET systems. *Medical Physics*, 42(8):4591–4609, jul 2015.

[38] Debashish Pal, Joseph A O'Sullivan, Heyu Wu, Martin Janecek, and Yuan-Chuan Tai. 2D linear and iterative reconstruction algorithms for a PET-insert scanner. *Physics in Medicine and Biology*, 52(14):4293–4310, jul 2007.

[39] M E Phelps, E J Hoffman, N A Mullani, and M M Ter-Pogossian. Application of annihilation coincidence detection to transaxial reconstruction tomography. *Journal of nuclear medicine : official publication, Society of Nuclear Medicine*, 16(3):210–24, mar 1975.

[40] M Pizzichemi. Development of EndoTOFPET-US, a multi-modal endoscope for ultrasound and time of flight positron emission tomography. *J. Instrum.*, 9(02):C02002, 2014.

[41] Lucreiu M Popescu and Robert M Lewitt. Small nodule detectability evaluation using a generalized scan-statistic model. *Physics in Medicine and Biology*, 51(23):6225–6244, dec 2006.

[42] Guillem Pratx, Suleman Surti, and Craig Levin. Fast List-Mode Reconstruction for Time-of-Flight PET Using Graphics Hardware. *IEEE Transactions on Nuclear Science*, 58:105–109, 2011.

[43] Homayoon Ranjbar, Jie Wen, Aswin J Mathews, Sergey Komarov, Qiang Wang, Ke Li, Joseph A O'Sullivan, and Yuan-Chuan Tai. A simultaneous beta and coincidence-gamma imaging system for plant leaves. *Physics in Medicine and Biology*, 61(9):3572–3595, may 2016.

[44] Bosky Ravindranath, Jie Wen, Aswin Mathews, Sergey Komarov, Heyu Wu, Farrokh Dehdashti, Joseph O'Sullivan, and Yuan-Chuan Tai. *The Journal of nuclear medicine : JNM.*, volume 53. Society of Nuclear Medicine, 2012.

[45] A Rezaei, M Defrise, G Bal, C Michel, M Conti, C Watson, and J Nuyts. Simultaneous Reconstruction of Activity and Attenuation in Time-of-Flight PET. *IEEE Trans. Med. Imaging*, 31(12):2224–2233, 2012.

[46] A Rezaei, M Defrise, and J Nuyts. ML-reconstruction for TOF-PET with Simultaneous Estimation of the Attenuation Factors. *Med. Imaging, IEEE Trans.*, 33(7):1563–1572, 2014.

[47] Alejandro Sanchez-Crespo. Comparison of Gallium-68 and Fluorine-18 imaging characteristics in positron emission tomography. *Applied Radiation and Isotopes*, 76:55–62, 2013.

[48] L. A. Shepp and Y. Vardi. Maximum Likelihood Reconstruction for Emission Tomography. *IEEE Transactions on Medical Imaging*, 1(2):113–122, oct 1982.

[49] Robert L. Siddon. Fast calculation of the exact radiological path for a three-dimensional CT array. *Medical Physics*, 12(2):252–255, mar 1985.

[50] Donald L. Snyder and David G. Politte. Image Reconstruction from List-Mode Data in an Emission Tomography System Having Time-of-Flight Measurements. *IEEE Transactions on Nuclear Science*, 30(3):1843–1849, 1983.

[51] R Stevenson and E Delp. Fitting curves with discontinuities. In *Proc. of the first international workshop on robust computer vision*, pages 127–136, 1990.

[52] A. Studen, D. Burdette, E. Chesi, V. Cindro, N.H. Clinthorne, E. Cochran, B. Grosicar, K. Honscheid, H. Kagan, C. Lacasta, G. Llosa, V. Linhart, M. Mikuz, V. Stankova, Z. Weilhammer, and D. Zontar. Performance of the MADEIRA PET probe prototype. *2009 IEEE Nuclear Science Symposium Conference Record (NSS/MIC)*, 2009.

[53] A. Studen, E. Chesi, V. Cindro, N.H. Clinthorne, E. Cochran, B. Grošičar, K. Honscheid, H. Kagan, C. Lacasta, G. Llosa, V. Linhart, M. Mikuž, V. Stankova, P. Weilhammer, and D. Žontar. A silicon PET probe. *Nuclear Instruments and Methods in Physics Research Section A: Accelerators, Spectrometers, Detectors and Associated Equipment*, 648:S255–S258, aug 2011.

[54] Andrej Studen, Enrico Chesi, Vladimir Cindro, Neal H. Clinthorne, Eric Cochran, Borut Grosicr, Klaus Honscheid, S. S. Huh, Harris Kagan, Carlos Lacasta, Gabriela Llosa, Vladimir Linhart, Marko Mikuz, Vera Stankova, Peter Weilhammer, and Dejan Zontar. Report on the MADEIRA PET probe. *IEEE Nuclear Science Symposuim & Medical Imaging Conference*, pages 1755–1758, 2010.

[55] S Surti, M E Werner, and J S Karp. Study of PET scanner designs using clinical metrics to optimize the scanner axial FOV and crystal thickness. *Physics in Medicine and Biology*, 58(12):3995–4012, jun 2013.

[56] Suleman Surti, Adam R. Shore, and Joel S. Karp. Design Study of a Whole-Body PET Scanner With Improved Spatial and Timing Resolution. *IEEE Transactions on Nuclear Science*, 60(5):3220–3226, oct 2013.

[57] Yuan-Chuan Tai, Heyu Wu, Debashish Pal, and Joseph A O'Sullivan. Virtual-pinhole PET. *Journal of nuclear medicine : official publication, Society of Nuclear Medicine*, 49(3):471–9, mar 2008.

[58] Kris Thielemans, Sanida Mustafovic, and Charalampos Tsoumpas. STIR: Software for Tomographic Image Reconstruction Release 2. In *2006 IEEE Nuclear Science Symposium Conference Record*, pages 2174–2176. IEEE, 2006.

[59] N. Tomic, C.J. Thompson, and M.E. Casey. Investigation of the "block effect" on spatial resolution in PET detectors. In *2003 IEEE Nuclear Science Symposium. Conference Record (IEEE Cat. No.03CH37515)*, pages 2201–2205 Vol.3. IEEE, 2003.

[60] Qiang Wang, Aswin J Mathews, Ke Li, Jie Wen, Sergey Komarov, Joseph a O'Sullivan, and Yuan-Chuan Tai. A dedicated high-resolution PET imager for plant sciences. *Physics in medicine and biology*, 59(19):5613–5629, sep 2014.

[61] Qiang Wang, Jie Wen, Bosky Ravindranath, Andrew W. OSullivan, David Catherall, Ke Li, Shouyi Wei, Sergey Komarov, and Yuan-Chuan Tai. A compact high resolution flat panel PET detector based on the new 4-side buttable MPPC for biomedical applications. *Nuclear Instruments and Methods in Physics Research Section A: Accelerators, Spectrometers, Detectors and Associated Equipment*, 794:151–159, 2015.

[62] Thomas Wendler, Alexander Hartl, Tobias Lasser, Joerg Traub, Farhad Daghighian, Sibylle I Ziegler, and Nassir Navab. Towards intra-operative 3D nuclear imaging: reconstruction of 3D radioactive distributions using tracked gamma probes. *Medical image computing and computer-assisted intervention : MICCAI ... International Conference on Medical Image Computing and Computer-Assisted Intervention*, 10(Pt 2):909–17, 2007.

[63] Thomas Wendler, Joerg Traub, SibylleIlse Ziegler, and Nassir Navab. Navigated Three Dimensional Beta Probe for Optimal Cancer Resection. In Rasmus Larsen, Mads Nielsen, and Jon Sporring, editors, *Medical Image Computing and Computer-Assisted Intervention MICCAI 2006*, volume 4190 of *Lecture Notes in Computer Science*, pages 561–569. Springer Berlin Heidelberg, 2006.

[64] Jin Zhang, Peter D. Olcott, Garry Chinn, Angela M. K. Foudray, and Craig S. Levin. Study of the performance of a novel 1mm resolution dual-panel PET camera design dedicated to breast cancer imaging using Monte Carlo simulation. *Medical Physics*, 34(2):689–702, jan 2007.

[65] Jian Zhou and Jinyi Qi. Theoretical analysis and simulation study of a high-resolution zoom-in PET system. *Phys. Med. Biol.*, 54(17):5193, 2009.

[66] Jian Zhou and Jinyi Qi. Adaptive Imaging for Lesion Detection Using a Zoom-in PET System. *IEEE Transactions on Medical Imaging*, 30(1):119–130, jan 2011.

[67] Jian Zhou and Jinyi Qi. Fast and efficient fully 3D PET image reconstruction using sparse system matrix factorization with GPU acceleration, 2011.

Vita

Ke Li

Degrees

B.S. Electrical Engineering, July 2011
Fudan University, Shanghai, China
M.S. Electrical Engineering, May 2017
Washington University in St. Louis, MO, USA
Ph.D. Electrical Engineering, May 2017
Washington University in St. Louis, MO, USA

Professional Societies

Institute of Electrical and Electronic Engineers

Courses

Optimization, Digital Signal Processing, Quantitative Image Processing, Probability and Stochastic Processes, Information Theory, Detection and Estimation Theory, Special Topics: Alternating Minimization Algorithms in Information Theory and Inference, Biomedical Optics, Biomedical Imaging Technology, Stochastic Control, Graph Theory, Bayesian Statistics

Skills

Programming: C/C++, Java, Scala, Python, Matlab, R, KRL
Parallel Computing: OpenMP, OpenACC, CUDA

Employment

Intern Software Engineer, 2010.7-2010.9
Singapore Technology Engineering, Singapore
Graduate Research Assistant, 2011-2017
Teaching Assistant for ESE230 Circuits Labs, 2015 Fall
Washington University in St. Louis, MO, USA
Senior Compute and Performance Developer Technology Engineer, starting 2017.6
Nvidia Corporation, Santa Clara, CA, USA

Activities

Treasure, 2012-2013
Chinese Students and Scholars Association of WUSTL

Publications

[1] K. Li, A. Mathews, Q. Wang, J. Wen, J. OSullivan, and Y. Tai, A Feasibility Study of Point-of-Care PET System, in Society of Nuclear Medicine and Molecular Imaging Annual Meeting, 2015, vol. 56, no. supplement 3, p. 436.

[2] K. Li, A. J. Mathews, Q. Wang, J. Wen, J. A. OSullivan, and Y.-C. Tai, Preliminary Results from a Portable PET Probe System with Fast Image Reconstruction, in Nuclear Science Symposium and Medical Imaging Conference (NSS/MIC), 2014 IEEE, 2014.

[3] A. J. Mathews, K. Li, S. Komarov, Q. Wang, B. Ravindranath, J. A. OSullivan, and Y.-C. Tai, A generalized reconstruction framework for unconventional PET systems, Med. Phys., vol. 42, no. 8, 2015.

[4] Q. Wang, A. J. Mathews, K. Li, J. Wen, S. Komarov, J. A. OSullivan, and Y.-C. Tai, A dedicated high-resolution PET imager for plant sciences, Phys. Med. Biol., vol. 59, no. 19, p. 5613, 2014.

[5] Q. Wang, J. Wen, B. Ravindranath, A. W. OSullivan, D. Catherall, K. Li, S. Wei, S. Komarov, and Y.-C. Tai, A compact high resolution flat panel PET detector based on the new 4-side buttable MPPC for biomedical applications., Nucl. Instrum. Methods Phys. Res. A., vol. 794, pp. 151159, Sep. 2015.

[6] A. J. Mathews, K. Li, S. Komarov, Q. Wang, B. Ravindranath, J. A. OSullivan, and Y.-C. Tai, An image reconstruction framework for arbitrary positron emission tomography geometries, in Nuclear Science Symposium and Medical Imaging Conference (NSS/MIC), 2013 IEEE, 2013, pp. 16.

[7] C. Kreisch, R. E. Arvidson, J. A. OSullivan, K. Li, D. Politte, J. Finkel, E. Guinness, N. Stein, and A. Fraeman, Log-Likelihood

Method of Reducing Noise in CRISM Along-Track Oversampled Hyperspectral Images, in Imaging and Applied Optics 2015, 2015, p. CM4E.5.

[8] H. Ranjbar, J. Wen, A. J. Mathews, S. Komarov, Q. Wang, K. Li, J. A. OSullivan, and Y.-C. Tai, A simultaneous beta and coincidence-gamma imaging system for plant leaves, Phys. Med. Biol., vol. 61, no. 9, p. 3572, 2016.

Aug 2017